POLITECNICO DI TORINO

Master of Science in Aerospace Engineering

Master of Science Thesis

Navigation and Control Algorithm Design on TSE(3) around Small Irregular Bodies

Supervisor
Elisa Capello

Candidate
Gennaro Mangiacapra

Co-supervisor
Morad Nazari

April 2021

NAVIGATION AND CONTROL ALGORITHM DESIGN ON $\mathbb{TSE}(3)$ AROUND SMALL IRREGULAR BODIES

Master of Science Thesis

For obtaining the degree of Master of Science in Aerospace Engineering at Politecnico di Torino

Gennaro Mangiacapra

March 31, 2021

Dipartimento di Ingegneria Meccanica e Aerospaziale (DIMEAS) - Politecnico di Torino

Abstract

The configuration space of rigid body spacecraft is the Special Euclidean group $\mathsf{SE}(3)$ defined as a Lie group. The formalism of rigid body motion using $\mathsf{SE}(3)$ and its tangent bundle $\mathsf{TSE}(3)$ is developed in the field of Geometric Mechanics, which represents a modern description of the classic mechanics from the perspective of differential geometry. The use of Lie groups in the space field is of growing interest in the scientific community. Conventionally, the orbital and attitude dynamics of the spacecraft are analyzed separately which results in a misleading simplification of the reality since such analyses do not consider the orbit-attitude coupling. That coupling especially exists when the spacecraft operates in highly nonlinear environments, such as in the nonlinear gravity field of irregular bodies such as asteroids. The main advantage of using $\mathsf{SE}(3)$ consists in taking into account the nonlinear coupling between their translational and rotational dynamics, meanwhile preserving the geometrical properties of the system.

This work has the objective of developing novel navigation and control algorithms using the Lie groups formalism, with application to spacecraft motion around small irregular bodies. Although the control problem on $\mathsf{TSE}(3)$ for space applications has been extensively studied, the navigation problem on $\mathsf{TSE}(3)$ still requires further research. In fact, in literature, the design of navigation systems on Lie groups is especially addressed to robotic application.

First, the open-loop dynamics of the spacecraft orbiting as small irregular body are investigated using a variational integrator. Then, two Navigation and Control systems have been designed and tested through a simulation environment built in Matlab/Simulink with a Model-Based approach. Stochastic state filters have been designed on Lie groups based on the Unscented Kalman Filter (UKF) and a Super-Twisting Sliding Mode Observer. A performance analysis is conducted to test their behavior in the open loop system. The$\mathsf{TSE}(3)$ formalism led to the design of two nonlinear control algorithms represented by a single compact law accounting for the translational and rotational dynamics simultaneously. The first one based on the Morse-Lyapunov and Backstepping approaches, the second based on the robust Sliding Mode Control. They have been tested in some test cases, which emphasized the wastefulness of control effort when some source of noise is introduced in the closed-loop system. This latter situation may represent the closed-loop system without a state filter or state observer. Finally, using the Matlab/Simulink simulation environment, different combinations of navigation and control systems have been extensively tested and compared in different study cases. Those combinations have been compared in terms of some performance indices such as the estimation accuracy, the tracking error, the control effort, and the propellant mass required for a simultaneous orbit-attitude tracking. The simulations shows the efficacy of the design on $\mathsf{TSE}(3)$ in terms of required control effort and achieved tracking accuracy.

Sommario

In letteratura esistono diversi metodi per rappresentare un corpo rigido; in questa tesi, si è considerato lo Special Euclidean group SE(3) che per definizione è un Lie group. La dinamica del corpo rigido formalizzata in SE(3) ed il suo spazio tangente TSE(3) è sviluppata nel campo della geometria meccanica, la quale rappresenta una descrizione moderna della meccanica classica utilizzando il formalismo della geometria differenziale. L'utilizzo dei Lie group nel settore spaziale sta guadagnando sempre più attenzione, dato che la dinamica orbitale e la dinamica di assetto sono solitamente trattate separatamente. Non considerare l'accoppiamento tra gradi di libertà transazionali e rotazionali porta ad una notevole semplificazione della realtà, specialmente in casi in cui il satellite opera in campi particolarmente non lineari, come ad esempio, il campo gravitazionale generato da un piccolo ed irregolare corpo centrale. La scrittura del problema in SE(3) consente di tenere in considerazione l'accoppiamento non lineare orbitale e di assetto, allo stesso tempo preservando le proprietà geometriche del sistema.

Questo lavoro ha l'obiettivo di sviluppare nuovi algoritmi di navigazione e controllo, utilizzando il formalismo dei Lie group, con applicazione alla dinamica di un veicolo spaziale intorno ad un corpo centrale irregolare. Nonostante il problema del controllo in TSE(3) per applicazioni spaziali sia stato ampiamente studiato, si ritrovano pochi studi sul problema della navigazione in TSE(3), pur essendo ampiamente trattato nel campo della robotica.

Prima di procedere allo studio degli algoritmi, viene analizzata la dinamica open-loop dello spacecraft in orbita intorno ad un corpo centrale irregolare, utilizzando un integratore variazionale. Due sistemi di navigazione e due sistemi di controllo sono progettati e testati attraverso un ambiente di simulazione in Matlab/Simulink. Uno filtro di stato stocastico è stato sviluppato in TSE(3) partendo dalla teoria del Unscented Kalman Filter (UKF), inoltre è stato anche sviluppato un osservatore basato sulla teoria del Super-Twisting Sliding Mode. Le loro performance sono state testate in open-loop. Successivamente, due sistemi di controllo non lineare sono stati sviluppati in TSE(3), consentendo il design di una singola e compatta legge di controllo capace di considerare sia la dinamica traslazionale che rotazionale. Il primo algoritmo di controllo proposto è basato sulla teoria di Morse-Lyapunov e sul Backstepping, il secondo invece è basato sul controllo robusto a struttura variabile, di tipo Sliding Mode Control. Essi sono stati testati considerando diversi scenari, che hanno messo in evidenza la difficoltà nel controllare accuratamente il veicolo spaziale quando del rumore viene introdotto nel sistema closed-loop. Infine, le diverse combinazioni ottenute dai sistemi di navigazione e controllo sviluppati sono state testate paragonate per diversi scenari. Tali combinazioni sono state confrontate sulla base di alcuni parametri di performance, come l'accuratezza della stima dello stato, l'errore di tracking commesso, l'input richiesto dal sistema di controllo o la massa di propellente richiesta per il tracking simultaneo di orbita e assetto. I risultati ottenuti hanno mostrato l'efficacia del design in TSE(3), in particolare in

termini dell'accuratezza raggiunta e della richiesta di control effort.

Acknowledgment

This master thesis represents the conclusion of a period of self-fulfilling and mind opening studies between Politecnico di Torino and Delft University of Technology. An achievement that would not have been possible without sharing the path with several individuals to whom I owe genuine gratitude and respect. Although it is impossible to list everyone here, I would like to mention some in particular.

First of all, I would like to express my sincere gratitude to my supervisors Dr.Elisa Capello and Dr. Morad Nazari for guiding me towards the topics of this thesis. They provided me valuable insights and expertise that greatly assisted this research. I would like to thank my supervisors for giving me the opportunity to work in a stimulating research environment.

I would like to emphasize my deep gratitude to my family. Not only because of their teachings, support, and guidance all along my studies and my life. They always have believed in me regardless of my choices.

Special thanks goes to my beloved Chiara, who has always supported me no matter I was in Turin, Delft or Rome. She has been always there for me and ready to go, with her little suitcase packed

Many thanks go to my fellow students. Although I spent in Turin just the first year of MSc, I will always bring with me good memories of the time spent with Salvatore E. and Alessio P.. The memories of the date 18/07/2019 and a glass of sambuca under the sun, are enough to epitomize our times. Besides them, I would like to thank my friend Andrea M.. We shared important experiences during the year in Delft and I am grateful I met someone as crazy as me.

I would like to thank my dear friend Rocco V.. We have shared a lot during these years despite the different paths we took, and I hope it will always be as it is.

Last, but most definitely not least, I would like to thank my brothers Antonio D. and Antonio E. with whom I have shared thoughts, projects and amazing holidays during these years. In conclusion, my friends Mary G., Carmen C., Marica R., Giosue D. M., Stefano M., Pasquale G, Sara G., with whom I shared moments of pure carefreeness and amusement.

Little people discuss other people.
Average people discuss events.
Big people discuss ideas.

Rudolf E. Kalman

Contents

List of Figures

List of Tables

Chapter 1

Introduction

1.1 Objectives and Motivations

The objective of this work is the design of novel navigation and control algorithms using the Lie groups formalism, with application to spacecraft motion around small irregular bodies. The use of $\mathsf{SE}(3)$ and its tangent bundle $\mathsf{TSE}(3)$ in the space field is of growing interest in the scientific community. It allows to take into account the nonlinear coupling between the orbit-attitude dynamics, meanwhile preserving the geometrical properties of the system. This frameworks permits the execution of coupled translational and rotational maneuvers in three-dimensional Euclidean space while tracking a desired trajectory. The design of compact and efficient control algorithms on $\mathsf{SE}(3)$ and its tangent bundle $\mathsf{TSE}(3)$ has been extensively investigated and showed for spacecraft applications, for autonomous spacecraft rendezvous and docking [1], asteroid operations [2] or spacecraft formation flying [3]. On the other hand, the navigation problem on $\mathsf{TSE}(3)$ still requires further research. The design of navigation algorithms is a necessary step for any real application due to the intrinsic stochasticity of measurements and real instrumentation. The development of navigation filter and observers is still premature on $\mathsf{TSE}(3)$ for spacecraft application. In fact, the scientific community addresses the design of navigation systems on Lie groups especially to robotic applications. The Extended Kalman Filter (EKF) on $\mathsf{SE}(3)$ [4, 5], discrete-EKF (D-EKF) on $\mathsf{SE}(3)$ [6, 7], and Unscented Kalman Filter (UKF) on $\mathsf{SE}(3)$ [8, 9, 10] are some examples. According to the literature, these estimators are more accurate than their counterparts designed in vector Euclidean space, although formulation development of the filter design on $\mathsf{SE}(3)$ is more complex than that in vector Euclidean space. The aforementioned works exploit the geometrical mechanics frameworks by using the associated maps and operators in the state update step, where the measurements are defined in the Lie algebra but the filter is designed on the Lie group $\mathsf{SE}(3)$. The motivations that led this research can be found in the promising results that can be achieved with a complete design on on $\mathsf{SE}(3)$ and its tangent bundle $\mathsf{TSE}(3)$, highlighted by the scientific community. This type of design is particular suited for spacecraft application where the problem consists estimating the spacecraft state meanwhile controlling its orbit and attitude.

The geometric mechanics is a branch of mathematics which represents a modern description of the classic mechanics from the perspective of differential geometry. It applies principally to systems whose configuration space is a Lie group, or a group of diffeomorphisms [11]. The geometric mechanics, as well as the tools developed in this framework, has the characteristic of preserving the geometric properties of the physi-

cal system. The configuration space of a rigid body spacecraft is the Special Euclidean group $\mathsf{SE}(3)$, defined as a Lie group. In a three-dimensional space, the pose, or the configuration of a rigid body can be described by the location of its center of mass and its orientation with respect to a reference frame. The first one is adequately represented in Euclidean space. The attitude, instead, evolves in a nonlinear space provided with a certain geometry [12]. In particular, the attitude of a rigid body can be represented mathematically by a 3×3 orthonormal matrix with positive determinant. The set of these matrices is a manifold as it is locally diffeomorphic to a Euclidean space, and it also has a group structure with the group action of matrix multiplication. A smooth manifold with a group structure is referred to as a Lie group [13]. The Lie group of 3×3 orthonormal matrices with positive determinant is referred to as the Special Orthogonal group $\mathsf{SO}(3)$. The configuration manifold for the combined translational and rotational motion of a rigid body is the special Euclidean group $\mathsf{SE}(3)$, which is the semi-direct product of $\mathbb{R}^3$ and $\mathsf{SO}(3)$, i.e. $\mathsf{SE}(3)=\mathsf{SO}(3)\ltimes\mathbb{R}^3$ [14].

Spacecraft can be adequately approximated as rigid bodies defining the spacecraft motion as a six degrees of freedom body with translational (orbital) and rotational (attitude) motions, while this assumption excludes the possibility of taking flexible body dynamics into account. Different representations can be found in the literature for dynamics. Particularly, the spacecraft translational motion can be formulated and propagated using several type of formulation such as Cowell, Encke, Clohessy-Wilthsire, equinoctial elements or unified state model [15, 16, 17]. Since the spacecraft trajectory is mainly influenced by the gravitational attraction of other celestial bodies, the aforementioned methods take advantage of the orbital mechanics to improve the stability and accuracy of the dynamics propagation.

On the other side, the spacecraft rotational dynamics can be modeled using an attitude parameterization set, which is often defined by three or four parameters. Attitude parameterization sets can be minimal three-parameter sets defined in 3-dimensional Euclidean space $\mathbb{R}^3$ (principal rotation, Euler angles, classical Rodrigues parameters, and modified Rodrigues parameters) or redundant four-parameter set defined on the 3-sphere S^3 (quaternions). Kinematics modeling using minimal attitude parameterization sets can result in singularity. Quaternions, instead, are non-singular. However, since quaternions are not unique, they cannot generally result in a unique solution. This non-uniqueness can result in an undesired phenomenon of unwinding for large rotations, such as rigid body initial tumbling, although this can be avoided by using discontinuous feedback or nonlinear control laws. Alternatively, rigid body attitude can be represented using the direction cosine matrix (rotation matrix) defined on the special orthogonal group $\mathsf{SO}(3)$. Formalism of attitude using rotation matrices helps avoid the problems of singularity and non-uniqueness [18, 19, 20, 21]. The geometric mechanics formulation is based on the rotation matrix $R\in\mathsf{SO}(3)$. Fig. 1.1 summarizes the disadvantages of the commonly used attitude parametrization sets.

disadvantage	Θ	CRP	MRP	EA	q	R
attitude parameter singularity		×				
kinematic singularity	×	×		×		
nonlinear KDE*	×	×	×	×		
non-uniqueness	×				×	
redundancy	×				×	×
discontinuity			×			

* KDE: kinematic differential equation

Figure 1.1: Disadvantages of attitude parameterization sets and rotation matrix: principal rotation (Θ), classical Rodriguez parameters (CRP), modified Rodriquez parameters with switching (MRP), Euler angles (EA), quaternions (q), and rotation matrix (R) [22].

Conventionally, the analysis of the orbital and attitude dynamics of the spacecraft are conducted separately, resulting in separate control laws for attitude and translational motion. This decoupling is commonly assumed in the design of control algorithms for translational and attitude dynamics. However, as clearly discussed in several references such as [23, 24, 25], the coupling between the translational and rotational dynamics of the spacecraft should be considered in spacecraft dynamics analysis and control design. The simultaneous modeling of spacecraft orbital/attitude dynamics using special Euclidean group $\mathsf{SE}(3)$ is advantageous since it considers the coupling between translational and rotational dynamics. Such coupling can be due to gravity gradient forces and torques in highly nonlinear gravity fields, attitude-dependent forces and torques due to drag and solar radiation pressure, spacecraft rendezvous, proximity operations and docking, or spacecraft hovering over small bodies. This coupling has been considered in dynamic analysis and control design of rigid body or spacecraft, as in [26, 21, 27, 28, 29] and results in accurate, viable results for the rigid body and rigid-body spacecraft motion.

The design of navigation and control systems is part of the the more general guidance, navigation and control (GNC) system. The definition of GNC system used in this work is represented by the simple schematic in Fig. 1.2. In real-world applications, the consideration of stochastic processes is a crucial part of any GNC system. The navigation system includes the sensors and the filter and it enables to provide a state estimation based on the sensor measurements. The estimation process refers to the computation of an approximation of the (state) variables such that their values are usable for some other purpose. Even if the inputs of the algorithm are incomplete, uncertain or corrupted [30]. The on-board instruments, such as the inertial measurement unit, gyroscopes, accelerometers, and star trackers, have limited accuracy and are usually characterized by a degree of uncertainty. These uncertainties can arise not only due to the noise in the instruments, but also from electrical components, communication systems, or external disturbances, and result in inaccuracies and loss of precision in the measurements. In addition, some states might not be observable, as is the case with gyroscope biases. For the reasons mentioned above, there is a need for using state filters, such as the Kalman filters, that are capable of handling stochastic sources and can fuse the measurements from different sources optimally to estimate unobservable states [31, 32, 33].

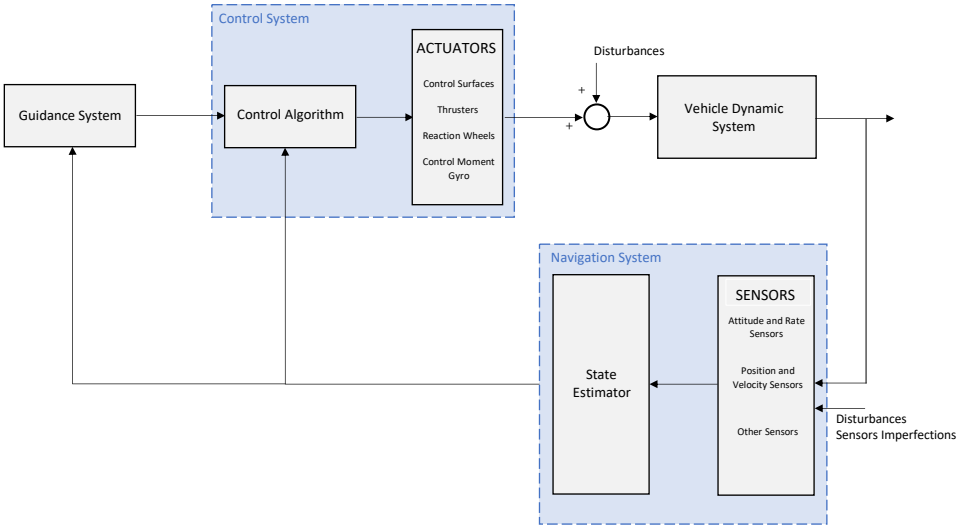

Figure 1.2: Simplified schematic of a GNC system.

The guidance system provides the desired state at each point in time, which will then be compared with the estimated state, provided by the navigation system, enabling the controller to generate the required commands [34]. The desired state follows from the physical motion constraints, the on-board models and the actual vehicles state. Typically the generation of the nominal trajectory is done on ground by means of optimization techniques. The trajectory is the result of a process that minimizes or maximizes some measures of performance (maximize payload, minimize fuel consumption, minimize cost, etc.) within prescribed constraint boundaries (maximum heat load, bending moment, maximum acceleration, constraints on flight path, etc.) [35]. Then a database is uploaded on board, covering a full range of possibilities which take care of inaccuracies of initial conditions, vehicle parameter uncertainties and environment disturbances. Advanced guidance systems are equipped with a trajectory generator which re-optimize the reference variables in case deviations of the actual vehicles states becomes too large with respect the nominal ones. Typically the output of the guidance system are smooth, time-varying reference signals.

The control system is composed of the control algorithm and the actuators. It receives the desired states from the guidance system and the estimated states from the navigation system. It computes the difference between the commanded (by the guidance logic) and measured (by the sensors) state, which is known as the state error for control, or control error. Then a control algorithm determines determines the actuators commands based on some control concept, e.g., a combination of P(roportional), I(ntegral) and D(erivative) manipulation of the control error, H_∞, Nonlinear Dynamics Inversion (NDI), Sliding Mode control (SMC), Model-Based Predictive control (MPC), Backstepping control or another concept. The Actuators are the actual hardware elements that convert the control commands to forces and moments. There are different types of ac-

tuators: reaction wheels, control moment gyroscopes, thrusters, magnetic torquer or control surfaces [36].

1.2 THESIS OUTLINE

In this work two navigation systems are designed. The first one is a stochastic state filter designed through a direct UKF based on the unscented transform (UT) described in [37]. A retraction function between the manifold and the vector Euclidean space [38, 39] and the inverse of that function are used to encode the UT sigma points onto the manifold and decode them from the manifold, respectively. The state filter has been introduced in the prior work [40], and now its formalism is revised to describe the dynamic system characterized by stochastic processes in a compact form on $\mathsf{TSE}(3)$. The second navigation system is designed on the basis of the conventional Super-Twisting Sliding Mode Observer (STO) described on vector Euclidean space [41]. The stochasticity is treated on $\mathsf{SE}(3)$ and its tangent bundle $\mathsf{TSE}(3)$ as discussed in [42, 4, 8]. It is important to emphasize that the two proposed systems employ very different state estimators. The STO is a deterministic state observer, meaning that the prediction of the state doesn't involve any source of randomness. In fact, the observer is structured as a copy of the plant and its gains remain constant through out the process, once they are selected. On the other hand, the UKF is a stochastic state filter, meaning that the prediction of the state possess some inherent randomness. Particularly, the UKF is a an algorithm which uses external measurements, containing noise, and computes estimates of the unknown variables that are more accurate than those based just on the measurements, by estimating a joint probability distribution over the variables for each instant of time. Thus, unlike the STO, the UKF gains are continuously changed by the algorithm itself [43].

The $\mathsf{TSE}(3)$ formalism leads to the design of two nonlinear control algorithms represented by a single compact law accounting for the translational and rotational dynamics simultaneously. The first one extends to regulation controller in [21, 40] and has been already used in the prior work [40] to design an almost globally asymptotically stable control algorithm based on the Morse-Lyapunov and Backstepping approaches (MLBS). The rationale of this nonlinear control consists in finding an asymptotically stable control law, capable of cancelling the system nonlinearities using the Lyapunov stability theory. The second control algorithm is based on the robust Sliding Mode Control (SMC), which is extended to $\mathsf{TSE}(3)$. Particularly, the sliding surface is designed using special configuration functions to encode the state on $\mathsf{TSE}(3)$ to a scalar quantity. This type of control algorithms is recognized as an efficient technique to withstand external disturbances and model uncertainties, and has been widely adopted for spacecraft applications [44, 45, 46, 47].

In this work the spacecraft dynamics is integrated using a fixed time step variational integrator (VI), which allows to preserve the geometric properties of the system [48]. The accuracy of the used VI is investigated for the orbit propagation application introducing a benchmark study case, before the spacecraft open loop dynamics is simulated. The results are analyzed, discussed and compared to those obtained with a point-mass spacecraft. Finally, the navigation and control systems algorithms and their combinations are extensively tested and compared in different case studies. The use of some performance

indices such as the estimation accuracy, the tracking error, the control effort, and the propellant mass required for a simultaneous orbit-attitude tracking, help to understand the efficacy of the design on $\mathsf{TSE}(3)$.

In order to achieve the aforementioned objectives, this work has been structured in the following chapters:

- Chapter 1. In this chapter, the objectives and motivations for this work are introduced. The novelty of the design on $\mathsf{TSE}(3)$ is highlighted. Background information are illustrated, with emphasis to the geometric mechanics framework and the GNC systems.
- Chapter 2. This chapter introduces the Lie Group $\mathsf{SE}(3)$ and its tangent bundle $\mathsf{TSE}(3)$ and the mathematical operators used on this manifold. The rigid body kinematic and kinetic equations are formulated on $\mathsf{SE}(3)$ and the gravitational model for the small irregular central body is introduced.
- Chapter 3. This chapter focuses on the design of state estimators on Lie groups based on the Unscented Kalman Filter and a Super-Twisting Sliding Mode Observer. Before the discussion of their formulation, a novel stochastic system formulation on $\mathsf{TSE}(3)$ is introduced, and the sensor selection is briefly discussed.
- Chapter 4. This chapter focuses on the design of two nonlinear control algorithms represented by a single compact law accounting for the translational and rotational dynamics simultaneously. The first one based on the Morse-Lyapunov and Backstepping approaches, the second based on the robust Sliding Mode control. Before the discussion of their formulation, the actuator selection is briefly discussed.
- Chapter 5. This final chapter is committed to the simulation results and discussion. First, the variational integrator accuracy is investigated from the perspective of the orbit propagation. The spacecraft open loop dynamics is analyzed and compared to the one of a point mass spacecraft. Then, the navigation systems singularly are tested in open-loop in different of case studies. The control system performances are analyzed in the same manner. Finally different combinations of navigation and control systems are extensively tested and compared in different case studies.

Chapter 2

Preliminaries and Problem Statement

In this chapter the mathematical background to be used in the Special Euclidean Group $\mathsf{SE}(3)$ *and its tangent bundle* $\mathsf{TSE}(3)$ *is introduced; the rigid body dynamics model is deduced and the gravitational field of small irregular bodies is presented.*

2.1 Formalism in Geometric Mechanics Framework

The spacecraft configuration is defined by six degrees of freedom, three of which are related to the location of its center of mass and the other three are related to its attitude. According to [49, 50], the configuration space of a rigid-body spacecraft is a member of the Lie group $\mathsf{SE}(3)$ which is a smooth manifold obeying the group properties (closure under multiplication, identity, associativity, and invertability) and that the group operations are differentiable. The configuration of a rigid body can be expressed as

$$g = \begin{bmatrix} R & r \\ 0_{1\times 3} & 1 \end{bmatrix} \in \mathsf{SE}(3) \tag{2.1}$$

where $R \in \mathsf{SO}(3)$ is the rotation matrix from the body frame to the inertial frame, $r \in \mathbb{R}^3$ is the position vector from the origin of the inertial frame to the center of mass of the rigid body expressed in the inertial frame, and I_3 is the 3×3 identity matrix. The smoothness of the matrix Lie group implies the existence of a single tangent space at each point. The tangent space at the identity element of the group is referred to as Lie algebra [13] and is denoted as

$$\mathfrak{se}(3) = \left\{ \mathbb{V}^\vee = \begin{bmatrix} \omega^\times & v \\ 0_{1\times 3} & 0 \end{bmatrix},\ \omega^\times \in \mathfrak{so}(3),\ v \in \mathbb{R}^3 \right\} \tag{2.2}$$

where $(\cdot)^\vee$ indicates the wedge map, i.e. $(\cdot)^\vee : \mathbb{R}^6 \to \mathfrak{se}(3)$ applied to the vector $\mathbb{V} = [\omega^T, v^T]^T$ which is the augmented velocity vector, defined through the translational velocity $v \in \mathbb{R}^3$ and the angular velocity $\omega \in \mathbb{R}^3$; $\mathfrak{so}(3)$ is the set of 3 by 3 skew symmetric matrices such that $\omega^\times$ can be defined in terms of the components of the angular velocity vector. According to [14], given the vector $\omega = [\omega_1, \omega_2, \omega_3]^T$, the cross map $(\cdot)^\times : \mathbb{R}^3 \to \mathfrak{so}(3)$ is defined as

$$\omega^\times = \begin{bmatrix} 0 & -\omega_3 & \omega_2 \\ \omega_3 & 0 & -\omega_1 \\ -\omega_2 & \omega_1 & 0 \end{bmatrix} \tag{2.3}$$

From the definition of Lie group $\mathsf{SE}(3)$ and its Lie algebra $\mathfrak{se}(3)$, the geometric link between the two formulations can be understood. The Lie algebra can be considered as a linearization of the Lie group, near the identity element [51]. Due to the complexity of the nonlinear structure of the Lie group, it is difficult to study with conventional mathematical tools. The important feature of the Lie algebra is that it is a linear vector space and thus it can be studied using the tools developed in linear algebra. However, the extraction of the $\mathsf{SE}(3)$ properties from its Lie algebra opens the possibility to several scientific applications [52]. The exponential map $\exp : \mathfrak{se}(3) \to \mathsf{SE}(3)$ allows to transfer elements of the Lie algebra to the Lie group which, intuitively, can be interpreted as a wrapping operation, from the tangent plane onto the manifold. Formally, it is a local diffeomorphism from a neighborhood of zero in $\mathfrak{se}(3)$ onto a neighborhood of the identity element in $\mathsf{SE}(3)$ [14]. The following figures help to gather more intuitive information about the previous statements.

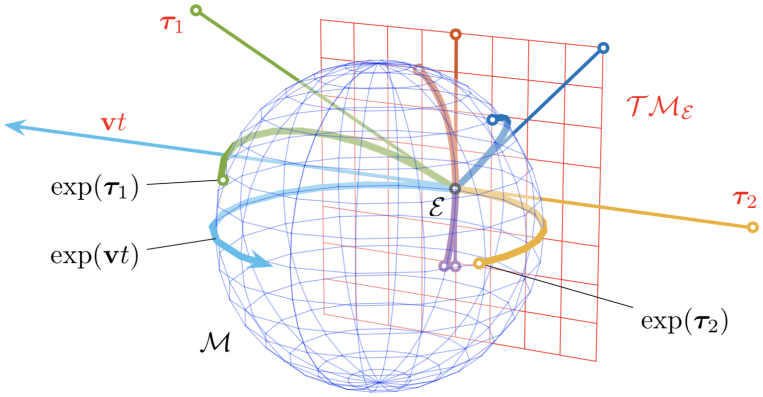

Figure 2.1: Lie group and Lie algebra relation figurative representation.

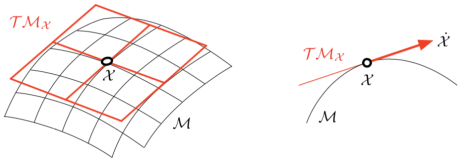

Figure 2.2: Manifold and vector space relation figurative representation.

Figure 2.1 depicts a figurative representation of Lie group and Lie algebra. The Lie algebra (red plane) is the tangent space to the Lie group's manifold (represented as a blue sphere) at the identity ϵ. Through the exponential map, each straight path vt through the origin on the Lie algebra produces a path $\exp(vt)$ over the manifold which runs along the respective geodesic. Conversely, each element of the group has an equivalent in the Lie algebra. This relation is so profound that (nearly) all operations in the group, which is curved and nonlinear, have an exact equivalent in the Lie algebra, which is a linear vector

space. It must be emphasized that this figure is just a figurative representation, since the sphere in $\mathbb{R}^3$ is not a Lie group. Actually it describes the group of unit quaternions [13]. Figure 2.3 represents a manifold $\mathscr{M}$ and the vector space $\mathscr{TM}_{\mathscr{X}}$ (in this case $\approx \mathbb{R}^2$) tangent at the point $\mathscr{X}$, and a convenient side-cut. The velocity element, $\dot{\mathscr{X}} = \partial\mathscr{X}/\partial t$, does not belong to the manifold $\mathscr{M}$ but to the tangent space $\mathscr{TM}_{\mathscr{X}}$ [13].

The exponential coordinates are defined as

$$\xi = \begin{bmatrix} \Theta \\ p \end{bmatrix} \in \mathbb{R}^6, \tag{2.4}$$

where $\Theta \in \mathbb{R}^3$ represents rotational vector, it is the product of eigenaxis (principal axis) and eigenangle (principal angle) of rotation, i.e. $\Theta = \theta e$, $\theta = \|\Theta\|$; $p \in \mathbb{R}^3$ represents the translational vector. Hence, the configuration g is obtained via exponential map $\exp : \mathfrak{se}(3) \to \mathsf{SE}(3)$ as

$$g = \exp(\xi^\vee) = \sum_{n=0}^{\infty} \frac{1}{n!}(\xi^\vee)^n, \tag{2.5}$$

which, according to [53], can be written as

$$g = \begin{bmatrix} R(\Theta) & S(\Theta)p \\ 0 & 1 \end{bmatrix} \in \mathsf{SE}(3), \tag{2.6}$$

where $R(\Theta) \in \mathsf{SO}(3)$ is the rotation matrix from body frame to the inertial frame. The rotation matrix is obtained via Rodrigues formula as

$$R(\Theta) = \exp(\Theta^\times) = I + \frac{\sin\theta}{\theta}\Theta^\times + \frac{1-\cos\theta}{\theta^2}(\Theta^\times)^2, \tag{2.7}$$

and

$$S(\Theta) = I + \frac{1-\cos\theta}{\theta^2}\Theta^\times + \frac{\theta-\sin\theta}{\theta^3}(\Theta^\times)^2. \tag{2.8}$$

Note that the inverse of the exponential map is the logarithmic map $\log : \mathsf{SE}(3) \to \mathfrak{se}(3)$ which can be interpreted as an unwrapping operation. The exponential coordinates can be obtained via logarithmic map as

$$\xi^\vee = \log_{\mathsf{SE}(3)}(g) \tag{2.9}$$

2.2 RIGID BODY MOTION FORMULATION ON TSE(3)

The rigid body configuration is defined by 6 degrees of freedom, 3 of which related to the location of its center of mass and the other 3 related to its attitude. According to [49],[50], the configuration space of a rigid-body spacecraft is the Lie group $\mathsf{SE}(3)$. This is a smooth manifold obeying the group properties (closure under multiplication, identity, associativity, and invertability) with the additional condition that the group operations are differentiable. The configuration of a rigid body can be expressed as in Eq.(2.1). The smoothness of the matrix Lie group implies the existence of a single tangent space at each point.

Particularly, the tangent space at the identity element of the group is referred to as Lie algebra [13]. The rigid body kinematic and kinetic equations of motion are given as written with respect to an inertial reference frame and expressed in the body-fixed frame as

$$\dot{g} = g\mathbb{V}^{\vee}, \tag{2.10}$$

$$\dot{\mathbb{V}} = \mathbb{I}^{-1}\mathrm{ad}^{*}_{\mathbb{V}}\mathbb{I}\mathbb{V} + \mathbb{I}^{-1}\left(u_g + u_c + u_d\right),$$

where $g \in \mathsf{SE}(3)$ represents the rigid body configuration as defined in Eq. (2.1), $\mathbb{V} = [\omega^T, v^T]^T$ denotes the rigid body augmented velocity vector expressed in the body frame, $u_g \in \mathbb{R}^6$ denotes the external input due to gravitational effect, and $u_c \in \mathbb{R}^6$ is the control input produced by the control system. Finally $u_d \in \mathbb{R}^6$ represents the effect of additional disturbances which may enter as input in the system. The complete state is thus represented by $(g, \mathbb{V}) \in \mathsf{SE}(3) \times \mathbb{R}^6 = \mathsf{TSE}(3)$, the tangent bundle of $\mathsf{SE}(3)$. In this framework, both the attitude and the translational displacement are considered simultaneously. This allows to design an estimation algorithm and a control system in $\mathsf{TSE}(3)$, which is more versatile and more accurate than the standard decoupled procedures. In Eq. (2.10), the inertia tensor in $\mathsf{SE}(3)$ is given as

$$\mathbb{I} = \begin{bmatrix} J & 0_{3\times3} \\ 0_{3\times3} & mI_3 \end{bmatrix} \in \mathbb{R}^6 \tag{2.11}$$

where $J \in \mathbb{R}^{3\times3}$ is the moment of inertia about the center of mass, and m is the mass of the system. Moreover, the co-adjoint operator is defined as

$$\mathrm{ad}^{*}_{\mathbb{V}} = \mathrm{ad}^{T}_{\mathbb{V}} = \begin{bmatrix} -\omega^{\times} & -v^{\times} \\ 0_{3\times3} & -\omega^{\times} \end{bmatrix} \tag{2.12}$$

where the adjoint operator $\mathrm{ad}_{\mathbb{V}}$ is

$$\mathrm{ad}_{\mathbb{V}} = \begin{bmatrix} \omega^{\times} & 0_{3\times3} \\ -v^{\times} & -\omega^{\times} \end{bmatrix} \tag{2.13}$$

From an intuitive point of view, this operator allows to transform a tangent vector from the tangent space around one element to the tangent space around another one.

2.3 DYNAMICS OF SPACECRAFT HOVERING NEAR SMALL BODIES

For many small bodies, the asymmetric distribution of mass becomes a more significant element in the dynamics than in their larger counterparts such as Earth, Jupiter, or their major moons. For rigid body dynamics, the torque on the spacecraft body caused by the asymmetry must be considered. The gravity force exerted by the asteroid on the spacecraft is described using a second degree and order spherical harmonic gravity field. Assuming the origin of the asteroid body-centered inertial frame (BCI) coinciding with the center of mass of the body, the first degree and order gravity terms are $C_{11} = C_{10} = S_{11} = 0$. The asteroid is modeled as a constant density triaxial ellipsoid with major axes l_1, l_2, and l_3. This assumption makes the second degree and order terms C_{21}, S_{21}, S_{22}

identically zero. The gravity potential of second degree and order of the celestial body given in [54] can be revisited as

$$U = \frac{\mu}{\|\rho\|}\left(1+\frac{1}{\|\rho\|^2}\left(C_{20}\left(-\frac{1}{2}+\frac{3}{2}(\hat{\rho}\cdot\hat{K})^2\right)+3C_{22}\left(1-(\hat{\rho}\cdot\hat{K})^2-2(\hat{\rho}\cdot\hat{J})^2\right)\right)\right), \tag{2.14}$$

where $\rho = \|\rho\|\hat{\rho} \in \mathbb{R}^3$ is the position vector of an arbitrary point on the spacecraft expressed in the BCI frame such that $r = \frac{1}{m}\int_{\mathscr{B}} \rho\, dm$, $(\hat{I},\hat{J},\hat{K})$ is the unit basis of the BCI frame, and the second degree and order coefficients are [55, 56, 57]

$$C_{20} = -J_2 = \frac{1}{5}(\gamma^2 - \frac{\alpha^2+\beta^2}{2}), \qquad C_{22} = \frac{1}{20}(\alpha^2-\beta^2) \tag{2.15}$$

where $\alpha = 1$, $\beta = \frac{l_2}{l_1}$, and $\gamma = \frac{l_3}{l_1}$ are normalized semi major axes of the ellipsoid. According to [58], the presented gravitational potential is effective to study the orbit-attitude coupled spacecraft dynamics in proximity of small irregular bodies. Taking the partial derivative of the gravity potential U in Eq. (2.14) with respect to ρ, integrating over the body of the spacecraft, and keeping only the terms up to order $1/\rho^4$, the gravity gradient force applied to the spacecraft expressed in spacecraft body fixed (SBF) coordinates is approximated as

$$F_g = R^T\int_{\mathscr{B}}\frac{\partial U}{\partial \rho}dm = R^T\left(F_{g_1}+F_{g_2}\right), \tag{2.16}$$

where R is the rotation matrix from the SBF frame to the BCI frame,

$$F_{g_1} = -m\frac{\mu}{\|r\|^2}\left(1+\frac{3}{m\|r\|^2}\left[J+\frac{1}{2}\left(\mathrm{tr}(J)-5\,\hat{r}^T R\,J\,R^T\hat{r}\right)I_3\right]\right)\hat{r}, \tag{2.17}$$

$\hat{r} = r/\|r\|$, and

$$F_{g_2} = \frac{m\mu}{\|r\|^4}\left(\left[\begin{array}{c}\left(\frac{3}{2}C_{20}-9C_{22}\right)\left(\hat{r}\cdot\hat{I}\right)\\ \left(\frac{3}{2}C_{20}-21C_{22}\right)\left(\hat{r}\cdot\hat{J}\right)\\ \left(\frac{9}{2}C_{20}-15C_{22}\right)\left(\hat{r}\cdot\hat{K}\right)\end{array}\right]+\frac{15}{\|r\|}\left(\left(-\frac{C_{20}}{2}+C_{22}\right)\hat{r}\cdot\hat{K}+2C_{22}\hat{r}\cdot\hat{J}\right)\hat{r}\right) \tag{2.18}$$

which is an alternative representation to that given in [59]. The gravity gradient torque on the rigid-body spacecraft due to the gravitational field of the central body is expressed in the SBF frame as

$$M_g = \frac{3\mu}{\|r\|^3}(R^T\hat{r})^\times JR^T\hat{r} \tag{2.19}$$

Therefore, the total augmented external effect given in Eq. (2.10) is $u_g = [F_g^T, M_g^T]^T$, where the gravitational force and moment are given in Eq. (2.16)-(2.19), respectively.

2.3.1 CENTRAL BODIES PARAMETERS

In this work, three different asteroids will be used as central bodies to perform the simulations. They are assumed to be triaxial ellipsoids with uniform density. The first body is the asteroid Bennu whose properties are shown in Tab.2.1. The second body is the Saturnian moon Pan whose properties are given in Tab.2.2.

Table 2.1: Assumed parameters for asteroid Bennu [59, 60, 61].

Parameter	Values
Mass $[kg]$	$m = 7.80 \cdot 10^{10}$
Gravitational Parameter $[km^3/s^2]$	$\mu = 5.2060 \cdot 10^{-9}$
Triaxial Ellipsoid Axes $[km]$	$(l_1, l_2, l_3) = (0.535, 0.508, 0.365)$
Coefficients $[-]$	$C_{20} = -0.0971, C_{22} = 0.0049$
Rotation Period $[h]$	$T = 4.297$

Table 2.2: Assumed parameters for Saturnian moon Pan [62].

Parameter	Values
Mass $[kg]$	$m = 4.95 \cdot 10^{15}$
Gravitational Parameter $[km^3/s^2]$	$\mu = 3.3038 \cdot 10^{-4}$
Triaxial Ellipsoid Axes $[km]$	$(l_1, l_2, l_3) = (34.4, 31.4, 20.8)$
Coefficients $[-]$	$C_{20} = -0.1102, C_{22} = 0.0083$
Rotation Period $[h]$	$T = 14$

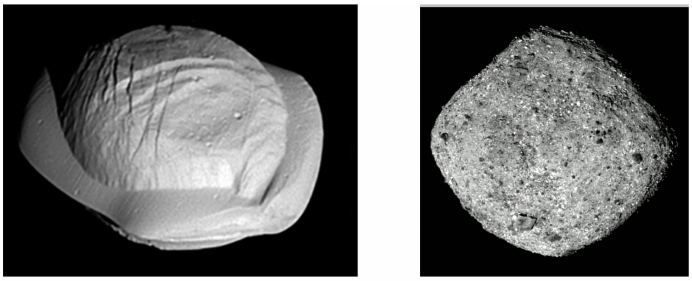

Figure 2.3: Representation of the Saturnian moon Pan (left) and the asteroid Bennu (right).

Chapter 3

Navigation System Design

This chapter focuses on the design of state estimators on Lie groups based on the Unscented Kalman Filter and a Super-Twisting Sliding Mode Observer. Before the discussion of their formulation, a novel stochastic system formulation on $\mathsf{TSE}(3)$ *is introduced, and the sensor selection is briefly discussed.*

3.1 Sensors Selection

The type of sensors the spacecraft is equipped with play a major role in the design of any navigation algorithm. The reason lies in the fact that each type of sensor is able to provide a measurement within a certain accuracy and with a certain degree of noise. Clearly, when cheap sensors are used, it can be expected that the measurements are more compromised by noise and inaccuracies. Therefore the navigation designer has to dedicate a great effort to the navigation algorithm, which has to take over inaccurate measurements. On the other hand, accurate sensors allow the designer to dedicate less effort in the algorithm design.

In this work, any particular sensor model is implemented. Instead, it is assumed that the spacecraft state (attitude, position and velocities) is completely observable and available to feedback. Even if any sensor model has been used, a white Gaussian zero mean noise is added to the feebacked state. Moreover, the covariance of the noise for each state is selected on the basis of the accuracy of the sensors typically employed for spacecraft applications. Spacecraft position and velocity states are principally determined using force models based on the modelization of the spacecraft dynamics, with with occasional position fixes from ground stations. This is more accurate than the use of inertial navigation except during periods of significant maneuvering. Position fixes in low Earth orbit can be obtained from GNSS (Global Navigation Satellite System), from ground stations through radio transmission, or with visual matching of planetary features. The spacecraft attitude solution is maintained using a gyroscopes, kept aligned with attitude fixes from a star tracker. For satellites in low Earth orbit, other aiding may be used, such as magnetometers, horizon sensors or GNSS information. In Tab.3.1, the typical accuracy of sensors employed for attitude estimation is reported.

Table 3.1: Attitude sensors performance comparison [63].

Sensor	Accuracy [deg]
Sun Sensors	$0.01 - 0.1$
Horizon Sensors	$0.02 - 0.03$
Magnetometer	1
Star tracker	0.001
Gyroscope	0.01/h

3.2 STOCHASTIC PROCESSES ON LIE GROUPS AND SYSTEM FORMULATION

The mathematical model employed for the control and state estimation is usually developed in the Euclidean space, which is an affine space and, by definition, is a geometric structure based on the vectorial space [13]. When the mathematical modeling is performed in Euclidean space, it is common to deal with uncertainties simply using an additive approach. Basically, an Additive White Gaussian Noise (AWGN) can be considered as representative of the many random processes that occur in nature. However, when the model is developed in $\mathsf{SE}(3)$ and its tangent bundle $\mathsf{TSE}(3)$, uncertainties and stochastic processes cannot be formulated using the conventional mathematical models that are commonly used in the Euclidean space. This is due to the fact that $\mathsf{SE}(3)$ is a nonlinear manifold and not a vectorial space [42]. In this research, the formulation covered in [64, 4, 8] is used to accommodate a stochastic process in the model. Since the source of noise is assumed to be in vector space, the exponential map $\exp(\cdot)$ is used to map it into $\mathsf{SE}(3)$ as

$$\chi_n = \bar{\chi}_n \exp(n^\vee) \quad n \sim \mathcal{N}(0, N) \tag{3.1}$$

where χ_n is the noise in $\mathsf{SE}(3)$ and $\mathcal{N}(0, N)$ denotes the Gaussian distribution in Euclidean space with zero mean and covariance matrix $N \in \mathbb{R}^{6\times 6}$. In Eq. (3.1), post multiplication by $\bar{\chi}_\eta \in \mathsf{SE}(3)$ causes the original Gaussian $\eta \in \mathbb{R}^6$ of the Lie algebra to center at $\bar{\chi}_\eta \in \mathsf{SE}(3)$. The symbols χ_η and $\bar{\chi}_\eta$ represent a small perturbation with covariance N and a large source of noise, respectively. Fig.3.1 depicts the Gaussian distribution on the Lie group and its algebra for the random variable n at the identity I.

The Kalman filter technique expects the definition of two sources of noise: process noise and measurement noise. The first one accounts for all the model uncertainties, disturbances, and unmodelled dynamics which are easily modelled as lumped process noise [65]. The measurement noise, instead represents the uncertainty and imperfection of the sensors employed in the navigation system. The stochastic system formulation which best accommodates the application of Kalman filter theory expects an additive approach for both the process and the measurement noise. Particularly, the process noise is added to the state derivative equation, and the measurement noise is added to the system output equation. In this work, the aforementioned approach can not be adopted, because the state of the system $x = (g, \mathbb{V})$ is on $\mathsf{TSE}(3)$. Although the velocity, expressed in $\mathbb{R}^6$, allows to simply add the noise, the pose requires the notation given in Eq. (3.1) since it is defined on $\mathsf{SE}(3)$. Although different estimation techniques can be found in the literature, none of them account for a state vector that is defined on $\mathsf{TSE}(3)$. Therefore, a novel, augmented formulation is introduced.

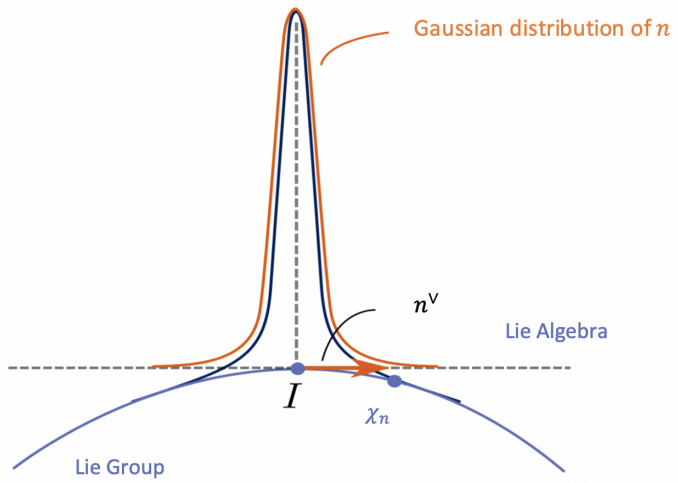

Figure 3.1: Concentrated distribution on Lie group with mean at the identity, where $\chi_n = \exp(n^\vee)$ and the random variable n has a Gaussian distribution in $\mathbb{R}^6$. The concentrated distribution with non-identity mean is defined using the left translation, as shown in Eq.(3.1) [66].

It is assumed that the spacecraft pose and velocity are measurable and the output of the system, $z \in \mathbb{R}^{12}$, consists of the principal angles of rotation Θ, the translational vector components r, the angular velocity ω, and the translational velocity v. It must be emphasized that the use of the principal angles of rotation doesn't represent the attitude parametrization, which is based on the rotation matrix. Instead, Θ is just used to represent the rotation matrix as output of the system. In addition, using the principal angle of rotation allows to take advantage of the $\mathsf{SE}(3)$ maps and operator previously defined, thus having a compact stochastic system formulation. Particularly the stochastic system can be written on $\mathsf{TSE}(3)$ as

$$\dot{x}(t) : \begin{cases} \dot{g} = \chi_{\eta_g}\, g\mathbb{V}^\vee \\ \dot{\mathbb{V}} = \mathbb{I}^{-1}\mathrm{ad}^*_{\mathbb{V}+\eta_\mathbb{V}}\mathbb{I}(\mathbb{V}+\eta_\mathbb{V}) + \mathbb{I}^{-1}u \end{cases} \tag{3.2}$$

$$z(t) = [(\log_{\mathsf{SE}(3)}(\chi_{\zeta_g} g)^|)^T, \mathbb{V}^T + \zeta_\mathbb{V}^T]^T \tag{3.3}$$

where $(\cdot)^|$ is the inverse of the vedge map. The dependence on time is omitted in the right sides for the readability of the equations. The process noise $\zeta = [\zeta_g^T, \zeta_\mathbb{V}^T]^T \in \mathbb{R}^{12}$ and the measurement noise $\eta = [\eta_g^T, \eta_\mathbb{V}^T]^T \in \mathbb{R}^{12}$ are assumed to be Gaussian white-noise processes. In addition, they are assumed to be uncorrelated and thus the second order joint central moment, i.e. the covariance, is zero. The aforementioned assumption leads to:

$$E\{\eta(t)\} = B_\eta \qquad E\{\eta(t)\eta(t+\tau)^T\} = Q \qquad \eta \sim \mathcal{N}(B_\eta, Q) \tag{3.4}$$

$$E\{\zeta(t)\} = B_\zeta \qquad E\{\zeta(t)\zeta^T(t+\tau)\} = T \qquad \zeta \sim \mathcal{N}(B_\zeta, T) \tag{3.5}$$

$$E\left\{\zeta(t)\eta^T(t+\tau)\right\} = 0 \tag{3.6}$$

where τ represents the time lag, $Q \in \mathbb{R}^{12\times12}$ is the process noise covariance matrix, $T \in \mathbb{R}^{12\times12}$ is the measurement noise covariance matrix and $B_\eta \in \mathbb{R}^{12\times12}$ contain the measurement noise biases. The process noise is zero mean since the bias is encoded thought the post multiplication in SE(3). In fact, the pose state equation can be revised as

$$\dot{g} = \bar{\chi}_{\eta_g} \exp(\eta_g^\vee) g \mathbb{V}^\vee \tag{3.7}$$

where the noise biases are represented by $\hat{\chi}_{\zeta_g} \in \mathsf{SE}(3)$. The stochastic system formulation in Eqs.(3.2)-(3.3) is written in the following compact form, which will be employed in the description of the UKF steps described in the subsequent section

$$\begin{aligned} \dot{x}(t) &= f\left(x(t), u(t), \eta(t)\right) \\ z(t) &= h\left(x(t), \zeta(t)\right) \end{aligned} \tag{3.8}$$

$f(\cdot) \in \mathsf{TSE}(3)$ represents the nonlinear state function, which depends on the state, input, process noise and time. $h(\cdot) \in \mathbb{R}^{12}$ represents the measurement function, which depends on the state, measurement noise and time. Again, the time dependence is omitted. The stochastic model adopted in this work is schematically represented in the following figure.

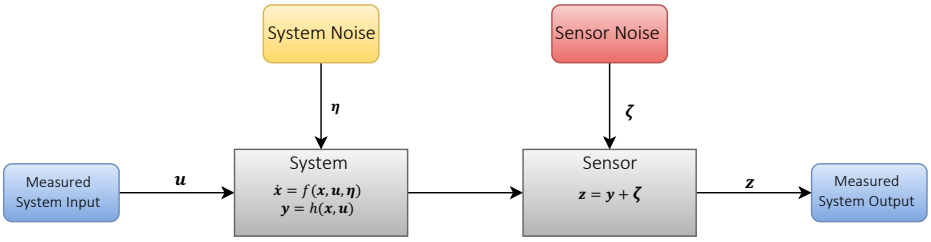

Figure 3.2: Schematic representation of the stochastic system modeling adopted for this work.

3.3 UNSCENTED KALMAN FILTER DESIGN ON TSE(3)

The first navigation system is based on the Unscented Kalman Filter (UKF) state estimator, which belongs to the family of filters known as Sigma-Point Kalman Filters or Linear Regression Kalman Filters, which use the statistical linearization technique [67, 68]. This technique linearizes a nonlinear function of random variable through a linear regression obtained from the the prior distribution of the random variable. Since the problem at hand deals with the spread of the random variables, this techniques tend to be more accurate than Taylor series linearization, which is the basis of the Extended Kalman Filter (EKF) or the Iterated Extended Kalman Filter (IEKF) [10]. In these techniques the state distribution is propagated analytically through the first-order linearization of the nonlinear system. Hence, the a posteriori covariance and mean could be corrupted [69]. The UKF, instead handles the problem with a deterministic sampling approach. A minimal

set of sample points, called sigma points, are carefully chosen to represent the state distribution. Hence the UKF avoids the computation of the system's Jacobians thus leading to a versatile and easy algorithm to be translated for fast hardware implementation [9].

The intuition that it is easier to approximate a probability distribution than to approximate an arbitrary nonlinear function is the leading idea which the UKF is based upon [70]. The sigma points are selected such that their mean is the state x and their covariance is the state covariance matrix P. Then, the sigma points are propagated through the nonlinear dynamics with the purpose of capturing the *a posteriori* mean and covariance with high accuracy. This process is known as Unscented Transformation (UT) and it is used to compute the statistics of a random variable which undergoes a nonlinear transformation [37].

Starting from the system of Eqs. (3.2)-(3.3), the state estimation is performed using the UKF which is formulated on TSE(3). The filter implementation is based on that given in [39], where an innovative UKF technique on manifolds was introduced. The novel UKF on TSE(3) design has been discussed and introduced in the previous work [40].

Generally the Kalman Filter techniques consists of two main step:

- Prediction Step: in this phase the state and its error covariance are predicated on the basis of the system mathematical model. Usually this phase takes the name of *a priori* estimate of the system.
- Measurement Update Step: in this phase the *a priori* state is corrected with an external measure. This procedure allows to obtain a better state estimate, defined as *a posteriori* estimate of the system.

The UKF has an additional preliminary step, which consists in the UT and hence the computation of the sigma points. In the subsequent sections, the actual state and state error covariance matrix are indicated $\hat{x}[k|k], P[k|k]$ respectively. The *a priori* state error covariance matrix are indicated $\hat{x}[k+1|k], P[k+1|k]$ respectively. The *a posteriori* state error covariance matrix are indicated $\hat{x}[k+1|k+1], P[k+1|k+1]$ respectively. Note that the adopted nomenclature $[a|b]$ indicates that the estimates at a are obtained with the information of the estimates at b.

3.3.1 SIGMA POINTS SELECTION STEP

The number of the sigma points clearly depends on the dimension of the system. From now on the letter p indicates the state dimension and the quantities related to it and the letter q refers to the process noise. Given the current state covariance matrix $P[k|k]$ and process noise matrix Q two different sets of sigma points are computed. The UT requires $2p+1$ points for the first set and $2q+1$ for the second one, where the additional point refers to the mean of the distribution. Therefore $2p+1$ sigma points χ_p related to the state error covariance matrix and $2q+1$ sigma points χ_q related to the process noise matrix are defined. The matrix $\boldsymbol{\chi}_p[k] \in \mathbb{R}^{p\times 2p+1}$ of $2p$ sigma column vectors $\chi_{p,i}[k]$ is

formed according to

$$\begin{aligned}
&\chi_{p,0}[k] = 0 \\
&\chi_{p,i}[k] = \chi_{p,0}[k] + (\sqrt{(p+\lambda_p)P[k|k]})_i \qquad i = 1,\dots,p \\
&\chi_{p,i}[k] = \chi_{p,0}[k] - (\sqrt{(p+\lambda_p)P[k|k]})_{i-p} \qquad i = p+1,\dots,2p
\end{aligned} \tag{3.9}$$

where $\chi_{p,0}[k]$ represents the mean of the distribution, and the other $2p$ points the dispersion around it. $[k]$ indicates the current kth step and $\lambda_p = (\alpha^2 - 1)p$ is a scaling parameter. The constants α determines the spread of the sigma points around their mean and is usually set to a small positive value, e.g. $10^{-4} \leq \alpha \leq 1$. $(\sqrt{(p+\lambda_p)P[k|k]})_i$ is the ith column of the matrix square root (e.g. lower triangular Cholesky factorization). Moreover the sigma points are defined along with their weights

$$\begin{aligned}
W_{p,0}^{(m)} &= \frac{\lambda_p}{\lambda_p + p} \\
W_{p,0}^{(c)} &= \frac{\lambda_p}{\lambda_p + p} + (1 - \alpha^2 + \beta) \\
W_{p,i}^{(m)} &= W_{p,i}^{(c)} = \frac{1}{2(d+\lambda_d)} \qquad i = 1,...,2p
\end{aligned} \tag{3.10}$$

where (c) refers to the covariance and (m) to the mean. The first ones will be used to compute the sigma points mean after they are passed through the nonlinear system, while the latter ones are used for the computation of the sigma points covariances. In addition the subscript 0 refers to the mean of the distribution. The constant β is used to incorporate prior knowledge of the distribution of the state. The value $\beta = 2$ is optimal for Gaussian distribution and is commonly selected as value. In other words, the matrix $\boldsymbol{\chi}_p[k]$ and its weights are constructed as

$$\boldsymbol{\chi}_p[k] = \begin{bmatrix} \chi_{p,0}[k] & \chi_{p,0}[k] + \sqrt{(p+\lambda_p)P[k|k]} & \chi_{p,0}[k] - \sqrt{(p+\lambda_p)P[k|k]} \end{bmatrix} \tag{3.11}$$

$$\begin{aligned}
W_p^{(m)} &= \begin{bmatrix} W_{p,0}^{(m)} & W_{p,1}^{(m)} & \dots & W_{2p,1}^{(m)} \end{bmatrix} \\
W_p^{(c)} &= \begin{bmatrix} W_{p,0}^{(c)} & W_{p,1}^{(c)} & \dots & W_{2p,1}^{(c)} \end{bmatrix}
\end{aligned} \tag{3.12}$$

The same procedure applies to the set $\boldsymbol{\chi}_q[k]$ related to the process noise matrix. In particular the matrix $\boldsymbol{\chi}_q[k] \in \mathbb{R}^{q \times 2q+1}$ of $2q$ sigma column vectors $\chi_{q,i}[k]$ is formed according to

$$\begin{aligned}
&\chi_{q,0}[k] = 0 \\
&\chi_{q,i}[k] = \chi_{q,0}[k] + (\sqrt{(q+\lambda_q)Q})_i \qquad i = 1,\dots,q \\
&\chi_{q,i}[k] = \chi_{q,0}[k] - (\sqrt{(q+\lambda_q)Q})_{i-q} \qquad i = q+1,\dots,2q
\end{aligned} \tag{3.13}$$

and their weights

$$\begin{aligned} W_{q,0}^{(m)} &= \frac{\lambda_q}{\lambda_q + q} \\ W_{q,0}^{(c)} &= \frac{\lambda_q}{\lambda_p + q} + (1 - \alpha^2 + \beta) \\ W_{q,i}^{(m)} &= W_{q,i}^{(c)} = \frac{1}{2(q + \lambda_q)} \qquad i = 1, ..., 2q \end{aligned} \tag{3.14}$$

Or in other words, the matrix $\boldsymbol{\chi}_q[k]$ and its weights are constructed as

$$\boldsymbol{\chi}_q[k] = \begin{bmatrix} \chi_{q,0}[k] & \chi_{q,0}[k] + \sqrt{(q+\lambda_q)Q} & \chi_{q,0}[k] - \sqrt{(q+\lambda_q)Q} \end{bmatrix} \tag{3.15}$$

$$\begin{aligned} W_q^{(m)} &= \begin{bmatrix} W_{q,0}^{(m)} & W_{q,1}^{(m)} & ... & W_{2q,1}^{(m)} \end{bmatrix} \\ W_q^{(c)} &= \begin{bmatrix} W_{q,0}^{(c)} & W_{q,1}^{(c)} & ... & W_{2q,1}^{(c)} \end{bmatrix} \end{aligned} \tag{3.16}$$

In the update step, a third set of sigma points $\boldsymbol{\chi}_u$[k] will be generated with the one-step-ahead state prediction $\hat{x}[k+1|k]$. In principle a third set of weights may be defined, however the same of the $\boldsymbol{\chi}_p$[k] set will be used.

3.3.2 PREDICTION STEP

The prediction takes as the input the current estimated state $\hat{x}[k|k]$, the current estimated covariance state matrix $P[k|k]$, and the sigma points vectors $\chi_{i,q}, \chi_{i,p}$ obtained with the current estimates. The objective of this step is the computation of the one-step-ahead state prediction $x[k+1|k]$ and the one-step-ahead state covariance matrix prediction $P[k+1|k]$. It is clear that the UKF needs to be initialized with the initial state estimate $\hat{x}_0 = E\{x_0\}$ and the initial covariance state matrix $P_0 = E\{(x_0 - \hat{x}_0)(x_0 - \hat{x}_0)^T\}$. Since the system states are on $\mathsf{TSE}(3)$, a retraction function $\varphi(\cdot) : \mathbb{R}^{12} \to \mathsf{TSE}(3)$ is introduced, which is a smooth, arbitrarily-chosen function that encodes the mean and covariance noise on the Lie group and its tangent bundle. The retraction function is divided into two parts to manage the augmented state:

$$\varphi(x, \chi_i) : \begin{cases} \varphi_g = g \exp((\chi_i^g)^\vee)) \\ \varphi_{\mathbb{V}} = \mathbb{V} + \chi_i^{\mathbb{V}} \end{cases} \tag{3.17}$$

where χ_i^g indicates the first $p/2$ elements of the sigma points vector χ_i, and $\chi_i^{\mathbb{V}}$ the latest $p/2$. It can be noted that when $\chi_j = 0$ then $\varphi(x, 0) = x$. The inverse retraction function $\varphi^{-1} : \mathsf{TSE}(3) \to \mathbb{R}^{12}$ can be obtained as

$$\varphi^{-1}(\hat{x}, x) : \begin{cases} \varphi_g^{-1} = \log_{\mathsf{SE}(3)}(\hat{g}^{-1} g) \\ \varphi_{\mathbb{V}}^{-1} = \hat{\mathbb{V}} - \mathbb{V} \end{cases} \tag{3.18}$$

where $\hat{x} = (\hat{g}, \hat{\mathbb{V}})$ and $x = (g, \mathbb{V})$. Given the current optimal estimated state $\hat{x}[k|k]$, the first set of sigma points are retracted into the manifold and then used to propagate the

system dynamics starting from $\hat{x}[k|k]$

$$x_{\chi_{p,i}}[k] = f\left(\varphi\left(\hat{x}[k|k], \chi_{p,i}[k]\right), \hat{u}[k], 0\right) \qquad i = 0, \dots, 2p \tag{3.19}$$

where the current input vector $\hat{u}[k]$ is assumed not measurable, and hence it is estimated using the current state $\hat{x}[k|k]$. The sigma points which represents the mean of the distribution, $\chi_{p,0}[k]$ returns the mean state which is used as one-step-ahead state prediction

$$\hat{x}[k+1|k] = f(\varphi\left(\hat{x}[k|k], \chi_{p,0}[k]\right), \hat{u}[k], 0) \tag{3.20}$$

and since $\chi_{p,0}[k] = 0$, the retraction function returns $\hat{x}[k|k]$, i.e.

$$\hat{x}[k+1|k] = f(\hat{x}[k|k], \hat{u}[k], 0) \tag{3.21}$$

In order to compute the covariance matrix with respect the state uncertainty, the obtained states are retracted back into $\mathbb{R}^{12}$ with the inverse retraction function. The retracted sigma points matrix $\boldsymbol{\chi}_p^r[k] \in \mathbb{R}^{p \times 2p+1}$ is then obtained as

$$\chi_{p,i}^r[k] = \varphi^{-1}(\hat{x}[k+1|k], x_{\chi_{p,i}}[k]) \qquad i = 0, \dots, 2p \tag{3.22}$$

and since $x_{\chi_{p,0}}[k] = \hat{x}[k+1|k]$, the first column of the matrix is $\chi_{p,0}^r[k] = 0$. The retracted sigma points mean is computed as

$$\overline{\chi}_p^r[k] = \sum_{i=0}^{2d} W_{p,i}^{(m)} \chi_{p,i}^r[k] \quad \in \mathbb{R}^{2p} \tag{3.23}$$

and finally the covariance matrix with respect to the state uncertainty can be computed as

$$P[k+1|k] = W_p^{(c)} (\boldsymbol{\chi}_p^r[k] - \overline{\chi}_p^r[k])(\boldsymbol{\chi}_p^r[k] - \overline{\chi}_p^r[k])^T \tag{3.24}$$

This matrix needs to be corrected with the contribute which comes from the process noise. Hence, the second set of sigma points, $\chi_{q,i}[k]$ are used similarly to the first one. The main important difference is that these points are not used as initial condition for the propagation, since they are not related to the state. Instead, they are introduced in the propagation as process noise

$$x_{\chi_{q,i}}[k] = f\left(\hat{x}[k|k], \hat{u}[k], \chi_{q,i}[k]\right) \qquad i = 0, \dots, 2q \tag{3.25}$$

it is clear that the first the sigma points which represents the mean of the distribution, $\chi_{q,0}[k]$ returns $\hat{x}[k+1|k]$, according to Eq.(3.21). The obtained states are retracted back into $\mathbb{R}^{12}$ with the inverse retraction function. The retracted sigma points matrix $\boldsymbol{\chi}_q^r[k] \in \mathbb{R}^{q \times 2q+1}$ is then obtained as

$$\chi_{q,i}^r[k] = \varphi^{-1}(\hat{x}[k+1|k], x_{\chi_{q,i}}[k]) \qquad i = 0, \dots, 2q \tag{3.26}$$

and since $x_{\chi_{q,0}}[k] = \hat{x}[k+1|k]$, the first column of the matrix is $\chi_{q,0}^r[k] = 0$. The retracted sigma points mean is computed as

$$\overline{\chi}_q^r[k] = \sum_{i=0}^{2d} W_{q,i}^{(m)} \chi_{q,i}^r[k] \quad \in \mathbb{R}^{2q} \tag{3.27}$$

and the covariance matrix with respect to the noise can be computed as

$$Q[k+1|k] = W_q^{(c)}(\boldsymbol{\chi}_q^r[k] - \overline{\chi}_q^r[k])(\boldsymbol{\chi}_q^r[k] - \overline{\chi}_q^r[k])^T \tag{3.28}$$

Finally, the one-step-ahead state error covariance matrix is computed correcting Eq.(3.24) as

$$\begin{aligned} P[k+1|k] &= P[k+1|k] + Q[k+1|k] \\ &= W_p^{(c)}(\boldsymbol{\chi}_p^r[k] - \overline{\chi}_p^r[k])(\boldsymbol{\chi}_p^r[k] - \overline{\chi}_p^r[k])^T + W_q^{(c)}(\boldsymbol{\chi}_q^r[k] - \overline{\chi}_q^r[k])(\boldsymbol{\chi}_q^r[k] - \overline{\chi}_q^r[k])^T \end{aligned} \tag{3.29}$$

It is interesting to note that the second contribute is weighted on the basis of the process noise covariance matrix Q. If the knowledge of the true model is poor, then Q has large elements and then the *a priori* covariance state error matrix estimate has a large dispersion.

3.3.3 MEASUREMENT UPDATE STEP

Once $\hat{x}[k+1|k]$ and $P[k+1|k]$ are computed and the measurement $z[k]$ is known, the correction can be performed. As already mentioned the third set of sigma points with the predicted state error covariance matrix are computed. The matrix $\boldsymbol{\chi}_u[k] \in \mathbb{R}^{p\times 2p+1}$ of $2p$ sigma column vectors $\chi_{u,i}[k]$ is formed according to

$$\begin{aligned} &\chi_{u,0}[k+1] = 0 \\ &\chi_{u,i}[k+1] = \chi_{u,0}[k+1] + (\sqrt{(d+\lambda_d)P[k+1|k]})_i \qquad i = 1,\dots,p \\ &\chi_{u,i}[k+1] = \chi_{u,0}[k+1] - (\sqrt{(d+\lambda_d)P[k+1|k]})_{i-p} \qquad i = p+1,\dots,2p \end{aligned} \tag{3.30}$$

or equivalently

$$\boldsymbol{\chi}_u[k+1] = \begin{bmatrix} \chi_{u,0}[k+1] & \chi_{u,0}[k+1] + \sqrt{(p+\lambda_p)P[k+1|k]} & \chi_{u,0}[k+1] - \sqrt{(p+\lambda_p)P[k+1|k]} \end{bmatrix} \tag{3.31}$$

Each point is retracted into the manifold and then passed through the measurement function. The matrix $z_u \in \mathbb{R}^{p\times 2p+1}$ is constructed such as each column is

$$z_{u,i}[k+1] = h(\varphi(\hat{x}[k+1|k], \chi_{u,i}[k+1])), \qquad i = 0,\dots,2d \tag{3.32}$$

where the zeroth column is $z_{u,i}[k] = 0$ thanks to the retraction function properties. Since the ith measurement vector is part of $\mathbb{R}^{12}$ and not of TSE(3), there is not need to use the inverse of the retraction function. Therefore, the measurement mean is computed as

$$\overline{z}[k+1] = \sum_{i=0}^{2d} W_{p,i}^{(m)} z_i[k+1] \tag{3.33}$$

The measurement covariance matrix $P_{zz}[k+1]$ and the cross-covariance $P_{xz}[k+1]$ can then be obtained

$$P_{zz}[k+1] = W_p^{(c)}(z_u[k+1] - \overline{z}[k+1])(z_u[k+1] - \overline{z}[k+1])^T + R \tag{3.34}$$

$$P_{xz}[k+1] = W_p^{(c)} \boldsymbol{\chi}_u[k+1](z_u[k+1] - \overline{z}[k+1])^T \tag{3.35}$$

According to [71], the Kalman gain is the factor which allows to minimize the state covariance matrix P and is computed by

$$K[k+1] = P_{xz}[k+1]P_{zz}[k+1]^{-1} \tag{3.36}$$

The measurement covariance matrix $P_{zz}[k+1]$, in the conventional Kalman Filters is commonly known as sensitivity matrix S, that inversely weighs measurement errors. It means that if a noisy sensor is used the measurement covariance matrix R will have high elements and its inverse will produce a low Kalman gain. In other words the contribute of the external measurement update is weighted less. Finally, the *a posteriori* state estimate can be obtained as

$$\hat{x}[k+1|k+1] = \varphi(\hat{x}[k+1|k], K[k+1]r[k+1]) \tag{3.37}$$

where $r[k+1] = z[k+1] - \overline{z}[k+1]$ is the residual, i.e. the discrepancy, between the estimated measurement $\overline{z}+1$ from the *a priori* predictions and the actual measurement $z[k+1]$. It is clear that the Kalman gain $K[k+1]$ acts as a weighing factor for the residual. Particularly, when the measurement are corrupted and R assumes large values, then the Kalman gain is low and the residual is weighted less. Therefore this gain allows to have an optimal estimate weighting the received measurement on the basis of its reliability. And this degree of reliability is achieved by comparing the covariance of the estimated measurement and the covariance of the real measurement. Finally the *a posteriori* state error covariance matrix is

$$P[k+1|k+1] = P[k+1|k] - K[k+1]P_{zz}[k+1]K[k+1]^T \tag{3.38}$$

Figure3.3 represents the model-based scheme of the proposed UKF filter. Finally, the three steps that characterize the proposed UKF are summarized in Fig.3.4.

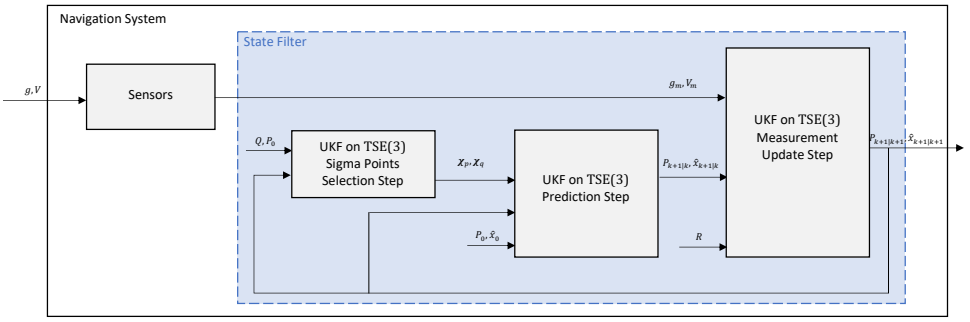

Figure 3.3: Schematic representative of the Simulink model for the Navigation System with the UKF state filter on TSE(3).

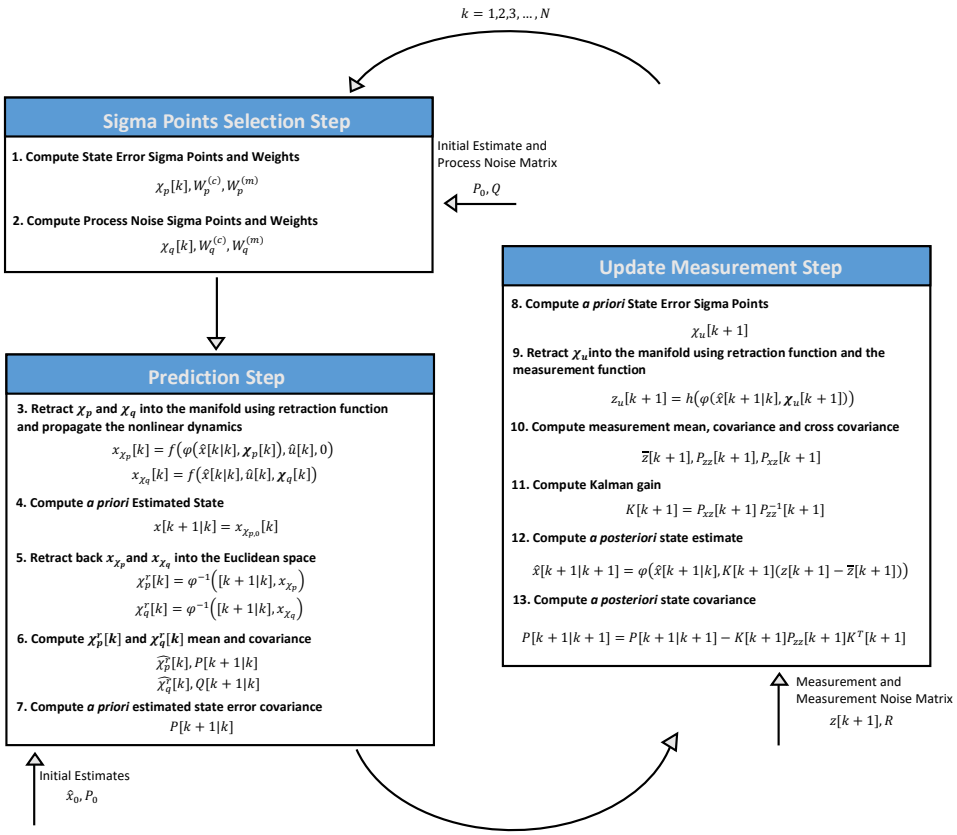

Figure 3.4: Unscented Kalman Filter steps scheme.

3.4 SUPER-TWISTING OBSERVER ON TSE(3)

The previous Navigation system was based on the Kalman Filter theory, which adopts a filtration approach to reconstruct the system states on the basis of the corrupted measurements. Particularly, the *a priori* knowledge of the noise statistics is optimally used to estimate the system true states. On the other hand, the second navigation system, is designed with a deterministic observer approach. In general, an observer is a replica of the system and has to role of estimating its unmeasurable states based only on the measured outputs and inputs. One of the earliest linear observer is the Luenberger observer. It feedbacks into the observer the difference between the output of the plant and the observer to estimates the states. However in presence of uncertainty, it is unable to force the output estimation error to zero and it may not converge to the system states [41]. Sliding mode observers provide an attractive and robust solution to this issues [72]. Particularly they are widely used since they are characterized by the unique features of being robustness with respect to unknown inputs and having a finite-time asymptotically convergence to exact values of the system states. In addition, disturbances within the system may also be reconstructed [73]. One of the main problem of the sliding mode

applications, is the unavoidable presence of chattering which is introduced by the discontinuous nature of the method.

The observer selected for the second navigation system, belongs to the family of high-order sliding mode (HOSM) observers. Particularly it is a second order Super-Twisting Observer (STO). It is one of the most popular second-order sliding mode algorithms which is able to reduce the chattering [74] and offers a finite reaching time [75]. In literature it is possible to find several works which use this algorithm for control purpose [76, 77, 78]. However it is interesting to point out that there is no application of such algorithm for estimation purpose on SE(3) or TSE(3).

The proposed Super-Twisting observer on TSE(3) estimates the spacecraft position, attitude and velocities.The presented Super-Twisting observer is based on the theory discussed in [41]. Recalling the rigid body dynamics on TSE(3) in Eq.(2.10) and their stochastic form in Eq.(3.2)-(3.3), the proposed observer structure is

$$\begin{aligned} \dot{\hat{g}} &= z_1^{-1}\hat{g}\hat{\mathbb{V}}^{\vee} \\ \dot{\hat{\mathbb{V}}} &= \mathbb{I}^{-1}\mathrm{ad}^{*}_{\hat{\mathbb{V}}}\mathbb{I}\hat{\mathbb{V}} + \mathbb{I}^{-1}\hat{u} + z_2 \end{aligned} \tag{3.39}$$

where $\hat{g}$ and $\hat{\mathbb{V}}$ are the state estimates on TSE(3) while the correction variables $z1 \in \mathsf{SE}(3)$ and $z_2 \in \mathbb{R}^6$ are output error injections. In addition, the input $\hat{u}$ is estimated using the current estimated state $\hat{x} = (\hat{g}, \hat{\mathbb{V}})$. The sliding surface $\sigma \in \mathbb{R}^6$ is designed as

$$\sigma = G_1\delta\mathbb{V} + G_2(log_{\mathsf{SE}(3)}(\delta g))^{|} \tag{3.40}$$

where $\delta\mathbb{V} = \mathbb{V}_m - \hat{\mathbb{V}}$ is the velocity estimation error with respect the measurement, and $\delta g = g_m^{-1}\hat{g}$ is the pose estimation error with respect the measurement. G_1, G_2

The output error injections have the form

$$\begin{aligned} z_1 &= \begin{bmatrix} \exp_{\mathsf{SO}(3)}(B_1(\mathrm{sgn}(\sigma_{1,2,3})\|\sigma_{1,2,3}\|^{1/2}) & B_2\,\mathrm{sgn}(\sigma_{4,5,6})\|\sigma_{4,5,6}\|^{1/2} \\ 0 & 1 \end{bmatrix} \\ z_2 &= B_3\,\mathrm{sign}(\sigma) \end{aligned} \tag{3.41}$$

where B_1 and B_2 are positive gains, and $B_3 = \mathrm{blockdiag}(B_{31}, B_{32})$ is a positive definite diagonal matrix. In order to reduce the chattering, instead of using the $\mathrm{sign}(\cdot)$ function, the hyperbolic tangent function is used $\tanh(\eta\,\cdot)$, with $\eta = 100$. Fig.3.5 represents the model-based scheme of the discussed observer.

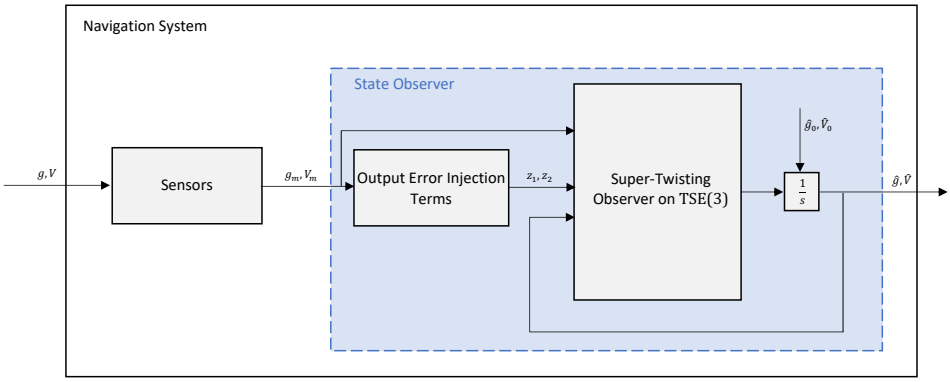

Figure 3.5: Schematic representation of the Simulink model for the Navigation System with the Super-Twisting state observer on TSE(3).

Chapter 4

Control System Design

This chapter focuses on the design of two nonlinear control algorithms represented by a single compact law accounting for the translational and rotational dynamics simultaneously. The first is based on the Morse-Lyapunov and Backstepping approaches and the second one is based on the robust Sliding Mode control. Before the discussion of their formulation, the selection of the actuator selection is briefly discussed.

4.1 Actuators Selection

The type of actuators play a main role in the design of any control system. The reason lies in the fact that each type of actuator is able to provide a certain amount of control force or moment. For instance, for the attitude control, a torque provided by a Reaction Control System (RCS) can be significantly larger than the torque provided by a magnetic torquer. This means different actuators are designed to work in different missions. Having the saturation limits (max provided control force and moment) as free variables, would increase the complexity of the simple analysis provided in the following sections. For this reason, it is imagined that the spacecraft is equipped with active actuators which require continuous feedback and adjustment. Particularly thrusters are used to provide control force and Control Moment Gyros (CMG) are used to provide the control moment. The saturation limits for the control force and moment are not set *a priori*. These values are left for the preliminary analysis of the control systems in Section 5.4.

For the CMG is not adopted any particular model, while for the thrusters the Tsiolkovsky rocket equation is used to compute the propellant mass consumption, which is used as a figure of merit for the control systems tuning. According to [79], using the momentum conservation, the engine thrust equation is

$$\dot{m} = -\frac{\|F_c\|}{v_e} \tag{4.1}$$

where $\dot{m}$ is the engine mass flow and v_e is the exhaust flow velocity, which is the velocity of the expelled particles relative to the rocket. The exhaust flow velocity is a figure of merit of rockets and gives a measure of how efficiently a rocket uses propellant. Eq.(4.1) is also useful to compute the required ΔV for the orbital maneuver

$$\Delta V = -v_e \log\left(\frac{M_0}{M_f}\right) = -v_e \log\left[\frac{M_0}{M_0 - \dot{m}\Delta t}\right] \tag{4.2}$$

where M_0 is the spacecraft total mass (dry mass + propellant mass), M_f is the mass once the maneuver is finished, and Δt is the burn time.

In the following section the spacecraft will be modeled with the properties described in Tab.4.1. It is assumed to have a propellant mass of $M_p = 1000\,kg$, which is about the 54% of the total mass. This ratio is consistent with real mission. For instance, the Cassini–Huygens spacecraft had a dry mass of 2523 kg and a propellant mass of 3051 kg [80]. The last parameter to set is the exhaust flow velocity, which depends on the specific fuel used. In this study a hydrazine mono propellant is selected and a conservative value of $v_e \approx 2000\,m/s^2$ is used [81, 82].

Table 4.1: Spacecraft thrusters parameters.

Parameter	Values
Propellant Mass $[kg]$	$M_p = 1000$
Exhaust Flow Velocity $[m/s]$	$v_e = 2000$

4.2 MORSE-LYAPUNOV BASED CONTROL VIA BACKSTEPPING ON TSE(3)

4.2.1 BACKSTEPPING CONTROL BACKGROUND

Generally, when a linear system is taken into account, its stability can be analyzed with linear techniques that involve the investigation of its poles. When a nonlinear system is analyzed, instead, there are not poles that can help and can characterize the overall stability of the system [83]. With nonlinear systems, the standard linear tools can only be used to assess a local stability analysis, which is based on linearization techniques around the neighborhood of the point of interest. A relevant example can be found in flight dynamics, where the vehicles are modeled as highly nonlinear systems [84]. From a practical perspective, an aircraft is a complex nonlinear system that operates in a wide range of flight conditions. Nevertheless, it must satisfy certain tracking and dynamics performances dictated by the regulations. Since the aircraft dynamic behavior can change meaningfully throughout the flight envelope, traditionally the gain-scheduling approach is preferred [85]. The rationale of this method lies in the linearization of the system in different regions of the flight envelope, thus allowing many linear control laws to be designed. Apart from its simplicity, this approach is conventionally preferred also because the linear control theory has been extensively studied. However the gain-scheduling procedure has many drawbacks due to the basis linearization procedure. In case of failures the aircraft dynamics changes deeply and the aforementioned approach is not able to provide accurate performance. The same can happen with combat aircrafts, that are characterized by a wide flight envelope and in some region the nonlinearities can be more significant [86, 87].

During the years, with the increase of the available computational power, more sophisticated methods have been developed. They can avoid the lack of robustness that characterizes the linear control laws. According to [88], the most used nonlinear model-based approaches, that also have been successfully applied in off-line and on-line aerospace applications are: the Feedback Linearization (FBL), also known as Nonlinear Dynamic

Inversion (NDI), and the Backstepping (BS). The first approach consists in finding a control law that cancels out the nonlinearities of the system, such that the overall system can be treated as a linear one, thus allowing a linear controller to be used. This procedure cancels completely the natural dynamics of the system and for this reason can lead to wasteful control effort [89]. The second control approach can give the designer more flexibility in the choice of the control input and therefore is considered as a kind of selective FBL [90]. This means that if the system has certain stabilizing nonlinearities, it is possible to keep them and cancel only some part of the nonlinear dynamics. Nevertheless, the BS approach is based on Lyapunov stability theory, which allows to design a control law that guarantees global asymptotic stabilization and tracking. Between the discussed control approaches, this work focuses on the flexible Lyapunov-based BS control design.

4.2.2 STABILITY AND LYAPUNOV THEORY

Before introducing the BS control design approach, the Lyapunov stability theory is concisely introduced. It is a necessary step, since the BS design is strongly based on this concept.

For a general nonlinear dynamics, the stability in the sense of Lyapunov of its equilibrium points can be assessed describing the behavior of the system in the neighborhood of it [91]. To be of practical interest, the nature of the equilibria should be determined without directly solve any differential equation. This is an important point since, in general, nonlinear dynamics can not be solved analytically. According to [92], for this purpose, the russian A.M. Lyapunov developed two methods:

- Indirect Method, which is based is based on local stability around an equilibrium point from the stability properties of its linear approximation. This method represents the theoretical justification of using linear control for nonlinear systems. It is clear that the main drawback is that this analysis is just local.
- Direct Method, which is not restricted to the local motion. It determines the stability properties of a nonlinear system on the basis of the observation that if the total energy of a system is dissipated, then the system must settle down to an equilibrium point. Basically an "energy-like" function is constructed and its time variation is analyzed.

The latter one is the most commonly used method for nonlinear system analysis and design, moreover it is the approach used in the BS algorithm. As already introduced, an appropriate continuous differentiable and positive defined scalar function called Lyapunov Candidate Function (LCF) $\mathcal{V}$ is chosen. Then its time derivative $\dot{\mathcal{V}}$ is evaluated, and whether it is negative (semi) definite the equilibrium point is globally asymptotically stable. The selected $\mathcal{V}$ is also called Control Lyapunov Function (CLF). It is emphasized that this method does not prescribe how to determine an appropriate Lyapunov function, which is a fundamental step in the BS approach.

A more intuitive visualization of Lyapunov stability theory may be given in Fig.4.1, where a system of two state variables is considered. This leads to a 2-D phase plane (x_1, x_2). The

CLF is a parabolic surface which lives in the third dimension and it is a function of the state variables, i.e. $\mathcal{V}(x_1, x_2)$. The origin of the phase plane is the equilibrium point. The derivative of $\mathcal{V}$ is given by

$$\frac{d\mathcal{V}}{dt} = (\text{grad}(\mathcal{V}))^T \frac{dX}{dt} \tag{4.3}$$

where $X = [x_1, x_2]^T$ is the state vector and

$$\text{grad}(\mathcal{V}) = \left[\frac{d\mathcal{V}}{dx_1}, \frac{d\mathcal{V}}{dx_2}\right]^T \qquad \frac{dX}{dt} = (\frac{dx_1}{dt}, \frac{dx_2}{dt}) \tag{4.4}$$

In the neighborhood of the origin, the CLF is negative definite because

$$\frac{d\mathcal{V}}{dt} = (\text{grad}(\mathcal{V}))^T \frac{dX}{dt} < 0 \tag{4.5}$$

which means that the angle φ is greater than 90 deg. Clearly if this condition is satisfied everywhere in the neighborhood of the origin, then the trajectory tends to the origin, i.e. the system is stable. Otherwise, when $\frac{d\mathcal{V}}{dt}$ is positive, the trajectory moves away from the origin, i.e. the system is unstable. This intuition can be easily extended to the stability analysis of a general equilibrium point $X^* = \left[x_1^*, x_2^*\right]^T$.

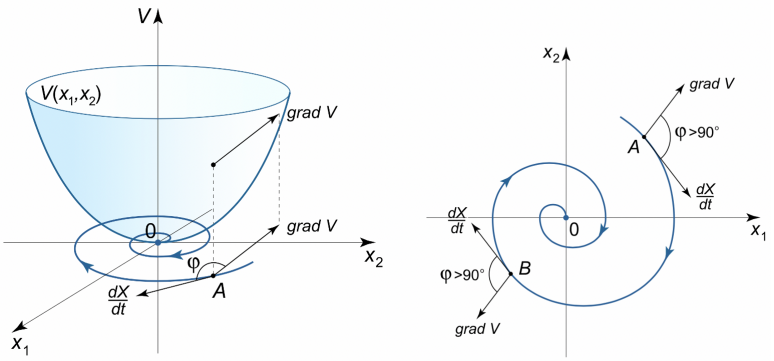

Figure 4.1: Representation of Lyapunov stability of the phase plane origin, for a two dimensional system [93].

4.2.3 MLBS CONTROL SYSTEM DESIGN ON TSE(3)

The rigid body model defined on TSE(3) is described as a second order nonlinear system with a lower triangular form. The BS technique on TSE(3) specializes with a single control law without the definition of intermediate virtual control laws. Moreover, it differs to the conventional BS approach by the presence of an additional term in the CLF: a Morse function to address the stability proof on SO(3). For this reason this controller takes the name of Morse-Lyapunov Backstepping (MLBS) Control. This approach, used for the first control system, reaches an almost globally asymptotically stable controller and is inspired to the previous work [21, 40]. However the control law is extended with

an additional integral term, which allows to reduce significantly the steady state error.

The BS control law that allows both stabilization and tracking of the equation of motion defined in (2.10), is

$$u_c = -\mathbb{I}K_1\dot{l} - \mathrm{ad}^*_{\psi - K_1 l}\mathbb{I}\left(\psi - K_1 l\right) - \mathbb{I}K_2\psi - \mathbb{I}\kappa[0_{1\times 3}, r^T R^T]^T - \mathbb{I}K_3\lambda \tag{4.6}$$

where $K1 = \mathrm{blockdiag}(k_{11}, k_{12})$, $K2 = \mathrm{blockdiag}(k_{21}, k_{22})$,$K3 = \mathrm{blockdiag}(k_{31}, k_{33})$ are positive definite control gain matrices in $\mathbb{R}^{6\times 6}$; κ, is a scalar positive gain; $l(g)$ is the pose configuration function; $\psi(g, \mathbb{V})$ is the pose and velocity configuration function; finally $\lambda = \int_0^t \psi(g, \mathbb{V})d\tau$ is the integral of the pose and velocity configuration function up to time t.

The CLF to prove the stability properties of the control law in Eq.(4.6) can be introduced, at this point. It is based on the summation of two parts, the first one that is a quadratic function of the configuration function ψ. However it is only positive semi definite in $l(g)$ and $\mathbb{V}$. Therefore a second positive semi definite Morse function is added to drive $\psi(g, \mathbb{V})$ and its derivatives to zero. Hence the complete CLF is defined as

$$\mathcal{V} = \mathcal{V}_1 + \mathcal{V}_2 > 0, \qquad \forall (g, \mathbb{V}) \neq (I, 0) \tag{4.7}$$

where

$$\mathcal{V}_1 = \frac{1}{2}\psi^T P\psi + \frac{1}{2}\kappa(1 - k_{12})r^T P_{22} r \qquad \mathcal{V}_2 = \varphi(\mathrm{tr}(A - AR)) \tag{4.8}$$

where $P = \mathrm{blockdiag}(P_{11}, P_{22})$, W are diagonal positive matrices and φ is a C^2 function such that $\varphi(0) = 0$ and $0 \leq \varphi'(x) \leq \alpha(x)$ for all $x \in \mathbb{R}^+$ where $\alpha(\cdot)$ is a class$-K$ function [94, 95]. The second attitude-dependent Morse function has one minimum at $R = I \in \mathsf{SO}(3)$, as well as one maximum and two saddle points [96]. For a positive definite matrix $A = \mathrm{diag}([a_1, a_2, a_3])$ with distinct diagonal entries $a_1 > a_2 > a_3 \geq 1$, the $V_2(R)$ function is positive definite on $\mathsf{SO}(3)$ and vanishes only when $R = I$.

CONFIGURATION FUNCTIONS

In order to use the Lyapunov theory to design the MLBS control law, it is necessary to introduce two configuration functions which allow to work on $\mathsf{TSE}(3)$. The state $x = (g, \mathbb{V}) \in \mathsf{TSE}(3)$ is treated with two smooth configuration functions $l(g)$ and $\psi(g, \mathbb{V})$ such that $l(I) = 0$ and $\psi(I, 0) = 0$. Particularly the functions ψ and l and their derivatives are

$$\begin{aligned} l(g) &= [s^T(R), r^T]^T \qquad \dot{l}(g) = [\dot{s}^T(R, \omega), (Rv)^T]^T \\ \psi(g, \mathbb{V}) &= \mathbb{V} + K_1 l(g) \qquad \dot{\psi}(g, \mathbb{V}) = \dot{\mathbb{V}} + K_1\dot{l} \end{aligned} \tag{4.9}$$

and the function $s(\cdot) : \mathsf{SO}(3) \to \mathbb{R}^3$ and its derivative are defined as

$$\begin{aligned} s(R) &= \sum_{i=1}^{3} a_i \left(R^T e_i\right)^\times e_i = \sum_{i=1}^{3} \left(R^T A^T e_i\right)^\times e_i \\ \dot{s}(R) &= \left(\mathrm{tr}(AR) I_3 - R^T A\right)\omega \end{aligned} \tag{4.10}$$

where $e_i, i = 1, 2, 3$, are the elements of the natural basis in $\mathbb{R}^3$. The time derivative of ψ can be further elaborated using the equation of motion and Eq.(4.6). It is a necessary

step to prove the almost globally asymptotically stable property of the BS control law. Taking the derivative of ψ and substituting first Eq.(2.10) and the control input

$$\begin{aligned}\dot{\psi} &= \dot{\mathbb{V}} + K_1\dot{l} \\ &= \mathbb{I}^{-1}\mathrm{ad}^*_{\mathbb{V}}\mathbb{I}\mathbb{V} + \mathbb{I}^{-1}u + K_1\dot{l} \\ &= \mathbb{I}^{-1}\mathrm{ad}^*_{\mathbb{V}}\mathbb{I}\mathbb{V} + \mathbb{I}^{-1}\{-\mathbb{I}K_1\dot{l} - \mathrm{ad}^*_{\psi-K_1 l}\mathbb{I}\left(\psi - K_1 l\right) - \mathbb{I}K_2\psi - \mathbb{I}\kappa\left[0_{1\times 3}, r^T R^T\right]^T - \mathbb{I}K_3\lambda\} + K_1\dot{l} \\ &= \mathbb{I}^{-1}\mathrm{ad}^*_{\mathbb{V}}\mathbb{I}\mathbb{V} - \mathbb{I}^{-1}\,\mathrm{ad}^*_{\psi-K_1 l}\mathbb{I}\left(\psi - K_1 l\right) - K_1\dot{l} - K_2\psi - \kappa\left[0_{1\times 3}, r^T R^T\right]^T - K_3\lambda + K_1\dot{l}\end{aligned} \tag{4.11}$$

The above expression can be further simplified using the relation $\mathbb{V} = \psi - K_1 l$ and simplifying

$$\begin{aligned}\dot{\psi} &= \mathbb{I}^{-1}\mathrm{ad}^*_{\psi-K_1 l}\mathbb{I}(\psi - K_1 l) - \mathbb{I}^{-1} - \mathrm{ad}^*_{\psi-K_1 l}\mathbb{I}\left(\psi - K_1 l\right) - K_1\dot{l} - K_2\psi - \kappa\left[0_{1\times 3}, r^T R^T\right]^T + K_1\dot{l} \\ &= -K_2\psi - \kappa\left[0_{1\times 3}, r^T R^T\right]^T \\ &= -K_2\psi - \kappa\left[0_{1\times 3}, (Rr)^T\right]^T\end{aligned} \tag{4.12}$$

FIRST TERM IN THE CLF

The first function of the CLF in (4.7), $\mathcal{V}_1$, is taken in consideration. Its differentiation yields to

$$\dot{\mathcal{V}}_1 = \psi^T P\dot{\psi} - \kappa(1-k_{12})r^T P_{22}\dot{r} \tag{4.13}$$

then, substituting Eq.(4.12) into Eq.(4.13) yields

$$\begin{aligned}\dot{\mathcal{V}}_1 &= \psi^T P(-K_2\psi - \kappa\left[0_{1\times 3}, (Rr)^T\right]^T) + \kappa(1-k_{12})r^T P_{22}\dot{r} \\ &= \psi^T(-PK_2)\psi - \kappa\psi^T P\left[0_{1\times 3}, (Rr)^T\right]^T + \kappa(1-k_{12})r^T P_{22}\dot{r}\end{aligned} \tag{4.14}$$

The second term can be even rewritten, recalling that $\psi = \mathbb{V} + K_1 l$

$$\begin{aligned}\dot{\mathcal{V}}_1 &= \psi^T(-PK_2)\psi - \kappa(\mathbb{V} + K_1 l)^T P[0_{1\times 3}, (Rr)^T]^T + \kappa(1-k_{12})r^T P_{22}\dot{r} \\ &= \psi^T(-PK_2)\psi - \kappa[\omega^T + k_{11}s^T(R), v^T + k_{12}r^T]^T P[0_{1\times 3}, (Rr)^T]^T + \kappa(1-k_{12})r^T P_{22}\dot{r} \\ &= \psi^T(-PK_2)\psi - \kappa(v^T + k_{12}r^T)P_{22}(Rr) + \kappa(1-k_{12})r^T P_{22}\dot{r}\end{aligned} \tag{4.15}$$

Using the Backstepping technique it is supposed that the kinematic differential equation in Eq.(2.10) can be stabilized by a state feedback control law of the form $\mathbb{V} = -l(g)$ [95]. Therefore the components return

$$\omega = -s(R), \qquad v = -r \tag{4.16}$$

and the substitution in Eq.(4.15) leads to

$$\begin{aligned}\dot{\mathcal{V}}_1 &= \psi^T(-PK_2)\psi - \kappa(-r^T + k_{12}r^T)P_{22}(Rr) + \kappa(1-k_{12})r^T P_{22}\dot{r} \\ &= \psi^T(-PK_2)\psi - \kappa(-1+k_{12})r^T P_{22}(Rr) + \kappa(1-k_{12})r^T P_{22}\dot{r}\end{aligned} \tag{4.17}$$

Finally the last term can be rewritten reminding the kinematic equation $\dot{r} = Rv$ and subsequently using Eq.(4.16)

$$\begin{aligned}\dot{\mathcal{V}_1} &= \psi^T(-PK_2)\psi - \kappa(-1+k_{12})r^T P_{22}(Rr) + \kappa(1-k_{12})r^T P_{22}Rv \\ &= \psi^T(-PK_2)\psi - \kappa(-1+k_{12})r^T P_{22}(Rr) - \kappa(1-k_{12})r^T P_{22}Rr \\ &= \psi^T(-PK_2)\psi + [-\kappa(-1+k_{12}) - \kappa(1-k_{12})]r^T P_{22}Rr \\ &= \psi^T(-2PK_2)\psi\end{aligned} \tag{4.18}$$

which is quadratic in ψ, hence with K_2, P positive definite control gain matrices, $\dot{V}_1 \leq 0$. As a result the first term in the CLF is positive semi definite.

SECOND TERM IN THE CLF

The second Morse function of the CLF in (4.7), $\mathcal{V}_2$, is further investigated. Since $\frac{d}{dt}tr(\cdot) = tr(\frac{d(\cdot)}{dt})$, and using the chain rule, it can be differentiated as

$$\dot{\mathcal{V}_2} = -\phi^{'}(\text{tr}(A - AR))tr(AR\omega^{\times}) \tag{4.19}$$

where the property $d(tr(A-AR)) = d(tr(-AR)) = -tr(A\dot{R}dt)$ and the rotational kinematics $\dot{R} = R\omega^{\times}$ are used. Without loosing generality, let $\phi(\cdot)$ be defined as $\phi(x) = k_3 x$ ($k_3 > 0$). Then its derivative becomes $\dot{\phi} = k_3$

$$\dot{\mathcal{V}_2} = -k_3 tr(AR\omega^{\times}) \tag{4.20}$$

However, since $\mathbb{V} = -l(g)$ then $\omega = -s(R)$ and

$$\dot{\mathcal{V}_2} = k_3 tr(ARs^{\times}(R)) \tag{4.21}$$

The following properties hold for all $A \in \mathbb{R}^{3\times 3}$ and $b \in \mathbb{R}^3$

$$\begin{aligned} &tr(Ab^{\times}) = b^T(A^T - A)^{\vee}, \quad (\cdot)^{\vee\times} = (\cdot) \\ &tr(A) = \sum_{i=1}^{3} = e_i^T A e_i \\ &(A^T - A)^{\vee} = \sum_{i=1}^{3} = e_i^{\times} A e_i \end{aligned} \tag{4.22}$$

Using the properties and the definition of $s(R)$ in Eq.(4.10):

$$\begin{aligned} tr(ARs^{\times}(R)) &= s^T(R)((AR)^T - AR)^{\vee} \\ &= s^T(R)\sum_{i=1}^{3} = e_i^{\times}(AR)e_i = -s^T(R)\sum_{i=1}^{3}(R^T A^T e_i)^{\times} e_i \\ &= -s^T(R)s(R) \end{aligned} \tag{4.23}$$

Therefore the Morse function derivative on the trajectory can be rewritten

$$\dot{\mathcal{V}_2} = -k_3 s^T s \tag{4.24}$$

and it is negative semi definite on SO(3). The Morse function $\mathcal{V}_2$ has a global minimum when the attitude rotation matrix is the identity matrix, i.e $R(0,0,0)$. On the other hand, there are two saddle points and a global maximum related to π rad rotations of the body frame with respect to the inertial frame about any of the body axes, i.e $R(\pi,0,0), R(0,\pi,0), R(0,0,\pi)$.

Finally the time derivative of the CLF function can be obtained with the sum of the two contributions in Eq.(4.18)-(4.24)

$$\dot{\mathcal{V}} = -k_3 s^T s - \psi^T (2PK_2)\psi \tag{4.25}$$

This equation is negative semi definite. Particularly there is the asymptotically stable equilibrium $x = (I,0)$ and $x = (R(\pi,0,0),0), x = (R(0,\pi,0),0), x = (R(0,0,\pi,),0)$which are three saddle equilibria with stable manifolds of zero Lebesgue measure. Since the stable manifolds of the last three equilibrium points have zero measure on TSE(3), the first equilibrium point is almost globally asymptotically stable [21]. The design procedure just described defines the solution for a stabilization problem, which means that for $t \to \infty$, the state $x = (g,\mathbb{V}) \to (I,0)$. It is also interesting to study the case of a tracking problem, in which a desired or reference state is defined $x_{ref} = (g_{ref},\mathbb{V}_{ref})$ and it is required that for $t \to \infty$, the state $x = (g,\mathbb{V}) \to (g_{ref},\mathbb{V}_{ref})$. Such problem can be solved using the same procedure as that described above, with in addition needs a change of coordinates. Instead of treating the state $x = (g,\mathbb{V})$, the error of the state with respect to the reference state is considered $\delta x = (\delta g, \delta\mathbb{V})$. Hence, the MLBS techniques guarantees that for $t \to \infty$, the state $\delta x = (\delta g, \delta\mathbb{V}) \to (I,0)$.

Figure 4.2 represents the model-based scheme of the discussed control algorithm. It is emphasized that the reference states come from the guidance system, while the estimated states from the navigation system. Once the required control input is computed on the basis of the estimated state error, the actuators moderate the output of the control system.

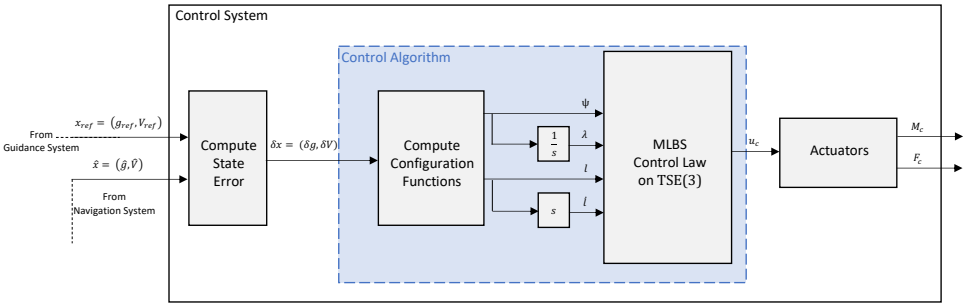

Figure 4.2: Representation of the Simulink model for the control system with the MLBS control algorithm on TSE(3).

4.3 SLIDING MODE CONTROL ON TSE(3)

4.3.1 SLIDING MODE CONTROL BACKGROUND

In the design procedure of any practical control system, there is always some discrepancy between the actual system to be controlled and its mathematical model used for the controller design. These mismatches may arise from unknown parameters, unmodeled/simplified plant dynamics or unknown external disturbances [41]. Conventional linear control systems, such as PID controller, are not able to overcome these issues and in the presence of these disturbances/uncertainties the closed-loop system may also diverge. This problem led the control engineers to the development of robust control methods which are supposed to be robust to disturbances/uncertainties. According to [92], there are basically two complementary approaches to dealing with the aforementioned mismatches: 1) Robust Control techniques which is discussed in this section; 2) Adaptive Control techniques, which deal with uncertainties with a variable structure which is updated during operation.

The Sliding Mode Control (SMC) is considered as an efficient technique to withstand external disturbances and model uncertainties, and has been widely adopted for spacecraft applications [44]. It is a systematic approach to the problem of maintaining stability and consistent performance when modeling uncertainties occur. The main advantages of SMC, including robustness, finite-time convergence, and reduced-order compensated dynamics, have been proved in numerous works [97, 46, 47]. The SMC is an efficient method for nonlinear systems, characterized by a solid theoretical foundations based on Lyapunov theory described in Section 4.2.2.

The robustness of the SMC to the plant uncertainties is obtained at the price of extremely high control activity. Generally the switching nature of the SMC is not desirable for mechanical systems, where it is required to have continuous force or moment control inputs. In addition this switching nature may excite some neglected plant dynamics [92]. However, the problem at hand consists in a spacecraft actuated with thrusters, which may also be characterized by a discontinuous nature. For this reason the SMC is a suitable control method to be implemented due to its consistency with these actuation systems [47, 98].

4.3.2 SMC CONTROL SYSTEM DESIGN ON TSE(3)

The SMC approach consists in defining a so-called sliding surface σ, which is a subset of the state space on which the trajectory of the plant is desired to lie. A feedback law is realized such that this surface will be attractive and invariant, i.e. the plant trajectory evolves towards this surface and, once there, it stays close to it. The sliding surface, $\sigma \in \mathbb{R}^{6\times 1}$, is defined as a function of pose and velocity

$$\sigma = c_1\mathbb{V} + c_2 l(g) + c_3\lambda \tag{4.26}$$

where $c1 = \text{blockdiag}(c_{11}, c_{12})$,$c2 = \text{blockdiag}(c_{21}, c_{22})$,$c3 = \text{blockdiag}(c_{31}, c_{32})$ are positive definite diagonal matrix, $\psi(g,\mathbb{V}), l(g), \lambda = \int_0^t \psi(g,\mathbb{V})d\tau$ is the integral of the pose and velocity configuration function up to time t. are the functions already used for the

MLBS control design (Section 4.2.3). The third integral term is added since it reduces meaningfully the steady state error. The addition of an integral action to define the sliding surface has proved to lead to good results in literature [99, 100, 101]. The SMC control force and moment input is defined as

$$u = u_{eq} + u_d \tag{4.27}$$

with

$$u_{eq} = -\mathrm{ad}^*_{\mathbb{V}}\mathbb{I}\mathbb{V} - \frac{c_2}{c_1\mathbb{I}^{-1}}\dot{l}(g) - \frac{c_3}{c_1\mathbb{I}^{-1}}\psi(g,\mathbb{V}) \qquad u_d = -K_\sigma \mathrm{sign}(\sigma) \tag{4.28}$$

where the $K_\sigma = -\frac{c_4}{c_1\mathbb{I}^{-1}} = \mathrm{blockdiag}(K_{\sigma,M}, K_{\sigma,F})$ is a positive definite diagonal matrix whose has to be selected properly in order to having the sliding mode without the unmodeled dynamics [102]. The first contribute is known as equivalent control, and it represents the control function which needs to be applied to the system after reaching the sliding surface to ensure that the system trajectory stays on this surface thereafter. This feature is known as invariant property and the control input guarantees the solution of the problem $\dot{\sigma} = 0$. The second contribute is known as discontinuous control and it ensures that the system trajectory evolves towards the sliding surface. This feature is known as attractive property and the switching control action allows the system trajectory to reach this surface [103]. In order to achieve the asymptotic convergence of $l(g)$ and $\psi(g,\mathbb{V})$ to zero, i.e. $\lim_{t\to\infty} l(g), \psi(g,\mathbb{V}) = 0$ with a given convergence rate, in the presence bounded disturbance, the control input in Eq.(4.27) has to drive the variable σ in Eq.(4.26) to zero in finite time. This feature can be guaranteed by applying the Lyapunov stability theory to the σ dynamics, which is basically the derivative of Eq.(4.26)

$$\dot{\sigma} = \dot{\psi}(g,\mathbb{V}) = c_1\dot{\mathbb{V}} + c_2\dot{l}(g) + c_3\psi(g,\mathbb{V}) \tag{4.29}$$

The asymptotic stability of the above equation to the equilibrium point $\sigma = 0$ can be proved introducing the following CLF

$$\mathcal{V} = \frac{1}{2}\sigma\sigma^T \tag{4.30}$$

whose derivative is

$$\dot{\mathcal{V}} = \sigma\dot{\sigma}^T \tag{4.31}$$

Substituting Eq.(4.29) and then Eq.(2.10)

$$\begin{aligned}\dot{\mathcal{V}} =& \sigma(c_1\dot{\mathbb{V}} + c_2\dot{l} + c_3\psi(g,\mathbb{V}))^T \\ =& \sigma[c_1(\mathbb{I}^{-1}\mathrm{ad}^*_{\mathbb{V}}\mathbb{I}\mathbb{V} + \mathbb{I}^{-1}u) + c_2\dot{l} + c_3\psi(g,\mathbb{V})]^T\end{aligned} \tag{4.32}$$

using the control law defined in Eq.(4.27) the control linear and angular accelerations can be substituted

$$\begin{aligned}\dot{\mathcal{V}} &= \sigma[c_1(\mathbb{I}^{-1}\mathrm{ad}^*_{\mathbb{V}}\mathbb{I}\mathbb{V} + \mathbb{I}^{-1}u) + c_2\dot{l} + c_3\psi(g,\mathbb{V})]^T \\ &= \sigma[c_1\mathbb{I}^{-1}\mathrm{ad}^*_{\mathbb{V}}\mathbb{I}\mathbb{V} + c_1\mathbb{I}^{-1}(-\mathrm{ad}^*_{\mathbb{V}}\mathbb{I}\mathbb{V} - \frac{c_2}{c_1\mathbb{I}^{-1}}\dot{l}(g) - \frac{c_3}{c_1\mathbb{I}^{-1}}\psi(g,\mathbb{V}) - \frac{c_4}{c_1\mathbb{I}^{-1}}\mathrm{sign}(\sigma)) + c_2\dot{l} + c_3\psi(g,\mathbb{V})]^T \\ &= -\sigma[\frac{c_4}{c_1\mathbb{I}^{-1}}\mathrm{sign}(\sigma)]^T \\ &= -\frac{c_4}{c_1\mathbb{I}^{-1}}||\sigma|| = -K_\sigma||\sigma||\end{aligned} \tag{4.33}$$

since $\dot{\mathbb{V}} < 0$ for $\sigma \neq 0$ the stability of the equilibria point is proved. In the CLF derivative $||\cdot||$ is the 1−norm of the sliding surface, i.e. $||\sigma|| = \sum_1^6 |\sigma_i|$. To be precise, this proof only guarantees the local stability of the equilibria $\sigma = 0$ since it can also happen that σ is zero because $\mathbb{V} = -K_1 l$. The CLF should be extended with the term $\frac{1}{2}\kappa(1-k_{12})r^T P_{22} r$ as done for the MLBS control design, in order to guarantee the global stability. This step is avoided since in this work the equivalent control is omitted in favor of an easier control law, which is totally independent on the knowledge of the mathematical model of the plant. In fact, neglecting u_{eq} the SMC uses only the state measurements to determine the sliding surface and returns a comparable performance. In addition, the equivalent control u_{eq} is not usually implemented since, in case of input disturbances, it would need of their model. The equivalent control represents the effect of the high-frequency switching control u_d. For this reason, according to [41], u_{eq} is achieved using a low-pass filter (LPF) on u_d

$$u_{eq} \approx -LPF(u_d) \tag{4.34}$$

Therefore, a first order SMC law is used for the second control system, i.e.

$$u = -K_\sigma \text{sgn}(\sigma) \tag{4.35}$$

Fig.4.3 depicts the behavior of the system trajectory in the state space, for a two states system under the SMC. The sliding surface is a line in the phase plane containing the equilibria point $\sigma = 0$. Starting from any initial condition $(x_0, \dot{x}_0)$, the state trajectory reaches the sliding surface in a finite time (reaching phase), and then slides along the surface towards the origin exponentially (sliding mode). In summary the idea behind the SMC consists in constructing a well-behaved function of the tracking error, σ, and then select the feedback control law such that it remains a Lyapunov-like function of the closed-loop system, despite the presence of model inaccuracy and of disturbances. The discontinuous nature of the control law in Eq.(4.35) leads to a phenomenon called chattering, which is highlighted in Fig.4.3. It basically consists in high frequency oscillations around the sliding surface. This phenomenon is highly undesirable in practical situation, since it involves high control activity and in addition it may excite high frequency dynamics neglected in the model. The most obvious solution to attenuate the chattering is to make the control law Eq.(4.35) continuous/smooth to approximate the discontinuous sgn$(\cdot)$ function. The most common solution in literature consist in the use of: 1) hyperbolic tangent function, $\tanh(\eta\sigma)$, with $\eta \geq 100$; 2) sigmoid function, $\frac{\sigma}{|\sigma|+\eta}$, with $\eta \leq 10$ [101].

As for the first control system, the stabilization procedure just described guarantees that for $t \to \infty$, the state $x = (g, \mathbb{V}) \to (I, 0)$. However the procedure can be extended to the tracking case with the precaution of defining the sliding surface as a function of the error of the state with respect to the reference state is considered, i.e. $\delta x = (\delta g, \delta \mathbb{V})$.

Figure 4.4 represents the model-based scheme of the discussed control algorithm. It is emphasized that the reference states come from the guidance system, while the estimated states from the navigation system. Once the required control input is computed on the basis of the estimated state error, the actuators moderate the output of the control system.

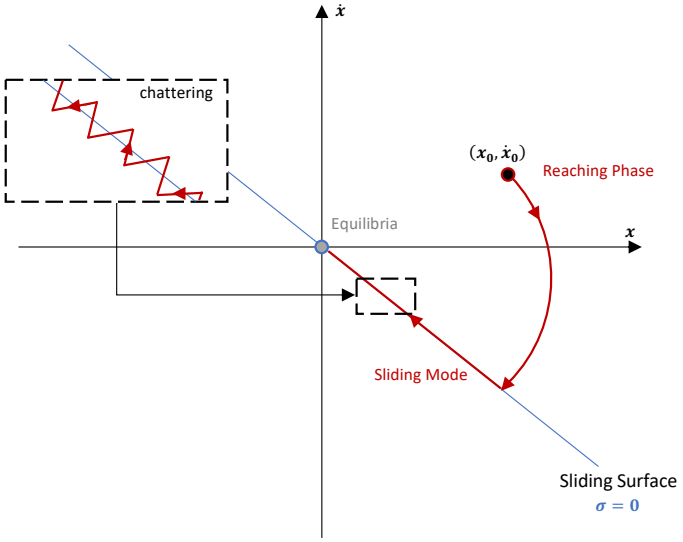

Figure 4.3: Graphical interpretation of the sliding mode control in the state space.

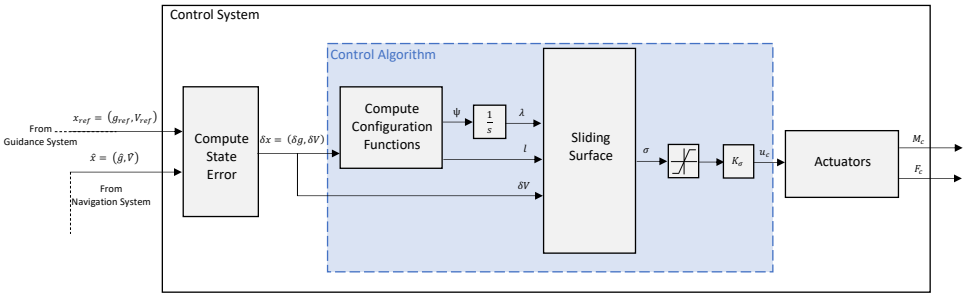

Figure 4.4: Representation representative of the Simulink model for the control system with the SMC control algorithm on TSE(3).

Chapter 5

Simulation Results and Discussion

This final chapter is committed to the simulation results and discussion. First, the variational integrator's accuracy is investigated from the perspective of the orbit propagation. The spacecraft open loop dynamics are analyzed and compared to the one of a point mass spacecraft. Then, the navigation systems singularly are tested in open-loop in different of case studies. The control system performances are analyzed in the same manner. Finally different combinations of navigation and control systems are extensively tested and compared to each other in different case studies.

5.1 Orbit Propagation

The orbit propagation requires the numerical solution of a system of differential equations, which can describe a large class of problems: planetary orbiters, transfer orbits, planetary systems, re-entry or solar system simulations. According to [104], the problem can be formulated in more general terms as follow

$$\frac{dx}{dt} = f(x, t; p) \tag{5.1}$$

and requires the definition of the following blocks:

- Environment: the properties of the physical surroundings, defined through p. Different environment models may be defined, such as: atmosphere model (atmospheric density, temperature, etc.), ephemeris (body state as a function of time), shape model, vehicle's properties (mass, inertia, aerodynamics coefficients, etc.). Each body concurring in the simulation can contain a list of environment models. Basically this framework includes/computes all the physical properties used in simulation.

- Acceleration: the terms to be included in equations of motion, represented by what is contained in f. If the environment list assigns the properties of the bodies, the acceleration block defines how these properties are used to compute the dynamics. Different source of acceleration may be taken into account: central gravity, which is the point mass acceleration due to a single central body and would results in a Keplerian orbit; spherical harmonics gravity, which models the gravitational interaction through spherical harmonics; the third body gravitational attraction; the aerodynamics or the radiation pressure acceleration.

- Propagator: the formulation of the equation of motion, defined through x. It does not need to be in Cartesian coordinates. The propagator has the role of defining the type of dynamics (translational, rotational, coupled, mass, etc.) and the equations that need to be solved (Encke, Cowell, etc.)

- Integrator: solver for the equation of motion, which allows to obtain $x(t)$. The integrator block defined the integration scheme to be used to solve the equations numerically (Euler, Runge Kutta, etc.) and the settings for it (time step, relative tolerance, etc.)

In this work, an irregular asteroid is taken as central body and the translation and rotational spacecraft dynamics are both propagated considering the nonlinear coupling between them. The spacecraft equation of motion Eq.(2.10) are not propagated with standard propagators, since the state is expressed on $\mathsf{TSE}(3)$. There are two bodies concurring in the simulation, and just the gravitational acceleration of the asteroid on the spacecraft is considered and modeled with spherical harmonics C_{20} and C_{22}. The gravitational influence of the spacecraft on the asteroid is thus neglected. Since no other bodies concur in the simulation, the reference frame is assumed to be fixed with the asteroid and its dynamics is not propagated. Hence, the environment includes all the physical properties of the two bodies needed to write Eq.(2.10) and Eq.(2.16)-(2.19). For the most of astrodynamics problems, analytical solutions are not (readily) available, and one has to numerically integrate a propagation model that best represents the dynamics of the system at hand. In the context of numerical astrodynamics, the choice of a numerical integrator is a design problem since the results can be heavily influenced by the integration method of the accuracy.

5.1.1 NUMERICAL INTEGRATOR

The differential equations representing the spacecraft dynamics are numerically integrated using a fixed time step Lie group variational integrator (LGVI). Its main feature is the preservation of geometric properties of the system. This integration scheme is applied directly on the nonlinear manifold $\mathsf{SE}(3)$, where the discretized Hamiltonian is used. The specific variational integrator formulation used in this thesis is described in detail in [105, 106] and used in [48]. The variational principle yields to the discrete equations of motion and their manipulation allows to derive a symplectic Euler variational integrator of the form:

$$\begin{bmatrix} R_{k+1} & r_{k+1} \\ 0 & 1 \end{bmatrix} = \begin{bmatrix} R_k & r_k \\ 0 & 1 \end{bmatrix} \begin{bmatrix} \exp(h\omega_k) & hB_{\exp}(h\omega_k)v_k \\ 0 & 1 \end{bmatrix} \tag{5.2}$$

$$C_{\exp}^T(h(\omega_k, v_k))\mathbb{I}\mathbb{V}_k - C_{\exp}^T(-h(\omega_{k-1}, v_{k-1}))\mathbb{I}\mathbb{V}_{k-1} = hu((R_k, r_k), \mathbb{V}_{k-1}) \tag{5.3}$$

where h is the time step, the map $\mathrm{B}_{\exp} : \mathbb{R}^3 \to \mathbb{R}^{3,3}$ is equal to

$$\mathrm{B}_{\exp}(\omega) = \begin{cases} I_3 & \text{if } \omega = 0 \\ I_3 + \left(\frac{1-\cos\|\omega\|}{\|\omega\|}\right)\frac{\widehat{\omega}}{\|\omega\|} + \left(1 - \frac{\sin\|\omega\|}{\|\omega\|}\right)\frac{\widehat{\omega}^2}{\|\omega\|^2} & \text{if } \omega \neq 0 \end{cases} \tag{5.4}$$

and the map $C_{\exp} : \mathbb{R}^6 \to \mathbb{R}^{6,6}$ is

$$C_{\exp}(\omega, v) = I_6 - \frac{1}{2}\mathrm{ad}_{[\omega,-v]} + \frac{1}{12}(\mathrm{ad}_{[\omega,-v]})^2 \tag{5.5}$$

For an implicit step, the discussed holonomic integrator takes $(R_k, r_k, \omega_{k-1}, v_{k-1})$, the matrices $B_{\exp}$ and $C_{\exp}$ are computed with Eq.(5.4)-(5.5) respectively, Eq.(5.3) is solved with a Newton-type solver for (ω_k, v_k), finally Eq.(5.2) allows the update for (R_{k+1}, r_{k+1}).

5.1.2 INTEGRATOR ACCURACY

As already introduced, it is important to analyze the error behavior of the presented integrator, in order to select the proper time step. Typically, in the preliminary phases of a mission design, a requirement on the accuracy is formulated [107]. With this accuracy requirement, the best propagator-integration combination is selected performing quantitative analysis. Since the propagator and the integrator have been already chosen, the only degree of freedom is the integrator time step. It can be selected on the basis of the integrator error behavior analysis. In order to do so, a benchmark solution is required. Clearly it can't be an exact solution to the problem at hand, but it will be accurate enough such that further analyses can be developed.

The integrator algorithms solve the equation of motion thus obtaining a numerical solution. The latter one, is an approximation of the real solution which is not obtainable analytically. It is emphasized that the performance of such numerical procedures are influenced by the simulated physical situations. For instance, if the propagated dynamics evolves with high rate, an high time step can lead to large errors since the integrator wouldn't be able to follow the dynamics change. Clearly the error behavior analysis can not be developed for all the possible physical situations, instead a representative case study has to be selected. In this work, the chosen representative situation is the one which may show better the coupling between the translational and rotational motions, i.e. the open-loop (uncontrolled) spacecraft dynamics. The accuracy requirement is given on the position error, since it is influenced by the evolution of all the other spacecraft state variable. Particularly its derivative depends on R and v, but both of them depends on ω. For the physical situation at hand, it is chosen to have an integration accuracy in the order of $1\,m$. Since the integration error are cumulative in time, it is needed to define a propagation time. When the navigation and control systems will be applied to the vehicle, integration times in the order of few Earth days will be considered. However, in order to present a more robust and conservative error analysis, a propagation of 10 Earth days is considered here.

Ideally, the LGVI should be benchmarked with the analytical solution representing aforementioned physical situation. However it is not possible to obtain a closed form solution of the orbit propagation when spherical harmonics are considered. Therefore a benchmark numerical solution is needed to assess the LGVI accuracy. This 'ground truth' is chosen to be the point mass propagation with Runge-Kutta 7^{th} order integrator (RK7)

already implemented in Simulink. Moreover, the acceleration model is a simple point mass gravity acceleration. With this procedure it is possible to quantify the LGVI accuracy with the classical Kepler orbit analytical solution. The spacecraft initial conditions are selected such that the outcome would results in a circular closed orbit. Fig. 5.1 shows the position error history between the RK7 numerical solution and the analytical solution for different time steps (left) and the maximum position error for different time steps (right). The position error curves increase over time, and it is expected since the truncation errors are cumulative over time. Particularly under the assumption of dominating truncation errors, the position error behaves approximately as a polynomial in Δt. It is confirmed by the right figure, where the maximum position error increases linearly in logarithmic scale. When the time step becomes small, a more irregular and erratic behavior of the curves can be observed. Since the numerical and the analytical solutions are very close, the rounding errors start to become relevant. Fig. 5.1 shows that a time step of 100 s leads to a precision in the order of mm and the minimum position error $o(10^{-13})$ km can be approximately obtained with $\Delta t = 0.5$ s. Since the point mass propagation does not require a large computational effort, $\Delta t = 0.5$ s is chosen for the benchmark solution.

Now that a benchmark solution is available, the same procedure described above is applied to the LGVI and the spherical harmonics gravity of the irregular central body can be included in the acceleration models. As result Fig.5.2 is obtained. Conversely to the previous case, now the position error curves are not characterized by the rounding errors and the their order of magnitude is undoubtedly higher. It is somehow expected since the rigid body propagation is characterized by the coupling between the translational and rotational dynamics. A larger difference with respect the point mass propagator is unavoidable. However the information on the LGVI accuracy can be still obtained. The requirement accuracy of the error less than $1\,m$ can be obtained with all the time steps $\leq 10\,s$. Particularly, since the LGVI does not take an high computational time, it is chosen a time step of $1\,s$ which corresponds to an accuracy of approximately $0.1\,m$.

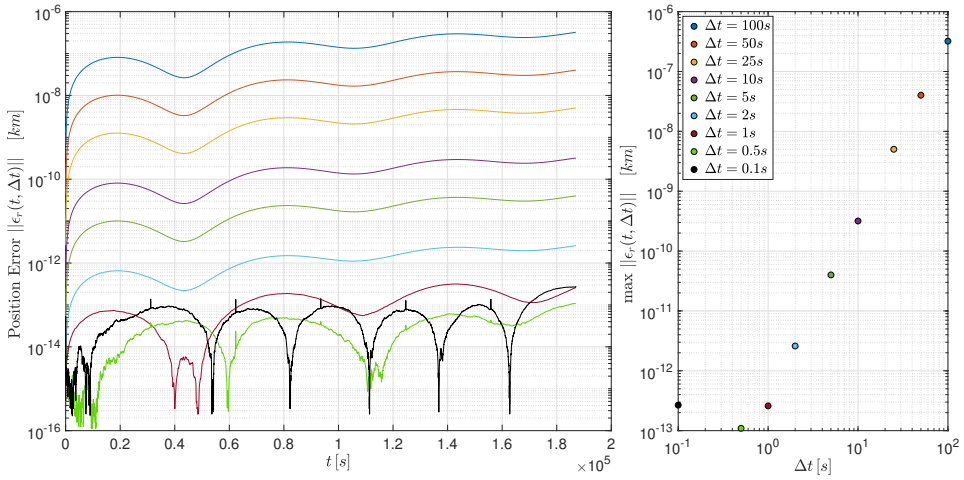

Figure 5.1: Position error $\|\epsilon_r(t,\Delta t)\|$ as a function of time t (left) and maximum position error as function of Δt (right). Position error between point mass propagator with RK7 integrator and analytical solution, obtained with Bennu central gravity.

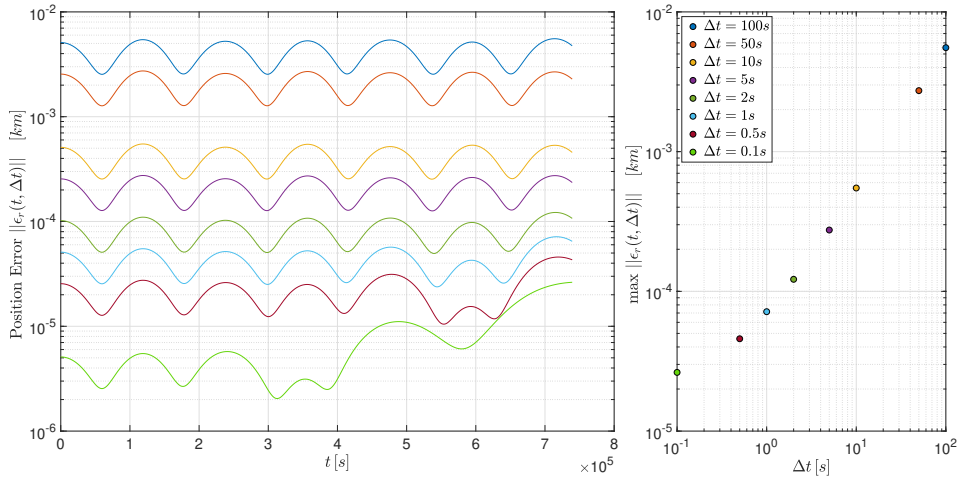

Figure 5.2: Position error $\|\epsilon_r(t,\Delta t)\|$ as a function of time t (left) and maximum position error as function of Δt (right). Position error between rigid body on $\mathsf{TSE}(3)$ propagator with LGVI integrator and point mass propagator RK7 integrator, obtained with Bennu spherical harmonics gravity.

5.2 OPEN-LOOP DYNAMICS MODEL AND SIMULATION RESULTS

The implementation of the simple model consisting in the spacecraft dynamics on $\mathsf{TSE}(3)$ ad the gravitational effect is shown in Fig.5.3. Since the objective is to simulate the open loop response of the system, the control force and moment $u_c = [M_c, F_c]$ are set to zero, as well as the disturbance force and moment $u_d = [M_d, F_d]$. There is only one environmental effect which is represented by the gravitational field of the irregular central body. The "Spacecraft Dynamics on $\mathsf{TSE}(3)$" block contains Eq.(2.10) and the integration using the algorithm previously discussed. The "Gravitational Effect" block makes use of Eqs.(2.16)-(2.19).

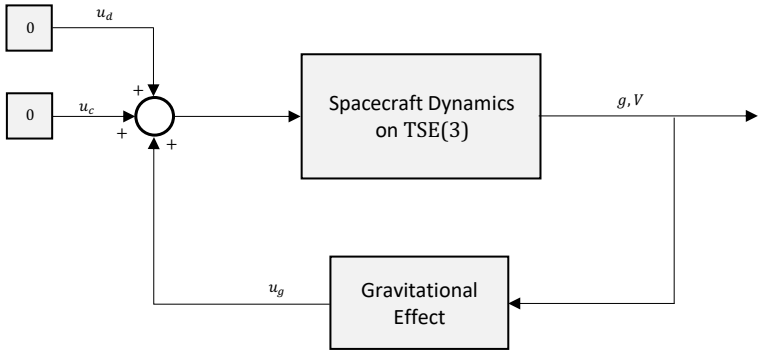

Figure 5.3: Schematic representation of the Simulink model for the open-loop dynamics on $\mathsf{TSE}(3)$

The highly perturbed environment in which the spacecraft operates is primarily induced by the irregular shape of the central body. Spherical harmonics model is used to approximate the gravitational field of the central body, as described in Section 2.3. The spacecraft orbits around the asteroid Bennu, whose properties are given in Tab.2.1. Moreover, the spacecraft parameters and initial conditions are given in Tab.5.1. The inertia matrix is selected according to properties of the Delfi I satellite. The numerical simulation is carried out for 100 Earth days with a time step of $10\,s$, which according to the previous analysis leads to a precision of $\approx 1m$.

The traditional approach assumes a point mass spacecraft model to propagate the translational motion of the spacecraft, while the attitude motion is considered to be completely decoupled from it. The model used in this work, instead, describes the rigid body motion including the coupling between the rotational and translational motion. For this reason, it is interesting to compare the results for the rigid body spacecraft model on $\mathsf{TSE}(3)$ and the point mass spacecraft on Euclidean space. The orbit-attitude coupling on the spacecraft dynamics in proximity of small irregular bodies can have a strong impact and also may lead the spacecraft to rapidly diverge [58].

Fig.5.4 shows the differences in trajectory between the rigid body spacecraft model on $\mathsf{TSE}(3)$ obtained with the LGVI, and the point mass spacecraft on Euclidean space obtained with the RK7 integrator. The orbits are shown in the BCI frame. It can be seen how the satellite orbit for the point mass remains confined in the orbit plane, while the rigid

body's orbit does not. To get a better idea of the orbital parameter variation, in Fig.5.5 some Kepler orbit and the orbital energy are shown with respect the time, for both the spacecrafts. The asteroid's oblatness (C_{20} zonal harmonics) is the largest perturbation of the gravitational field [108]. It causes the regression of the ascending node for both the spacecraft models, and in addition C_{20} is responsible of the oscillation of the point mass Kepler elements [109]. Clearly, without C_{20}, C_{22} perturbations, they would have been constant and the trajectory would have delineated a Keplerian orbit. The rigid body quantities are subjected to a high frequency component which may be induced by the satellite's tumbling.

In Fig.5.6 the rigid body spacecraft state variables are shown, where the rotation matrix is represented through the Euler angles 123 sequence. The influence of the attitude on the translational motion is clear by looking at the velocity in the BCI frame. It can be seen that the velocity components are characterized by a faint oscillation. Finally Fig.5.7 depicts the rigid body spacecraft force and moment due to the gravitational field of the irregular central body in SBF. The moment's third component is not zero, but it is of an order of magnitude smaller than the first two since the spacecraft has a low inertia components in correspondence of the z body axis.

Table 5.1: Spacecraft parameters and initial conditions for its relative states of with respect to asteroid Bennu.

Parameter	Values
Relative Position $[km]$	$r_0 = \begin{bmatrix} 2 & 0 & 0 \end{bmatrix}^T$
Relative Attitude $[deg]$	$\theta_0 = \begin{bmatrix} 30 & 60 & 70 \end{bmatrix}^T$
Relative Velocity $[km/s]$	$v_0 = R_0^T \sqrt{\frac{\mu}{r_0}} \begin{bmatrix} 0 & 1 & 0 \end{bmatrix}^T$
Relative Angular Velocity $[deg/s]$	$\omega_0 = \begin{bmatrix} 0.0172 & 0.0286 & 0.0573 \end{bmatrix}^T$
Mass $[kg]$	$m = 850$
Inertia $[kg\,m^2]$	$J = \begin{bmatrix} 124.531 & 124.586 & 0.704 \end{bmatrix}^T$

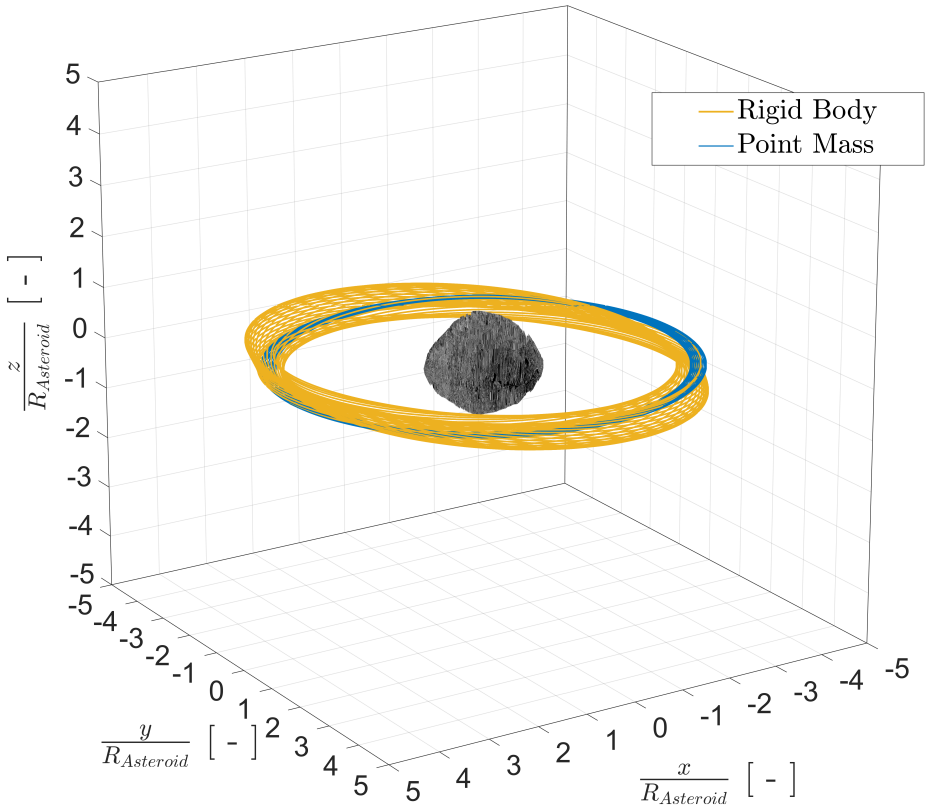

Figure 5.4: Spacecraft motion around asteroid Bennu. Blue and yellow trajectories represent rigid body and point mass motion respectively.

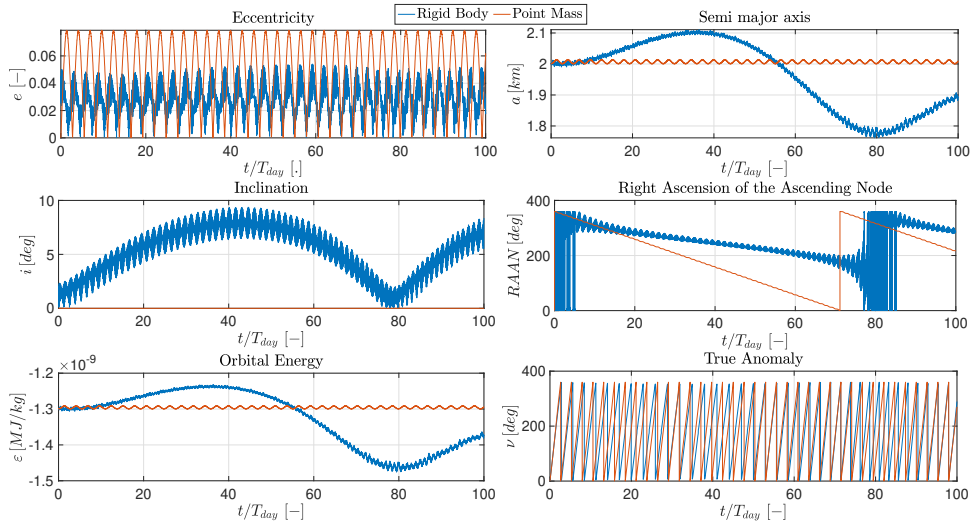

Figure 5.5: Some of the Kepler elements with respect to Bennu as a function of time. Blue and red lines represent rigid body and point mass motion respectively.

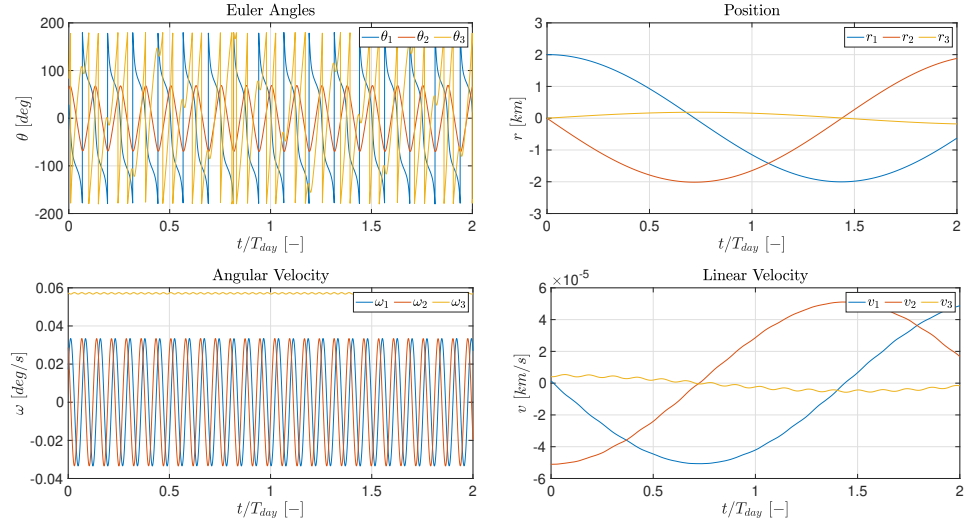

Figure 5.6: Rigid body spacecraft Euler angles, position in BCI frame, angular velocity and linear velocity in BCI frame. The time axis is limited to 2 Earth days propagation.

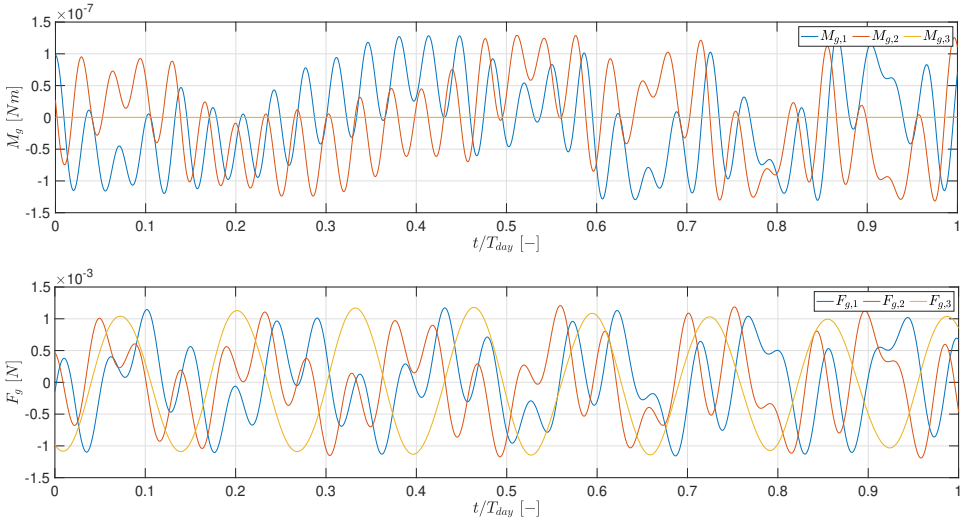

Figure 5.7: Gravitational force and moment exerted by the central body on the rigid body spacecraft, in the SBF. The time axis is limited to 1 Earth day propagation.

5.3 NAVIGATION SYSTEMS COMPARISON

Generally the performance analysis of any navigation system aims to develop a comprehensive evaluation of the algorithms from several aspects, such as parameter and noise sensitivity, complexity, sample time, etc. [110]. In this work, the navigation algorithms performance evaluation is conducted in agreement with [65], where a comparative study of EKF and a sliding mode observer is conducted applied to orbital determination for formation flying about the $L(2)$ Lagrange point. Particularly the emphasis is given to the following specifications:

- Sensitivity to measurement noise
- Sensitivity to parameter uncertainty
- Sampling frequency
- Input Disturbance

where the first one is generally the most important, since the measurement noise is the results of the sensors used in the navigation system. In this section, a case study scenario is introduced and the tuning of the navigation algorithm is discussed. Subsequently, their performance are tested in different test cases, according to the above points. It is emphasized that the performance evaluation is conducted independently from the control algorithms already discussed. Therefore the navigation systems are not run in the-loop with the control systems, hence their estimate are not fed into the control system. In these evaluations, the MLBS control system has been used.

5.3.1 NOMINAL CASE STUDY

In order to investigate the navigation systems performance, a nominal case study is selected. The scenario consists in the spacecraft with the characteristics given in Tab. 5.1, which has to reach and keep a closed orbit around the Saturnian moon Pan (Tab. 2.2). The reference position is represented by a closed circular orbit, not necessarily in the equatorial plane, parameterized as

$$r_{ref}(t) = R_o \left[r_o \sin(n_o t),\, r_o \cos(n_o t),\, 0\right]^T \tag{5.6}$$

where R_o represents the transformation matrix from the perifocal frame to the BCI frame, r_o is the orbit radius and n_0 is the orbital mean motion. The period of the orbit T_o is clearly related to the mean motion through the Kepler third law. Once R_o and r_o are defined, T_o is computed as

$$T_o = \frac{2\pi}{n_o} = 2\pi\sqrt{\frac{\mu}{a^3}} \tag{5.7}$$

where the semi-major axis is $a = r_o$ for a circular orbit. The reference translational velocity in the BCI frame, $v_{ref}(t)$, is obtained by taking the time derivative of the position vector in Eq.(5.6). The numerical values selected for this case are: $R_o = R_y(60)$, $r_o = 55\,km$. The reference attitude consists in the following time-dependent large command

$$\theta_{ref}(t) = \theta_a \left[\sin\left(\frac{2\pi}{T_a}t\right), 0, 0\right]^T \tag{5.8}$$

where $\theta_a = 85$ deg and $T_a = 1$ hr, and its time derivative returns $\omega_{ref}(t)$. The reason for this choice lies in the need of evaluating the navigation algorithms performance when the attitude approaches to large angles. In fact, in any estimation problem the attitude plays a major role in the choice of the attitude parametrization. Each type of parametrization is characterized by some disadvantage. For instance, the kinematic singularity of the Euler Angles, the redundancy and non.uniqueness of the quaternion, the redundancy of rotation matrix or the discontinuity of the modified Rodriguez parameters [111].

As important as the case study, is the selection of the measurement and process noise statistics. The measurement noise represents the uncertainty and imperfection of the sensors and the process noise is considered as a modeling error that is introduced to compensate the model incertitude. The process noise can be assumed to have a standard deviation few orders of magnitude smaller than the measurement noise, when there is a full knowledge of the system model. In this comparison the process noise affects only the UKF whose mathematical model of the plant has been introduced in Section 3.2. The STO does not need it since it is a state observer, and its mathematical model is basically a reproduction of the plant. In order to investigate how the navigation systems perform with noisy measurements, their standard deviations are selected reasonably high. The standard deviations of measurement and process noise are given in Tab. 5.2.

Table 5.2: case study measurement noise standard deviations.

Parameter	Measurement Noise
Attitude [deg]	$\sigma_{\zeta_\theta} = 1$
Position [m]	$\sigma_{\zeta_r} = 50$
Angular Velocity [deg/s]	$\sigma_{\zeta_\omega} = 0.1$
Velocity [m/s]	$\sigma_{\zeta_v} = 10$

The nominal case study is run with a sample frequency of $f_s = 1$ Hz ($\Delta t = 1$ s). Moreover, the navigation algorithm initial condition are chosen with an error of 10 % with respect the true states, for the pose. While an an error of 20 % with respect the true states, for the velocities.

5.3.2 PERFORMANCE ANALYSIS

In order to fairly compare the proposed navigation systems in the next sections, it is necessary to tune their gains such that both UKF and STO performs similarly. It is emphasized that these values are not retrieved with any optimized algorithm, whereas they are found with a trial and error procedure. In order to facilitate this process, the UKF and STO are tuned such that their responses have a good compromise between convergence time and state error statistics. Clearly, since the two navigation system will be placed in the loop with the control systems, it would be advantageous that their convergence time would be as small as possible.

The UKF needs the following matrices to be defined: process noise covariance matrix Q, measurement noise covariance matrix R and the initial estimated state error covariance matrix P_0. These matrices are chosen to represent a reasonable level of expected noise and the accuracy of the initial state error. Since the measurement noise statistics is known, due to the simple sensor model adopted, R is immediately determined. It can be defined according to the variance of the level of measurement noise, hence R is a diagonal matrix whose elements are the square of the values in Tab. 5.2. The process noise covariance matrix Q is significantly more difficult to quantify mathematically. All the uncertainties, disturbances, and unmodelled dynamics are modelled as lumped process noise [65]. In this work no particular method has been used for the tuning, instead a trial and error method is employed, where the Q elements standard deviation are increased from 10^{-5} to 10^2. This procedure showed that having a large Q leads to higher state error statistics; also the navigation algorithm convergence time increases meaningfully. This is due to the fact that, according to Eq.(3.29), if Q is high, then also the *a priori* covariance state error matrix estimate has a large dispersion. In principle, the elements of P_0 matrix may be computed with the knowledge of the initial state uncertainty. However, in order to investigate whether the UKF performs better with an higher initial state covariance, the same procedure of the process noise matrix is applied. Particularly the P_0 elements standard deviation are increased from 10^{-5} to 10^2. This process showed that having really small values of P_0 is not beneficial because the convergence time increases and consequently also the mean and standard deviation of state errors. The combination of values, for Q and P_0 which gave the best performance are shown in Tab. 5.3.

On the other hand, the STO needs a tuning procedure more similar to the one employed with the control systems. As result the values provided in Tab. 5.3 can be found.

The norm of the state errors can help to obtained insights about the navigation algorithm performances, more than the history of each state. Particularly, such errors are depicted in Fig. 5.8. Even if the nature of the two proposed navigation systems is consistently different, the steady state of their estimated states have a similar order of magnitude. It may seem that both the navigation systems are not able to estimate with high accuracy the position. However, it must be emphasized that the level of measurement considered is meaningful. For instance, the position is estimated with an accuracy of $O(10^0)$ m, but the received measurement has a standard deviation of 50 m. On the other hand, it can be seen that the convergence rate is particularly high for the attitude and angular velocity. The position and velocity have a slightly low convergence rate, however they reach a reasonably precision of ≤ 100 m and $\leq 1\, m/s$ respectively, in less than $100\, s$. Fig. 5.8 also shows that the UKF estimates are slightly noisier than the STO estimates. However it can be expected, since the UKF has a stochastic nature, while the STO has a deterministic nature.

The navigation system performances may be described through the statistics of the state errors previously analyzed. They are given in Tab. 5.4. According to [112], the state errors characteristics may be summarized through their mean, standard deviation (std) and normalized root mean square ($RMSE_{\%}$). The mean represents the expected value of the error and has the advantage of being particularly efficient in describing the order of magnitude of the signal; however it has the main disadvantage of being influenced

by outliers. The standard deviation is the square root of variance and it represents the measure of the amount of variation or dispersion of the estimation errors. The RMSE is the variance of the residuals squared and it indicates the degree to which the predicted states are close to the observed data. In this case, the percentage normalized $RMSE_{\%}$ has been used, which is the RMSE normalized with the highest value of the "true" signal. Clearly the estimation improves as these three numerical values decrease [113]. It can be seen that the UKF achieves smaller state means, a part from the angular velocity, in agreement with the previous comments on the order of magnitudes. The high STO position mean and std are achieved because of the initial high values with respect UKF. The fact that the normalized RMSE have a similar order of magnitude, confirm that the two navigation systems are able to achieve a comparable precision, even if the characteristics of the UKF transient are more favorable.

The performance of the UKF does not reflect only in the accuracy of the estimation error, but also in the accuracy of the estimated state error covariance matrix P. The diagonal elements of this matrix should resemble the variance of the Gaussian distribution resulting from the estimated state errors. Therefore, the square of the diagonal elements of P represents the confidence bound in which the 84.13% of samples should be placed. Fig. 5.9 shows the UKF estimation error and the relative estimated standard deviation. The good performance of the UKF is confirmed by the fact that the estimation errors are unbiased, i.e. have zero mean and are contained in the estimated bounds [114]. Moreover, the results show that the state errors are well bounded inside the covariance bounds, meaning a good modelling of the stochastic system. It must be emphasized that in practical situations the true states may be not known. In these cases the same procedure is applied to the residual r and the measurement covariance matrix P_{zz}. Or another technique consists in showing that the power spectral density (PSD) of the estimated measurements assumes smaller values than the PSD of the true measurements.

Table 5.3: UKF case study measurement and process noise standard deviations (left); parameters of the navigation system based on STO algorithm (right)

Parameter	Process Noise	Initial Error
θ[deg]	$\sigma_{\zeta_\theta} = 10^{-5} \cdot \frac{180}{\pi}$	$\sigma_{\theta_0} = 1 \frac{\pi}{180}$
r[m]	$\sigma_{\zeta_r} = 10^{-5} \cdot 10^3$	$\sigma_{r_0} = 1 \cdot 10^3$
ω[deg/s]	$\sigma_{\zeta_\omega} = 10^{-5} \cdot \frac{180}{\pi}$	$\sigma_{\omega_0} = 1 \frac{\pi}{180}$
v[m/s]	$\sigma_{\zeta_v} = 10^{-5} \cdot 10^3$	$\sigma_{v_0} = 1 \cdot 10^3$

Parameter	Value
G_1 [s,s/m]	10^{-5}
G_2 [-,m^{-1}]	10^{-1}
B_1 [-]	1
B_2 [-]	$6 \cdot 10^{-2}$
B_{31} [1/s]	10^{-3}
B_{32} [m/s]	10^{-4}

Table 5.4: Performance of UKF and STO algorithms: state errors mean, standard deviation and normalized root mean square.

Algorithm	Parameter	mean	std	$RMSE_{\%}$
UKF	θ [deg]	1.2453	9.2446	4.4956
	r [m]	5.3286	11.6662	0.0213
	ω [deg/s]	0.0714	0.5288	7.4190
	v [m/s]	0.1780	0.3700	3.5154
STO	θ [deg]	0.7872	5.8489	2.8327
	r [m]	84.1557	508.4562	0.8547
	ω [deg/s]	0.0526	0.4966	7.0157
	v [m/s]	0.4834	0.9686	8.2455

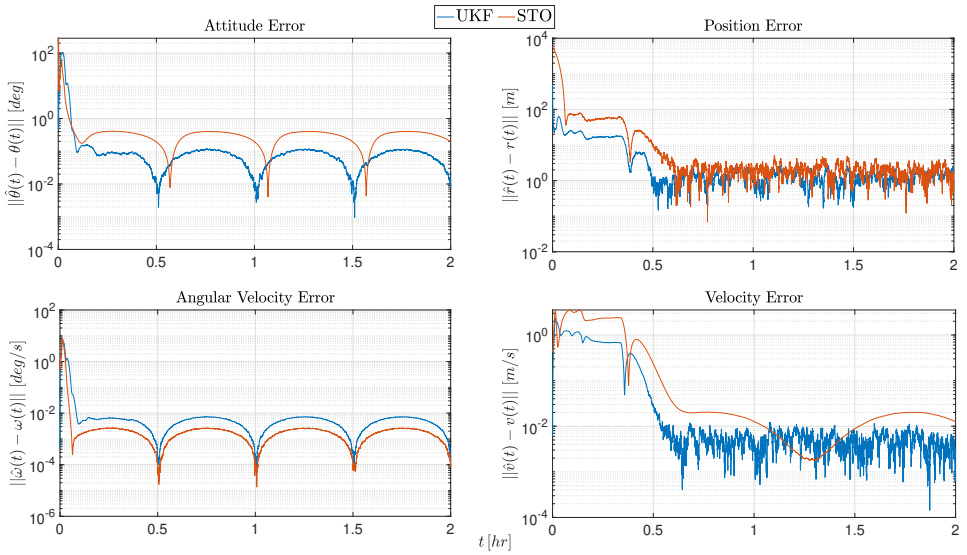

Figure 5.8: Norm of the difference between the reference states and the estimated states, obtained in open loop with the proposed navigation systems.

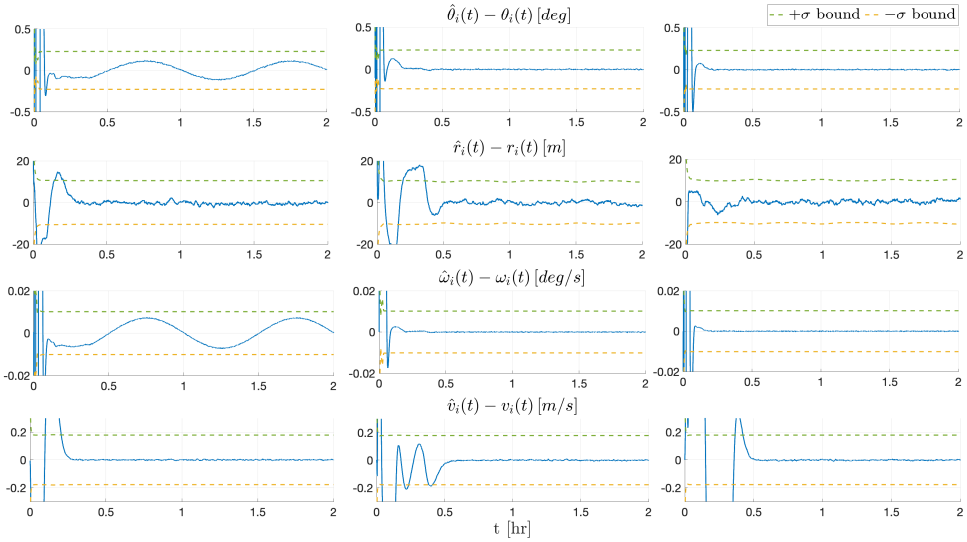

Figure 5.9: State estimation errors and estimated covariance state errors obtained with UKF, with respect to the time.

5.3.3 CASE 1: SENSITIVITY TO MEASUREMENT NOISE

In this section, the performance of the two proposed navigation systems is analyzed with respect the accuracy of the provided measurements. The two sets of noise standard deviations shown in Tab. 5.5 are used. The first sets represents a navigation system employed with very accurate and precise sensors thus explaining the low measurement noise standard deviation of each state. The second set, instead, represents a navigation system employed with very noisy sensors. The case study considered in the first place had standard deviations in between these new two sets.

Table 5.5: Case study measurement noise standard deviations.

Parameter	Measurement Noise (low)	Measurement Noise (high)
Attitude $[deg]$	$\sigma_{\zeta_\theta} = 0.1$	$\sigma_{\zeta_\theta} = 10$
Position $[m]$	$\sigma_{\zeta_r} = 1$	$\sigma_{\zeta_r} = 500$
Angular Velocity $[deg/s]$	$\sigma_{\zeta_\omega} = 0.001$	$\sigma_{\zeta_\omega} = 1$
Velocity $[m/s]$	$\sigma_{\zeta_v} = 1$	$\sigma_{\zeta_v} = 1000$

The norm of the state errors are shown in Fig. 5.10 for the two proposed sets for both UKF and STO. When the measurements are not corrupted, the UKF is able to provide estimates with an incredibly high accuracy and convergence rate. On the other hand when the measurement are noisy, the transient response behaves worse, having an initial overshoot and an unacceptable high convergence time. For noisy measurements, the STO is more robust in the transient response even if the velocity and position errors have higher order of magnitude with respect UKF. When the measurements are not corrupted, the STO is not able to provide estimates with the same accuracy of UKF, instead.

The measurement covariance matrix R changes according to the standard deviation of the noise for each state. In the UKF algorithm, this matrix influences the *a posteriori* estimation of the state error covariance matrix P. For this reason, it is interesting to analyze how the estimation of P changes with respect the one given in Fig. 5.9. The results are shown in Fig. 5.11- 5.12. When the first set of Tab. 5.5 is used the σ bounds assumes small values in agreement with the order of magnitude of the relative state error. The same rational applied when very noisy measurements are used. It is interesting to note that for accurate measurements the σ bounds have less oscillation in the transient phase, due to the fact that the estimated states converge with high rate. In addition, the same sinusoidal shape found in the state error norms, can be seen. For noisy measurements, the σ bounds are more irregular in the transient phase and then they evolve constantly.

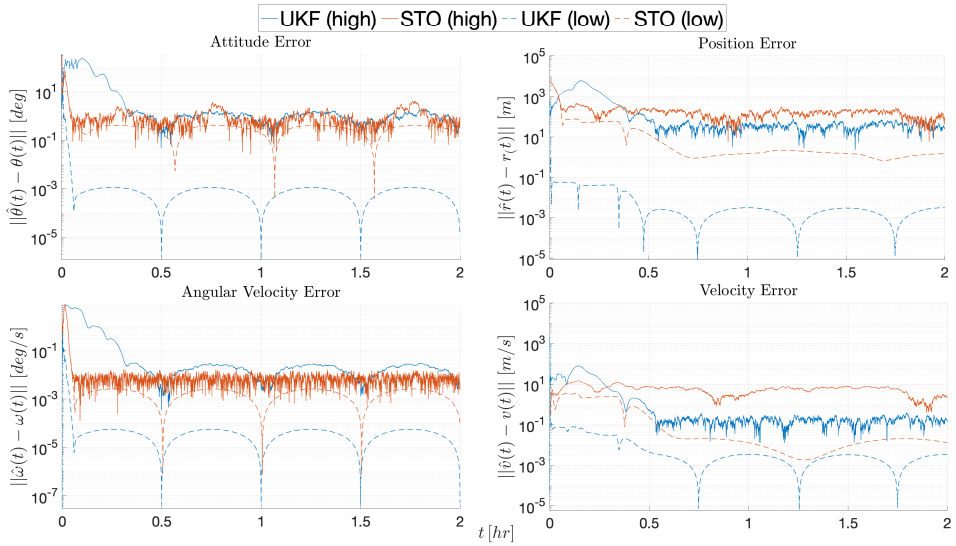

Figure 5.10: Norm of the difference between the reference states and the estimated states, obtained in open loop with the proposed navigation systems. Results shown for "low" and "high" measurement noise statistics.

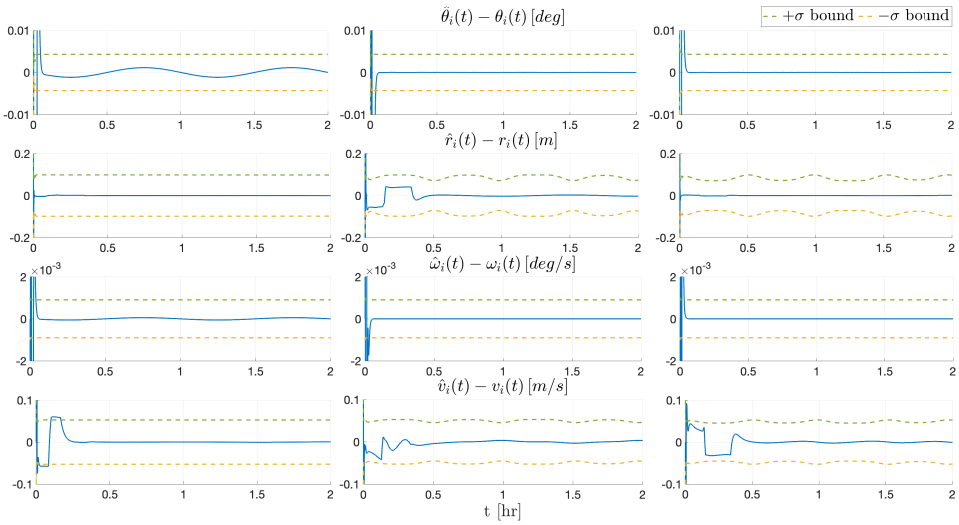

Figure 5.11: State estimation errors and estimated covariance state errors obtained with UKF, with respect to the time. Results obtained with "low" measurement noise statistics.

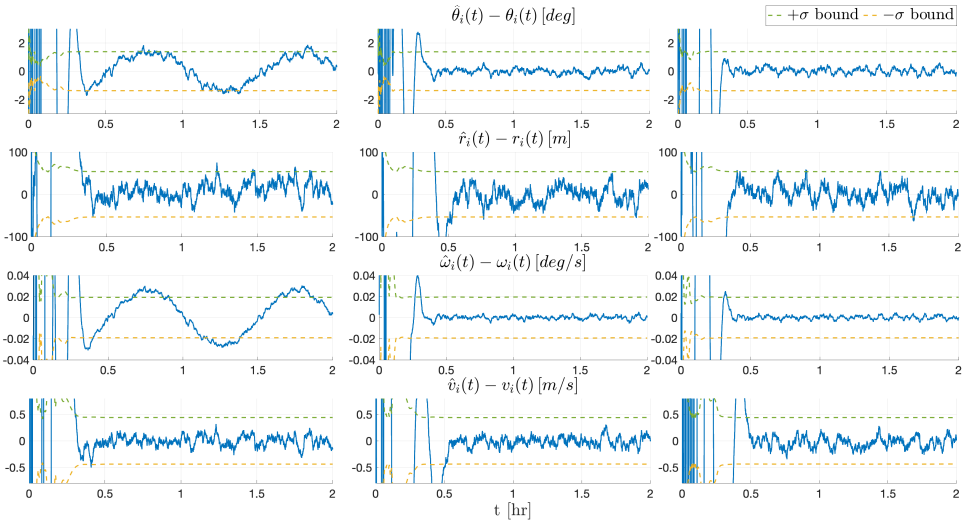

Figure 5.12: State estimation errors and estimated covariance state errors obtained with UKF, with respect to the time. Results obtained with "high" measurement noise statistics.

5.3.4 CASE 2: SAMPLING FREQUENCY

The proposed navigation systems are now tested with different sampling frequencies, which are selected to be in the same range of the ones used in the control system comparison. Particularly, starting from $10\,Hz(\Delta t = 0.1)$ it is decreased up to $0.09\,Hz(\Delta t = 11\,s)$. In Fig. 5.13 the results are shown in terms of the statistics of the norm of the estimation errors. For high f_s (small Δt), the UKF outperforms the STO, and the slope of the curves show there is still margins of improvement for smaller time steps. The STO, instead, does not seem to perform significantly better, hence an additional decreasing of Δt would be meaningless. In the middle zone of f_s, the two proposed navigation systems perform similarly and for small f_s (high Δt), the STO generally performs better. Even if the UKF achieves better results for small Δt, the the STO seems to be definitely more robust to the change in sampling frequency.

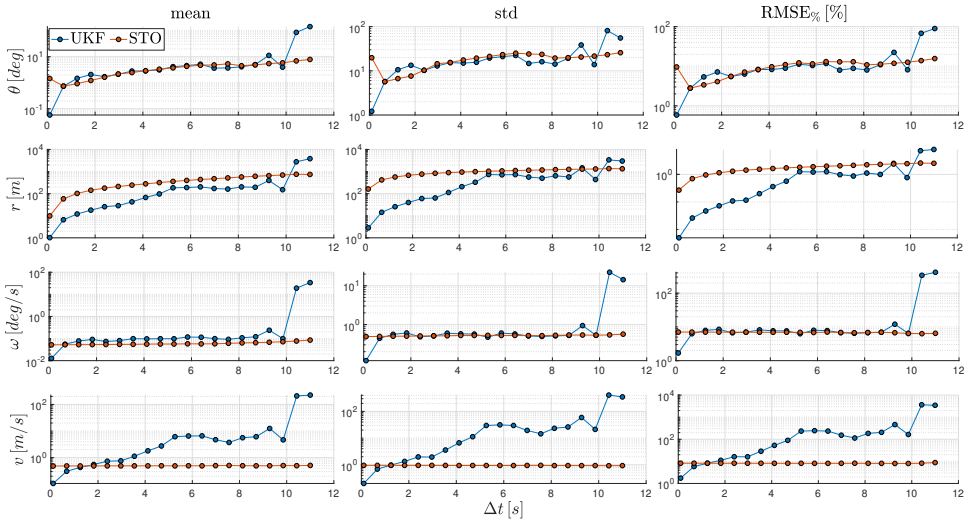

Figure 5.13: State error statistics (mean, std and normalized RMSE) with respect the time step Δt, which is the inverse of the sampling frequency f_s.

5.3.5 CASE 3: INACCURATE INITIAL CONDITIONS

The proposed navigation algorithms need to be initialized with an initial condition or guess for the estimated states. The value used to initiate the estimation algorithm plays an important role from the perspective of the navigation system performance. For instance, algorithms such as the EKF, which uses a linearization technique, may also diverge if the state initial is not chosen correctly.

In this section, the behaviour of UKF and STO is analyzed with respect to the uncertainty on the initial estimate, given on all the states at the same time. The STO algorithm just need the initial guess $\hat{x}_0 = (g_0, \mathbb{V}_0)$. Unlike the observer, the Kalman Filter also need the

initialization of the state error covariance matrix $P_0 = E(\hat{x}_0 - x_0)(\hat{x}_0 - x_0)^T$. Clearly, when the difference between the real state and the estimated one increases, so does the error covariance. For this reason, it is interesting to evaluate the performance of the UKF even in the case the initial estimate of P is tuned accordingly to the degree of uncertainty on the initial estimated state X_0. Therefore, the additional label "UKF(1)" is used for the UKF which has a varying P_0. Instead UKF has the constant P_0, which has been defined previously.

Let the nominal initial states be $R(\theta_0), 1, r_0, 1, \omega_0$ and v_0, the navigation algorithms initial estimates are parametrized as

$$\begin{aligned} \hat{g}_0 &= \begin{bmatrix} R\left(\left(\theta_0(1+\gamma/100)\right)\right) & r_0\left(1+\gamma/100\right) \\ 0 & 1 \end{bmatrix} \\ \hat{\mathbb{V}}_o &= \begin{bmatrix} \omega_0\left(1+\gamma/100\right), & v_0\left(1+\gamma/100\right) \end{bmatrix} \end{aligned} \tag{5.9}$$

where γ represents the percentage uncertainty, which varies from -200% to 200% for each state at the same time. The UKF(1) adapts the initial state error covariance matrix elements using the order of magnitude of the difference between the guess and the true state. The results are shown in terms of the statistics of the norm of the estimation errors, in Fig. 5.14. It can be seen that STO is robust in keeping a good performance for the velocity estimation, and it performs similarly to the UKF for the attitude estimation. On the other hand, the position and angular velocity assume too high statistics for large values of γ. The UKF performs better than STO, even if when $\gamma \geq 50\%$ the velocity estimation gets worse. It can be seen that generally the UKF(1) performs similarly to UKF for moderate values of γ, but when the uncertainty increases, UKF(1) performs better.

Figure 5.14: State error statistics (mean, std and normalized RMSE), with respect the initial state estimate uncertainty γ.

5.4 CONTROL SYSTEMS COMPARISON

In the analysis and design of any control system, many issues have to be considered [115]. The emphasis is typically given to the following specifications:

- Stability of the Closed-Loop System
- The response to command signals (tracking)
- The robustness to model uncertainties
- The input disturbance rejection
- The noise measurement injection

In this section, a case study scenario is introduced and the proposed control systems are tuned such that the closed-loop response satisfies some performance indexes. Subsequently, their performance are tested in different test cases, according to the above points. However the noise measurement injection is not considered, since the noisy measurement will be handled by the navigation system, in the final complete GNC design. In addition, the robustness to change in sample frequency is accounted.

5.4.1 NOMINAL CASE STUDY

In order to do so, a nominal case study is selected. The scenario consists in the same one used in Section 5.3.1. With respect to that one, two differences are introduced. The first one is the simulation time which is extended for a time of T_o. The second change reflects in a different choice for the commanded attitude, which consists in the series of 2 doublets with large commanded attitude

$$\Theta_{ref}(t) = \begin{cases} [0,0,0]^T \text{ deg} & \text{if} t \leq \Delta t_m \\ [80,80,80]^T \text{ deg} & \text{if} t \geq \Delta t_m, t \leq 2\Delta t_m \\ -[80,80,80]^T \text{ deg} & \text{if} t \geq 2\Delta t_m, t \leq 3\Delta t_m \\ [30,30,30]^T \text{ deg} & \text{if} t \geq 3\Delta t_m, t \leq 4\Delta t_m \end{cases} \tag{5.10}$$

with $\Delta t_m = T_o/4$ s. The reference angular velocity is kept $\omega_{ref} = [0,0,0]^T$ deg/s for all the simulation time. Finally the spacecraft is assumed to have the initial position and velocity with a 10% of error with respect to the reference, it has an initial attitude of $\Theta_0 = [30,60,70]^T$ deg and it is tumbling with $\omega_0 = [5,2,3]^T$ deg/s.

The integration is performed with the LGVI introduced in Chapter 2 for a time of T_o, using a sample frequency of $f_s = 1$ Hz, i.e. a time step of $\Delta t = 1$ s.

5.4.2 PERFORMANCE ANALYSIS

In order to fairly compare the proposed control systems in the next sections, it is necessary to tune their gains such that both MLBS and SMC behave similarly. It is emphasized that these values are not retrieved with any optimized algorithm, whereas they are found with a trial and error procedure. For this reason, in this preliminary section, the

proposed control systems are tested through numerical simulations. This procedure is also particularly useful to gather information of the closed-loop system behavior with respect the gain values and the saturation limits. The control systems are tuned on the basis of the following criteria:

- The position steady state error has to be $\|r_{ss}(t)\| \leq 10$ m
- The settling time to reach the condition $\|r(t) - r_{ref}(t)\| \leq 1000$ m has to be less than 1000 s, after a command
- The attitude steady state error has to be $\|\Theta_{ss}(t)\| \leq 0.5$ deg
- The settling time to reach the conditions: $\|\Theta(t) - \Theta_{ref}(t)\| \leq 1$ deg has to be less than 200 s after a command
- The control force saturation limit has to be ≤ 50 N per axis
- The control moment saturation limit has to be ≤ 1 Nm per axis

As result of this tuning procedure, the parameters in Tab. 5.6- 5.7 are obtained for the MLBS -and SMC-based control system respectively. It can be seen that the MLBS is able to satisfy the aforementioned constraints with smaller saturation limits. Particularly the SMC controller needs around three times the saturation limits of MLBS. In addition, during this preliminary phase, the MLBS has proved to guarantee the closed-loop convergence even with extremely small saturation limits ($F_{c,i} = 5$ N, $M_{c,i} = 0.01$ Nm) at the cost of having a slower convergence. In fact when the maximum available control torque and force are low, the controller gains are also low, and this leads to an undesirable slow convergence rate [116]. On the other hand, the SMC is more sensible to the saturation limits changing, and with very small allowable control input can experience more issues in order to guarantee the convergence. The discontinuous control action may also make the closed-loop system never converge.

The responses of the closed-loop systems are not shown since they don't allow to gather useful information on the behavior of the systems. Instead, in Fig. 5.15 the norm of the difference between the reference states and the spacecraft states for the two proposed control algorithm are shown. Both the algorithms are able to handle the two condition given on the settling times. The steady state error conditions are more critical, since large attitude commands are required. In fact, when the spacecraft performs an attitude maneuver, this affect also the position and the velocity since there is the coupling between the two dynamics. For this reason in correspondence of each quarter of period there is a peak. It can be seen that the MLBS algorithm is able to lead the spacecraft to exceptionally small steady state errors, even smaller than the required ones. The SMC algorithm has more difficulties to keep the above performance indexes for the attitude, especially in the third quarter of period. It is the most critical, since it is required an attitude command of 160 deg for each axis. In this period of time also the position is strongly affected, even if the condition of being under 10 m is satisfied.

In Fig. 5.16 the norm of the control force and moment are reported for the two control algorithms. It can be seen that the control moments are comparable in the first two

quarters. However when large attitude maneuvers are required, the SMC needs a larger torque. The control forces are comparable during the attitude maneuver, even if the SMC controller requires a slightly longer convergence to the steady state. At the beginning the SMC algorithm requires a significantly larger amount of thrust to bring the spacecraft to the orbit. It must be noted that the control force at regime are small but nonzero, since a control force is needed to keep the spacecraft moving along the closed orbit, because it is not a natural trajectory of the system [117].

The control system performances may be described by the performance indexes reported in Tab. 5.8. Where ΔV is the integrated control acceleration, $\Delta V = \int_0^t \|a_c(\tau)\| d\tau$ and $\Delta\tau$ is the integrated control torque $\Delta\tau = \int_0^t \|M_c\tau\| d\tau$. Then $\|a_{cm}\|$ and $\|\tau_{cm}\|$ are the peak control acceleration and control moment respectively, ΔM_p is the burnt propellant mass. The numerical values reported here confirm the previous analysis conducted through Fig. 5.15 - 5.16, the MLBS behaves better. The results obtained with the SMC are consistent with the ones obtained in [117], where a super twisting control (STW) has been implemented for a "decoupled" orbit control case.

Table 5.6: Parameters of the control system based on MLBS algorithm.

Parameter	Values
Control Force Saturation per axis $[N]$	$F_{c,i} = 20$
Control Moment Saturation per axis $[Nm]$	$M_{c,i} = 0.3$
$\kappa\,[km\,s^{-2}]$	10^{-6}
$k_{11}\,[s^{-1}]$	0.05
$k_{12}\,[s^{-1}]$	0.01
$k_{21}\,[s^{-1}]$	0.05
$k_{22}\,[s^{-1}]$	0.01
$k_{31}\,[s^{-2}]$	0
$k_{32}\,[s^{-2}]$	10^{-9}
$a\,[-]$	$\begin{bmatrix}1.2 & 1.1 & 1\end{bmatrix}^T$

Table 5.7: Parameters of the control system based on SMC algorithm.

Parameter	Values
Control Force Saturation per axis $[N]$	$F_{c,i} = 50$
Control Moment Saturation per axis $[Nm]$	$M_{c,i} = 1$
$K_{\sigma,M}\,[kNm]$	1
$K_{\sigma,F}\,[kN]$	50
$k_{11}\,[s^{-1}]$	0.05
$k_{12}\,[s^{-1}]$	0.01
$c_{11}\,[s]$	$5\cdot10^{-9}$
$c_{12}\,[s\,km^{-1}]$	0.05
$c_{21}\,[-]$	$5\cdot10^{-9}$
$c_{22}\,[km^{-1}]$	0.0005
$c_{31}\,[-]$	10^{-12}
$c_{32}\,[km^{-1}]$	0
$k_{11}\,[s^{-1}]$	0.05
$k_{12}\,[s^{-1}]$	0.01
$a\,[-]$	$\begin{bmatrix}1.2 & 1.1 & 1\end{bmatrix}^T$

Table 5.8: Performance of MLBS and SMC laws: ΔV, $\Delta\tau$, control input peaks and propellant mass burnt.

Control Low	$\Delta V\,[km/s]$	$\|a_{cm}\|[km/s]$	$\Delta\tau\,[Nms]$	$\|\tau_{cm}\|[Nm]$	$\Delta M_p\,[kg]$
MLBS	0.0691	$4.0754\cdot10^{-5}$	89.0771	0.4243	25.2909
SMC	0.0915	$1.0189\cdot10^{-4}$	151.4317	1.6225	36.5747

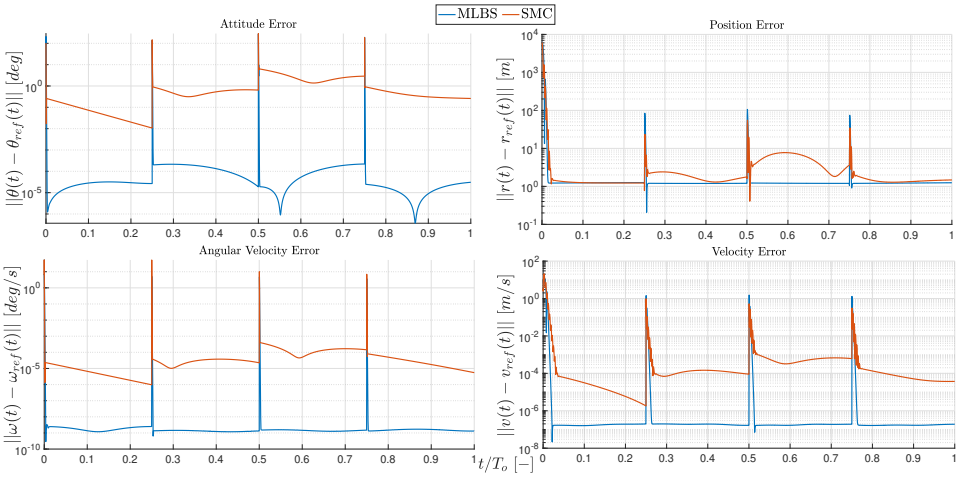

Figure 5.15: Norm of the difference between the reference states and the spacecraft states, obtained closing the loop with the proposed control systems.

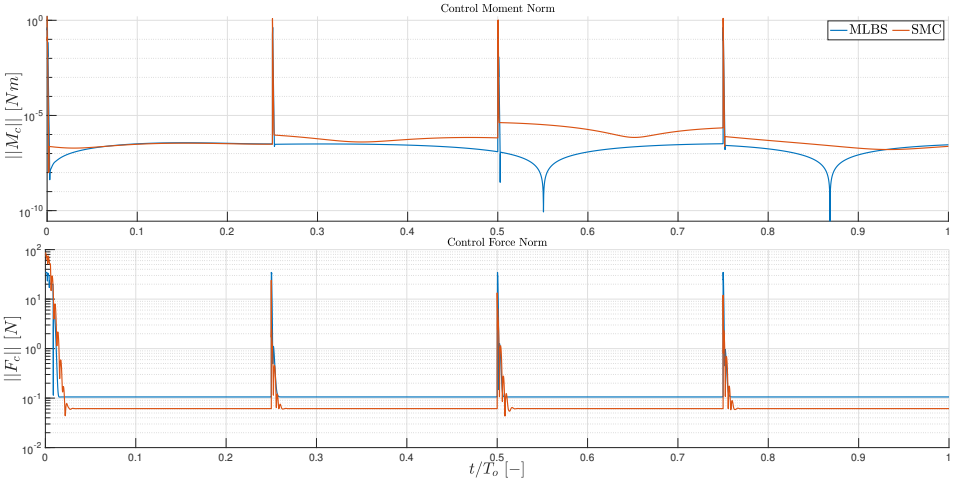

Figure 5.16: Norm of the control force and moment for the two proposed control systems.

5.4.3 CASE 1: SENSITIVITY TO PARAMETER UNCERTAINTY

The results obtained in the previous section highlight that the MLBS behaves better than the SMC algorithm. However it must be emphasized that the SMC law (Eq.(4.35)) is def-

initely easier than the MLBS one (Eq.(4.6)), and has the important advantage of being completely independent by the mathematical model of the plant. In addition, also the plant parameters, such as the spacecraft mass or inertia tensor, don't even appear. It is not the case of the MLBS law, which is influenced by the knowledge of the parameter J and m. In this section the behavior of the MLBS control system is analyzed along with the uncertainty on these two plant parameters. Particularly, let the nominal values be m_0 and J_0, the MLBS known values are parametrized as

$$m = m_0(1+\gamma_m/100) \quad J = J_0(1+\gamma_J/100) \tag{5.11}$$

where γ_m, γ_J are the percentage error, which varies from -90% to 150%.

In Fig. 5.17 the results of this first case are shown in terms of ΔV and $\Delta\tau$ for the MLBS-based control system. The mass uncertainty influences meaningfully only the required control force which is used to control the translational dynamics variables: position and velocity. The MLBS control law is linearly dependent from the value of the mass known by the control system. For this reason, with equal state error, the acceleration produced with a large mass will be greater than the acceleration produced with a lower mass. Decreasing the known mass, the total ΔV decreases, but on the other hand the position and velocity responses are badly influenced. The convergence rate becomes undesirable long, and the steady state error increases. However, they still remain bounded as the values obtained in Fig. 5.15. Looking at Eq.(4.2), it can be seen that ΔV varies as M_p, i.e. in order to have a large ΔV, more propellant mass is required. In this case, the mass consumption also remains bounded between 20 kg for the minimum mass uncertainty and 30 kg for the maximum one.

The inertia uncertainty, instead has a large impact on both the rotational and translational dynamics. The reason lies in the coupling of the velocity derivative with the angular velocity, Eq.(2.10). The response of the rotational dynamics is comparable to the response of a second order system where the inertia acts as damper. The response varies from being overdamped to critically damped and finally to underdamped along with the inertia variation from -90% to 150%. The control system has to provide a large $\Delta\tau$ in the critically damped situation, since the response converges in a short amount of time. The other two regions are characterized by lower values of $\Delta\tau$. The velocity response is also influenced by the inertia tensor uncertainty. Particularly the highest ΔV happens when the attitude response is most sluggish. When the inertia increases the ΔV decreases, but near the highest values of J, the ΔV tends to increase again. This behavior depends on the velocity response which becomes to have an higher peak. Although the state errors tend to increase with a decreasing inertia, they still remain bounded thus assuming small values as the ones in Fig. 5.15. In this case the mass consumption remains under 30 kg, except for $\gamma_J = -90\%$ where it increases to 40 kg.

5.4.4 CASE 2: SAMPLING FREQUENCY

The selection of sampling frequency is an important issue in control system design. In principle, having low sampling rates is beneficial from the economical perspective. In fact, low f_s mean high Δt, and then there is more time available for control algorithm

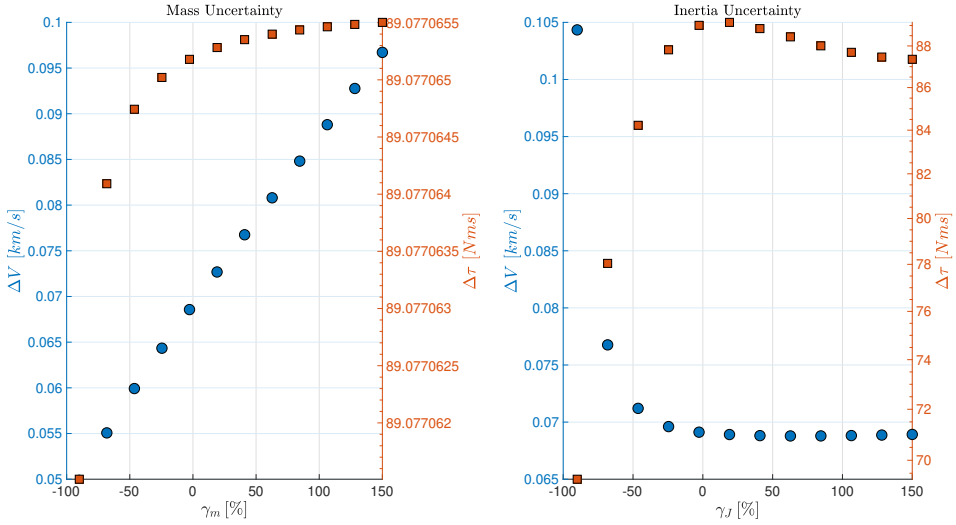

Figure 5.17: Norm of the control force and moment for the MLBS proposed control system with respect to parameters uncertainty γ_m and γ_J. SMC control system does not appear since it is insensitive to change in γ_m and γ_J.

execution, which can thereby be implemented on a slower (and cheap) computer. However the digitization of a well behaved analog control systems can heavily affect system response. If the sampling frequencies becomes too small the closed-loop system may even become unstable, since the control system is not able to follow the error dynamics. In fact, f_s should at least be twice as high as the bandwidth of the error signal in agreement with the Nyquist criterion [118].

The proposed control systems are now tested with different sampling frequencies. Starting from 20 Hz ($\Delta t = 0.05$ s), it is decreased up to closed-loop divergence. This procedure is particularly useful for two reasons: 1) It allows to test the robustness of the control law with the sampling rate changing; 2) It allows to understand how the control law performs with the nominal rate of 1 Hz ($\Delta t = 1$ s).

In Fig. 5.18 the results are shown in terms of ΔV and $\Delta\tau$ for both the control systems. It can be seen a similar behavior for all the four curves: with low f_s (high Δt) the curves tend to increase exponentially, while with high f_s (low Δt) the curves tend to a plateau. It is important to underline that the MLBS law is able to guarantee the system convergence up to $f_s = 0.0870$ Hz ($\Delta t = 11.5$ s), while the SMC law up to $f_s = 0.8696$ Hz ($\Delta t = 1.15$ s). Moreover, the MLBS has not significant changes in terms of control effort reducing the time step more than 1 s. On the other hand, for the SMC, the frequency reduction is beneficial for the force control effort, which seems to converge to values comparable to the ones of MLBS. However, in this work a sampling rate of $f_s = 1$ Hz ($\Delta t = 1$ s) is used, due to the fact that the integration periods are large. Selecting a too small time step would increase tremendously the computational cost.

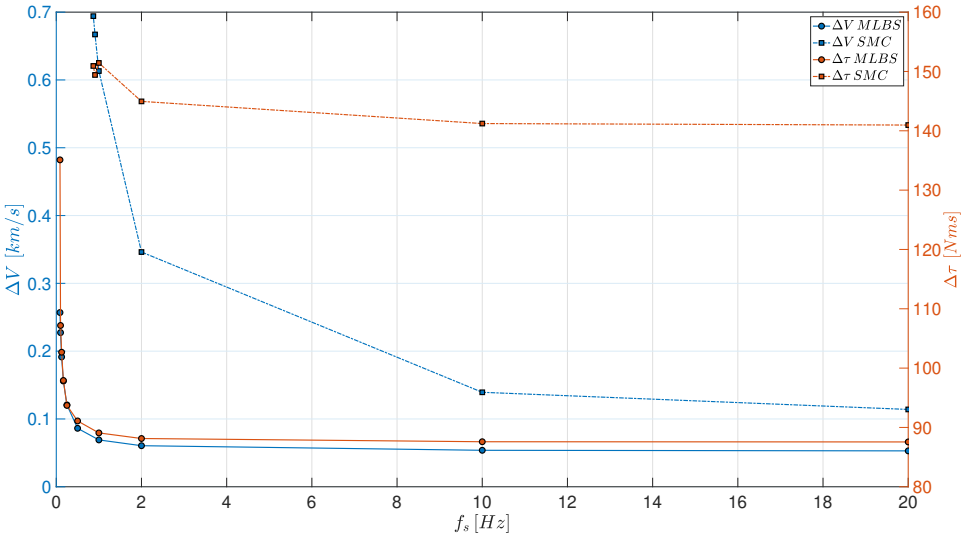

Figure 5.18: ΔV and $\Delta\tau$ for the two proposed control systems with respect the sampling frequency f_s.

For the MLBS algorithm, the attitude and angular velocity state errors are not meaningfully influenced by the change of sampling frequency. The position and velocity state errors behave approximately polynomial in f_s. With $\Delta t = 11.5$ s a position accuracy of 14 m and a velocity accuracy of 10^{-4} m/s are guaranteed. With $\Delta t = 0.05$ s, instead, the position accuracy of $\leq 0.1\,m$ and the velocity accuracy of $\leq 10^{-8}$ m/s are obtained, at the expense of a propellant mass consumption of 23 kg. For the SMC algorithm, only the position state error is heavily influenced by the sampling frequency. With the highest f_s an accuracy of ≤ 1 m is obtained, at the expense of a propellant mass consumption of 50 kg.

5.4.5 CASE 3: INPUT NOISE DISTURBANCE

In this last section, the robustness of the two proposed control system is tested when additional input noisy force and torque are fed into the system. It is not an unrealistic assumption when a spacecraft application is considered. As matter of fact, in the space there are several sources of disturbance. For instance, for a low-Earth orbit (LEO) there are:

- Gravity gradient $o(10^{-5})$ Nm
- Solar radiation pressure $o(10^{-6})$ Nm
- Earth magnetic field (10^{-5}) Nm
- Air drag $o(10^{-7})$ Nm

- Internal disturbances, as: uncertainty in centre of gravity, thrusters misalignment, rotating machinery, liquid sloshing, dynamics of flexible bodies, thermal shocks [63]

Other effects which are relatively small with respect to the above ones, are originated by Earth Albedo effect, the solar wind or the gravitational field of other near bodies [119].

In this context none of the above disturbance is modeled in detail, since the objective is to test the robustness of the control systems to the input noise disturbance $u_d = [M_d, F_d]$. For this reason the disturbance force and moment components are modeled as a zero mean Gaussian white noise with increasing order of magnitude variance

$$F_{d,i} \sim \mathcal{N}(0, \sigma^2_{F,d}) \tag{5.12}$$

$$M_{d,i} \sim \mathcal{N}(0, \sigma^2_{M,d}) \tag{5.13}$$

where the moment standard deviations $\sigma_{M,d}$ varies from 0 Nm to 0.0500 Nm, and the force standard deviations $\sigma_{F,d}$ varies from 0 N to 200 N. The upper limits are chosen as the highest values of noise variance for which both MLBS and SMC can guarantee the closed-loop stability. Moreover the force and moment input disturbances are studied separately, such the the weight of the single effect can be analyzed. Clearly the combination of the two, can only results in a worse performance.

In Fig. 5.19 the results are shown in terms of ΔV and $\Delta\tau$ for both the control systems. The third dimension in the color bar is represented by the dimensionless time in which the total amount of propellant is burnt and the spacecraft diverges from the tracking orbit. The first plot represents the control effort variation with respect the force standard deviations $\sigma_{F,d}$. The force disturbance does not affect meaningfully the control torque, hence it is not reported. In agreement to the previous cases, the SMC tends to require a greater amount of ΔV than the MLBS control system. It can be seen that the SMC consumes all the propellant mass already with $\sigma_{F,d} = 40\,N$ after about $0.7T_o$. The MLBS starts to use up all the propellant around $\sigma_{F,d} = 100$ N after about $0.9T_o$. In the worst scenario of $\sigma_{F,d} = 200$ N the SMC uses all the propellant in less than $0.3T_o$, while MLBS is able to use it up to $0.55T_o$. In Fig. 5.20 the state error norms are shown for the first part of the mission for different noise variances. It can be seen that the attitude and angular velocity errors are completely insensitive for SMC, while for MLBS they become to be slightly noisy. The position and velocity errors, instead, remain bounded and acceptable also for the largest disturbance force for SMC. While MLBS is not able to handle large source of noise, and even with the small $\sigma_{F,d} = 1$ N, performs worse than SMC.

The two bottom plots represents the control effort variation with respect the moment standard deviations $\sigma_{M,d}$. In this case, the impact on both the control force and moment is heavy. It is interesting to note that the MLBS struggles a lot to control the position and velocity when a disturbance noise is considered. The total amount of propellant is already used around $\sigma_{M,d} = 0.015$ Nm after about $0.7T_o$. The SMC, instead starts to burn all the propellant around $\sigma_{M,d} = 0.04$ Nm after about $0.9T_o$. It is also interesting to see that the MLBS ΔV consumption increases a lot faster than the SMC, while the noise variance increases. As matter of fact, around $\sigma_{M,d} = 0.01$ Nm, the SMC needs the half of thrust than the MLBS. On the other hand, the slope of $\Delta\tau$ is significantly greater for SMC than MLBS. However it must be noted that the MLBS curve is far under the SMC one

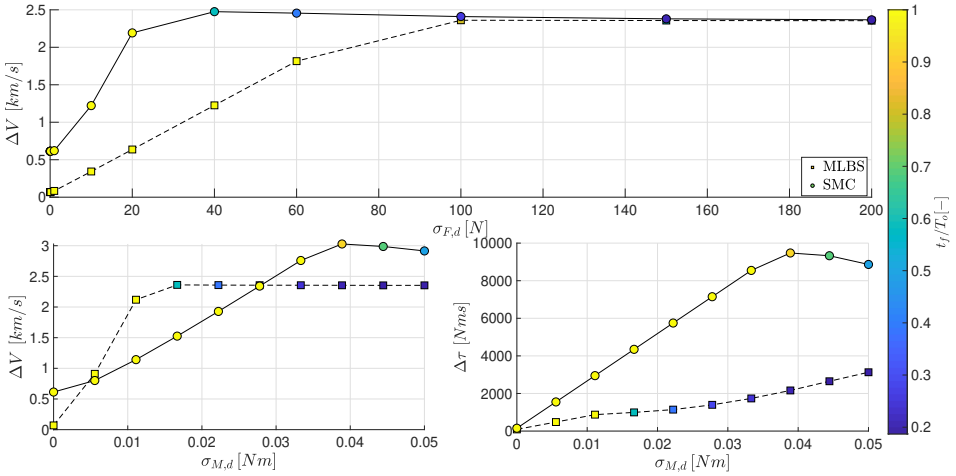

Figure 5.19: Norm of the control force and moment for the two proposed control systems with respect the standard deviation of input noise force and moment, $\sigma_{F,d}$ $\sigma_{M,d}$ respectively. t_f represents the time in which the simulation stops, because the control system has used all the amount of propellant.

because when the propellant mass is over, the simulation ends. Therefore, for MLBS, the values for $\sigma_{M,d} > 0.01$ Nm are not representative of the real amount of control torque used up to T_o. In Fig. 5.21 the state error norms are shown for the first part of the mission for different noise variances. Even in this case, the results highlight how the SMC is significantly more robust to input noise. This robustness translates in a better use of the control force and moment, and clearly of the propellant mass for the thrusters.

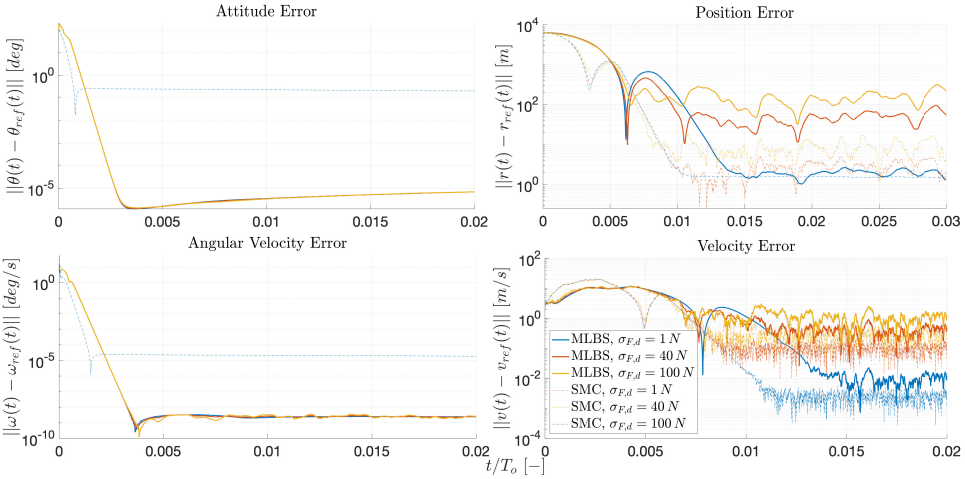

Figure 5.20: State error norms for the closed-loop responses obtained with the two proposed control systems, for different standard deviation of the input noise disturbance force $\sigma_{F,d}$.

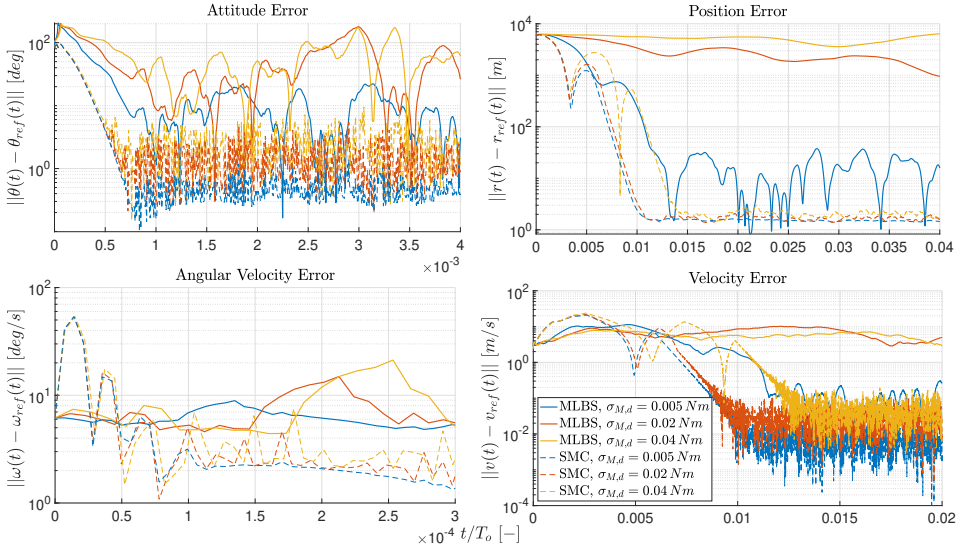

Figure 5.21: State error norms for the closed-loop responses obtained with the two proposed control systems, for different standard deviation of the input noise disturbance moment $\sigma_{M,d}$.

5.5 NAVIGATION AND CONTROL SYSTEM COMBINATIONS COMPARISON

In Section 5.4, two different control an systems have been proposed. Then, they have been stressed in a variety of cases, where the orbit-attitude coupling were involved. The first one, based on the Morse-Lyapunov control via Backstepping on $\mathsf{TSE}(3)$, is dependent on the spacecraft parameters and has proved to control the spacecraft with a relatively low control effort. The second one, based on the sliding mode control on $\mathsf{TSE}(3)$, has the advantage of being completely independent on the spacecraft plant and the effect of the unmodeled dynamics led to a control effort generally higher than the MLBS. However, it showed a more robust behaviour under uncertainties/disturbances.

The control systems comparison highlighted the introduction of noise in the closed-loop system as the most critical test case. Although the SMC showed to be robust to noise, its introduction led to a considerable waste of moment and force control. However, control systems generally have to perform under uncertainties/disturbances and with measurement signals corrupted by noise. As result, when sensors provide noisy measurements, a filtration/estimation approach is needed [41].

In this respect, Chapter 3 proposed two different navigation systems, with the objective of providing state estimates. The estimation process refers to the computation of an approximation of the (state) variables such that their values are usable for some other purpose. Even if the inputs of the algorithm are incomplete, uncertain or corrupted [30]. Clearly, in the GNC context, the purpose is to fed the control system with the estimated variables. It is important to emphasize that the two proposed systems employ very different state estimators. The STO is a deterministic state observer, meaning that the prediction of the state does not involve any source of randomness. In fact, the observer is structured as a copy of the plant and its gains remain constant through out the process, once they are selected. On the other hand, the UKF is a stochastic state filter, meaning that the prediction of the state possess some inherent randomness. Particularly, the UKF is a an algorithm which uses external measurements, containing noise, and computes estimates of the unknown variables that are more accurate than those based just on the measurements, by estimating a joint probability distribution over the variables for each instant of time. Thus, unlike the STO, the UKF gains are continuously changed by the algorithm itself [43].

In this final chapter, the proposed navigation and control systems are combined which each other as showed in Fig. 1.2, resulting in a total of four combinations:

- Unscented Kalman filter and Morse-Lyapunov control via Backstepping (UKF-MLBS)
- Unscented Kalman filter and sliding mode control (UKF-SMC)
- Super-twisting observer and Morse-Lyapunov control via Backstepping (STO-MLBS)
- Super-twisting observer and sliding mode control (STO-SMC)

The same rationale applied in the previous chapter is pursued. Once a case study scenario is introduced, the proposed navigation and control system combinations are tuned such that the closed-loop response satisfies some performance indexes. Subsequently, their performance are tested in different test cases, with the objective of highlight the combination which leads to the best results.

5.5.1 OSIRIS-REx MISSION SCENARIO

In order to investigate the performance of the proposed navigation and control system combinations, a scenario with high orbit-attitude coupling is proposed. Particularly, the NASA's asteroid-study and sample-return mission, OSIRIS-REx, mission is considered. The available data of this mission are used to define the properties of the spacecraft and the small irregular asteroid Bennu, whose properties were given in Table 2.1.

The spacecraft is a cubical platform with $2.3 \times 2.3 \times 2$ m in size and with a dry mass of 850 kg. The control system performs the orbital control through 4 thrusters with a nominal thrust of 275 N each. The attitude control is performed thought 16 thrusters with a nominal thrust of 4.5 N each for large maneuver, and it uses 4 reaction wheels for standard vehicle pointing. Typically the torque produced by reaction wheels lies between $10^{-1} - 1$ Nm. The spacecraft is able to store about 1200 kg of hydrazine mono propellant. The navigation system is equipped with precise sensors, particularly there are 2 star trackers and 2 IMU (Inertial Measurement Units) for attitude and angular velocity measurements. A camera system which uses LIDAR (Light Detection and Ranging) and TAGCAMS (Touch And Go Camera System) deliver assistance when navigating in close proximity to the asteroid.

The details of spacecraft properties and the control and navigation systems are reported in Table 5.9. It has been assumed that the attitude control is performed thought three reaction wheels, one for axis, with a saturation limits of 1 N each. In addition, even for the nominal case study, the sensors employed in the navigation system are assumed to be characterized by a worse statistics than the real-world scenario; i.e., the standard deviations are assumed to be relatively large in order to verify the robustness of the proposed navigation and control systems.

Table 5.9: Values used for the spacecraft properties and navigation and control systems [120, 121].

Parameter	Values
Spacecraft mass [kg]	$m = 850$
Spacecraft dimension [m]	$d_1 = 2.0$, $d_2, d_3 = 2.3$
Spacecraft inertia [kg m ^{2}]	$J = \frac{m}{12}\text{diag}\left[\left(d_1^2 + d_2^2\right), \left(d_2^2 + d_3^2\right), \left(d_1^2 + d_2^2\right)\right]$
Propellant mass [kg]	$M_p = 1100$
Exhaust flow velocity [m/s]	$v_e = 2000$
Control moment saturation per axis [N m]	$M_{c,i} = 1$
Control force saturation per axis [N]	$F_{c,i} = 366$
Measurement std [deg,m,deg,m/s]	$\sigma_{\zeta_\Theta} = 0.1 \times \frac{180}{\pi}$, $\sigma_{\zeta_r} = 100$, $\sigma_{\zeta_\omega} = 0.002 \times \frac{180}{\pi}$, $\sigma_{\zeta_v} = 2$

The tracking orbit is chosen based on the mission timeline. Just before the TAG (Touch-and-Go) operation, the spacecraft flies a closed orbit with a radius of 0.6 miles (1 km) around Bennu. This phase is also important for the scientific return of the mission, since the spacecraft collects asteroid's data to map its surface. For this reason, it is assumed a desired (reference) circular orbit with a nonzero inclination, and a nadir-pointing attitude such that a face of the satellite always points to the surface of the asteroid. The orbit is parameterized through trigonometric functions as done in the previous case studies, with the following values: $r_o = 1$ km, $R_o = R([0, \pi/3, 0])$. In order

to guarantee the nadir pointing attitude, the local vertical local horizontal (LVLH) reference frame is introduced, whose representation is given in Fig. 5.22. The first axis is oriented in the $v_{ref}(t)$ direction, $\hat{e}_{1,LVLH}(t) = v_{ref}(t)/\|v_{ref}(t)\|$; the third axis is is oriented in the $-r_{ref}(t)$ direction, $\hat{e}_{3,LVLH}(t) = -r_{ref}(t)/\|r_{ref}(t)\|$; the second axis is normal to the orbit plane and in the direction of angular momentum h with opposite sign, $\hat{e}_{2,LVLH}(t) = \hat{e}_{2,LVLH}(t) \times \hat{e}_{1,LVLH}(t)$. The reference angular velocity is simply defined as $\omega_{ref}(t) = -n_o\, \hat{e}_{2,LVLH}$ [122, 123]. The guidance system computes the reference attitude at each instant of time as

$$\theta_{ref}(t) = \log_{\mathsf{SO(3)}}\left(R^T_{LVLH}(t)\right) \tag{5.14}$$

where R_{LVLH} is the rotation matrix from BCI to LVLH reference frame

$$R_{LVLH}(t) = \begin{bmatrix} \hat{e}_{1,LVLH}(t)\cdot\hat{I} & \hat{e}_{1,LVLH}(t)\cdot\hat{J} & \hat{e}_{1,LVLH}(t)\cdot\hat{K} \\ \hat{e}_{2,LVLH}(t)\cdot\hat{I} & \hat{e}_{2,LVLH}(t)\cdot\hat{J} & \hat{e}_{2,LVLH}(t)\cdot\hat{K} \\ \hat{e}_{3,LVLH}(t)\cdot\hat{I} & \hat{e}_{3,LVLH}(t)\cdot\hat{J} & \hat{e}_{3,LVLH}(t)\cdot\hat{K} \end{bmatrix} \tag{5.15}$$

The spacecraft initial conditions are chosen reasonably different from the desired ones, i.e. reference orbit and nadir-pointing attitude. All the states are selected randomly from Gaussian distributions with a standard deviations of 90 deg, 1000 m, 5 deg/s and 1 m/s for attitude, position, and velocities respectively. On the other hand, the UKF initial conditions are selected with an error of 10% for attitude and position and 20% for velocities, with respect to the spacecraft initial conditions.

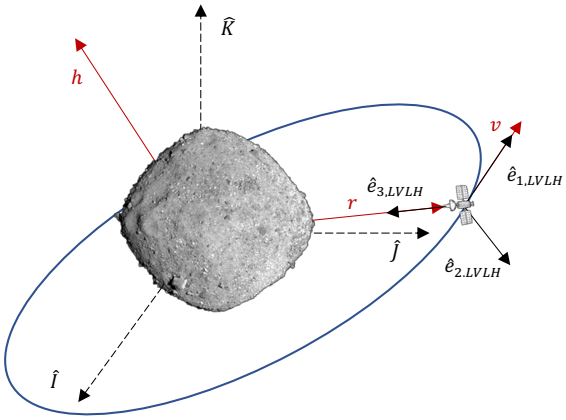

Figure 5.22: Local vertical local horizontal (LVLH) and body-centered inertial (BCI) frames representation.

5.5.2 PERFORMANCE ANALYSIS

This section has the purpose of tuning the proposed control and navigation system combinations, such that a preliminary analysis of their performance can be conducted. There are several gains that need to be chosen for the control and navigation systems, and those values are not retrieved with any optimized algorithm. As done in Sections 5.10-5.12, they are found with a trial and error procedure. However in this case the tuning

process is more complicated. The navigation system measures through the sensors, estimates the spacecraft states filtering the noise and provide them to the control system. This latter one can actuate the control law on the basis of the tracking error which is computed between the estimated states and the reference states provided by the guidance system. It is clear that when the closed-loop system is considered, the navigation and control systems influence each other. Particularly the role of the navigation system is critical to assure the convergence of the system. In fact, if the state filter/observer does not converge then, a wrong tracking error and control corrective action are computed. On the other hand, having a control system that is not able to nullify the tracking error (as result of a wrong tuning, for instance), does not imply that the navigation filter has not converged.

The tuning procedure has been carried out with the objective of having a similar settling time and steady state errors between the four proposed navigation and control system. Particularly, the gains are chosen such that position and attitude accuracy may reach ≈ 1 m and ≈ 1 deg respectively, in about 1000 s. As result of this procedure, all the gain values reported in Tab. 5.10 (UKF-MLBS), Tab. 5.11 (UKF-SMC), Tab. 5.12 (STO-MLBS, STO-SMC).

As result of the preliminary tuning procedure, it has verified that the STO and SMC are more difficult to tune with respect to the UKF and the MLBS. Particularly, the selection of inappropriate gains can lead to the chattering phenomenon near the sliding surface, and then the tracking errors never achieve the previous performance indexes. This is particularly problematic for the STO attitude estimation. In order to guarantee the STO performance, the attitude gain B_1 in Tab. 5.12 is lowered once the observer has converged. This method leads to a larger estimation error, especially for the attitude. Another disadvantage of the STO navigation system is that it needs to be provided with the spacecraft control input u_c. On the other hand, the UKF is able to assure convergence and accuracy just using an estimation of the gravity input $\hat{u} = \hat{u}_g$. The filter is basically able to blend the information that come from the propagation and the measurements, to produce estimates which are consistent with the plant states.

Table 5.10: Values used for the UKF-MLBS navigation and control systems.

Parameter	Values
Measurement cov matrix [deg,m,deg,m/s]	$T = \text{blckdiag}\left[\sigma^2_{\zeta_\Theta} I_3, \sigma^2_{\zeta_r} I_3, \sigma^2_{\zeta_\omega} I_3, \sigma^2_{\zeta_v} I_3/10\right]$
Process cov matrix [deg,m,deg,m/s]	$Q = 10^{-7} I_{12}$
State cov matrix [deg,m,deg,m/s]	$P_0 = 10^{-10} I_{12}$
$\kappa\,[km\,s^{-2}]$	10^{-6}
$k_{11}\,[\text{s}^{-1}]$	$6 \cdot 10^{-3}$
$k_{12}\,[\text{s}^{-1}]$	0.01
$k_{21}\,[\text{s}^{-1}]$	$2 \cdot 10^{-2}$
$k_{22}\,[\text{s}^{-1}]$	0.01
$k_{31}\,[\text{s}^{-2}]$	0
$k_{32}\,[\text{s}^{-2}]$	10^{-9}
$a\,[-]$	$\begin{bmatrix}1.2 & 1.1 & 1\end{bmatrix}^T$

Table 5.11: Values used for the UKF-SMC navigation and control systems.

Parameter	Values
Measurement cov matrix [deg,m,deg,m/s]	$T = \text{blckdiag}\left[\sigma^2_{\zeta_\Theta} I_3, \sigma^2_{\zeta_r} I_3, \sigma^2_{\zeta_\omega} I_3, \sigma^2_{\zeta_v} I_3/10\right]$
Process cov matrix [deg,m,deg,m/s]	$Q = 10^{-7} I_{12}$
State cov matrix [deg,m,deg,m/s]	$P_0 = 10^{-5} I_{12}$
$K_{\sigma,M}$ [kNm]	100
$K_{\sigma,F}$ [kN]	100
k_{11} [s^{-1}]	10^{-5}
k_{12} [s^{-1}]	1
c_{11} [s]	10^{-9}
c_{12} [s km^{-1}]	0.05
c_{21} [-]	10^{-11}
c_{22} [km^{-1}]	$3 \cdot 10^{-5}$
c_{31} [-]	0
c_{32} [km^{-1}]	$1 \cdot 10^{-10}$
k_{11} [s^{-1}]	$1 \cdot 10^{-5}$
k_{12} [s^{-1}]	1
a [−]	$\begin{bmatrix}1.2 & 1.1 & 1\end{bmatrix}^T$

Table 5.12: Values used for the STO-MLBS navigation and control systems (left). Values used for the STO-SMC navigation and control systems (right).

Parameter	Values
G_1 [s,s/m]	10^{-5}
G_2 [-,m^{-1}]	10^{-1}
B_1 [-]	50 for $t \leq 400$, then 10^{-8}
B_2 [-]	$6 \cdot 10^{-2}$
B_{31} [1/s]	10^{-6}
B_{32} [m/s]	10^{-6}
κ [$km\,s^{-2}$]	10^{-6}
k_{11} [s^{-1}]	0.005
k_{12} [s^{-1}]	0.005
k_{21} [s^{-1}]	0.02
k_{22} [s^{-1}]	0.1
k_{31} [s^{-2}]	0
k_{32} [s^{-2}]	10^{-9}
a [-]	$\begin{bmatrix}1.2 & 1.1 & 1\end{bmatrix}^T$

Parameter	Values
G_1 [s,s/m]	10^{-5}
G_2 [-,m^{-1}]	10^{-1}
B_1 [-]	50 for $t \leq 180$, then 10^{-8}
B_2 [-]	1
B_{31} [1/s]	10^{-6}
B_{32} [m/s]	10^{-6}
$K_{\sigma,M}$ [kNm]	100
$K_{\sigma,F}$ [kN]	100
k_{11} [s^{-1}]	0.001
k_{12} [s^{-1}]	1
c_{11} [s]	10^{-9}
c_{12} [s km^{-1}]	0.01
c_{21} [-]	10^{-11}
c_{22} [km^{-1}]	10^{-4}
c_{31} [-]	0
c_{32} [km^{-1}]	0
k_{11} [s^{-1}]	0
k_{12} [s^{-1}]	0
a [−]	$\begin{bmatrix}1.2 & 1.1 & 1\end{bmatrix}^T$

In Fig. 5.23 the norm of the difference between the reference states and the spacecraft states for the four proposed navigation and control systems are shown. The four sys-

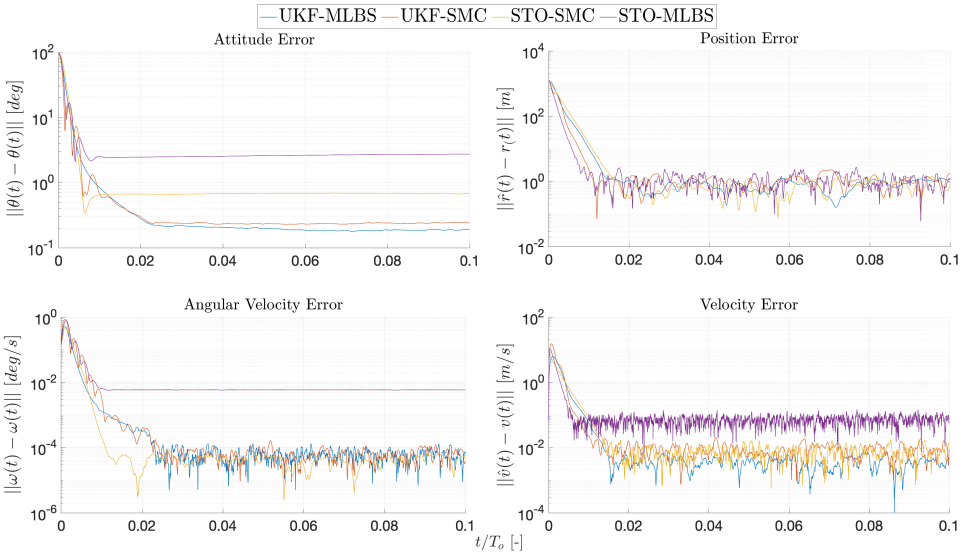

Figure 5.23: Norm of the difference between the reference states and the spacecraft states, obtained closing the loop with the proposed navigation and control systems.

tems are able to reach the spacecraft to the orbit with high accuracy, particularly with an error in the order of 1 m on position. On the other hand, the UKF-MLBS and UKF-SMC are able to handle better the rotational dynamics thus leading to highest accuracy of ≈ 0.1 deg on the attitude. However it was expected, according to the previous comments on the selection of the appropriate STO gains. Generally, STO-MLBS combination is the one with the poorest accuracy, while the UKF-based system are able to reach the highest accuracy. In Fig. 5.24, the four trajectories are shown in the initial maneuver. It is interesting to see that the UKF-MLBS and UKF-SMC overshoot before converging to the orbit, while the STO-MLBS and STO-SMC don't. Probably the reason lies in the fact that STO has a faster convergence than the UKF, as shown in Section 5.3. However, it can be seen that the four trajectories reach the reference orbit with high accuracy, as also confirmed by Fig. 5.23.

In Fig. 5.25 the norm of the control force and moment are reported for the four proposed navigation and control systems. Clearly the control actions never become zero because the control systems continuously control the spacecraft, in order to keep it with its principal axis along the nadir direction and in a non natural orbit. Even if the filter/observer have good performance in filtering the noise, some residual noise is expected. In addition, the figure in logarithmic scale highlight the presence of the noise in the signals. It can be seen that generally the control moments reach the same order of magnitude once the spacecraft reached the steady state. The same cannot be said for the control force, where the STO-MLBS, followed by the STO-SMC, have highest values. The magnified portions in Fig. 5.25 show the initial control action exerted by the four proposed navigation and control systems. It can be noted that the STO-SMC and STO-MLBS are more noisy than UKF-SMC and UKF-MLBS, and it due to the observer nature. In addition, the

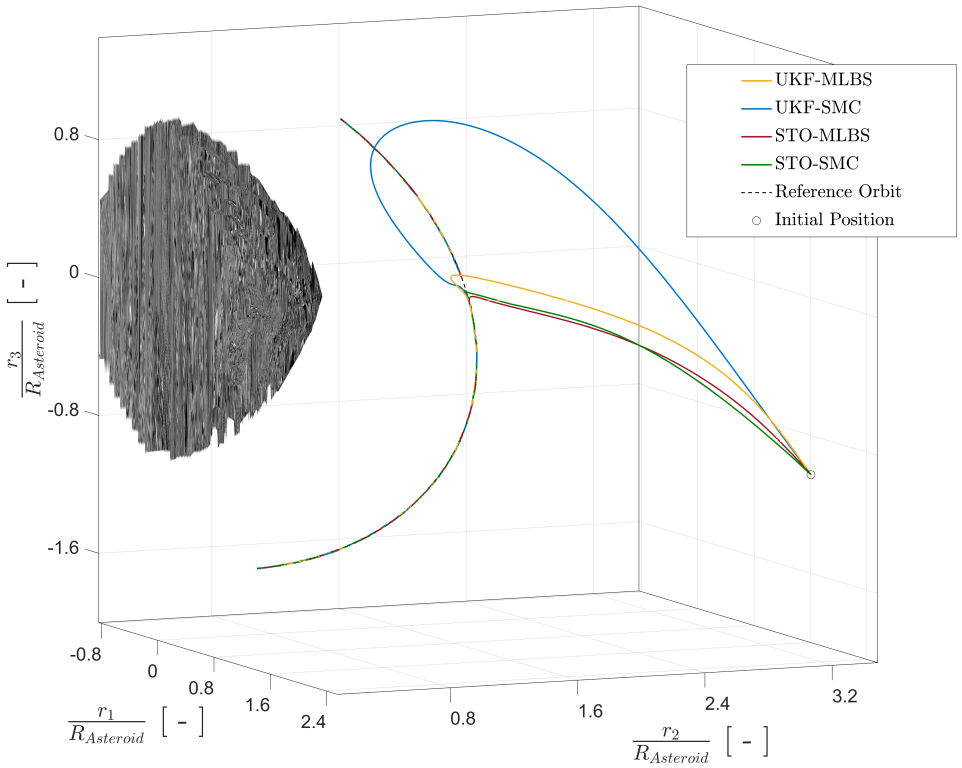

Figure 5.24: Initial maneuver zoom for the four navigation and control system combinations.

UKF-MLBS uses the lowest control force and moments to lead the spacecraft to the orbit, thus explaining the largest overshoot in Fig. 5.24. During the tuning procedure, it has been verified that increasing the gains led to a faster convergence with a larger amount of control force than with the actual tuning. However the accuracy does not improve or reduce meaningfully. Hence, it is preferred to keep the gains low and still satisfy the performance indexes described at the beginning.
In Tab. 5.15 additional performance indexes are reported for the four systems. In agreement with the analysis conducted in Section 5.4, the two MLBS systems are the ones which perform better in terms of burnt propellant mass, ΔV and integrated control moment $\Delta\tau$. It can be seen that the STO-SMC uses a large amount of propellant, according to the high steady state value of control force in Fig. 5.25.
Before proceeding with the case studies it is important to underline all the quantities related to the spacecraft state, involved in the closed-loop systems. Fig. 5.26 shows the schematic representation of the closed-loop system with with spacecraft, navigation and control systems. The spacecraft states x are measured through the sensors which pass the measured state x_m to the state filter. The estimated state $\hat{x}$ is used along with the reference x_{ref} produced by the guidance system, to compute the state tracking error δx. Then the control system can actuate the corrective action u_c to nullify the error δx.

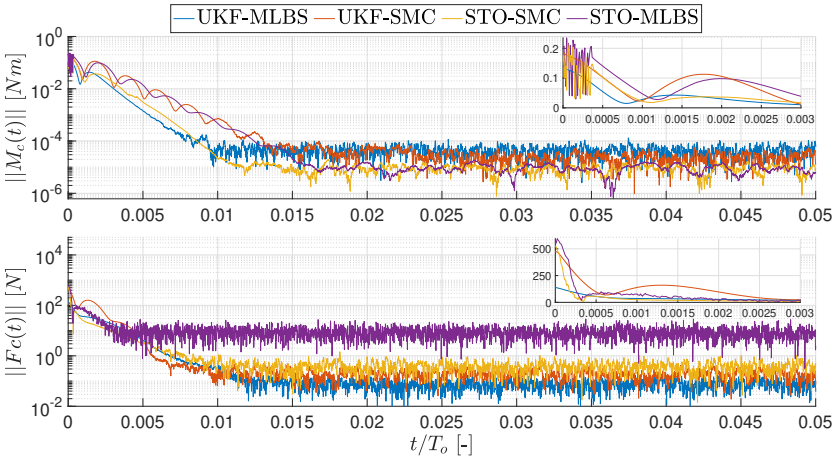

Figure 5.25: Norm of the control force and moment for the four proposed systems.

Table 5.13: Performance of the proposed navigation and control systems: ΔV, $\Delta\tau$, control input peaks and propellant mass burnt.

System	$\Delta V\,[km/s]$	$\|a_{cm}\|[km/s]$	$\Delta\tau\,[Nms]$	$\|\tau_{cm}\|[Nm]$	$\Delta M_p\,[kg]$
UKF-MLBS	0.0229	$0.1636\cdot10^{-3}$	15.0798	0.1430	9.8579
UKF-SMC	0.0603	$0.5593\cdot10^{-3}$	28.6157	0.1889	26.0942
STO-MLBS	0.0538	$0.6205\cdot10^{-3}$	15.0941	0.2204	21.8810
STO-SMC	0.9186	$0.6995\cdot10^{-3}$	28.6567	0.2351	368.6349

The total error between the spacecraft state and the reference state is computed as

$$\begin{aligned}\Delta x &= x - x_{ref}\\ &= x - \hat{x} - x_{ref} + \hat{x}\\ &= (x - \hat{x}) - (x_{ref} - \hat{x})\\ &= \delta\hat{x} - \delta x\end{aligned} \tag{5.16}$$

where $\delta\hat{x}$ is the navigation system error with respect to the spacecraft state, and δx is the tracking error which is defined through the estimated state. As discussed at the beginning of this section, the spacecraft state can converge to the desired states only if the navigation system has converged. In fact, if $\delta\hat{x}$ is large, then the control system minimizes the difference $\delta x = x_{ref} - \hat{x}$, which does not guarantee that $x \to x_{ref}$. Therefore, in order to assure that $\Delta x \to 0$, it is necessary that $\delta\hat{x} \to 0$.
In Fig. 5.27, the aforementioned states are shown for the UKF-MLBS system and for the attitude and position states. There are four different quantities depicted in this figure: the measured states (blue dot), filtered states (yellow), spacecraft states (red) and reference states (black dash). It can be seen that the spacecraft states start with a certain error with respect to the reference, and also the filtered states have initial conditions different from the spacecraft states. The measured states resemble the spacecraft ones with the

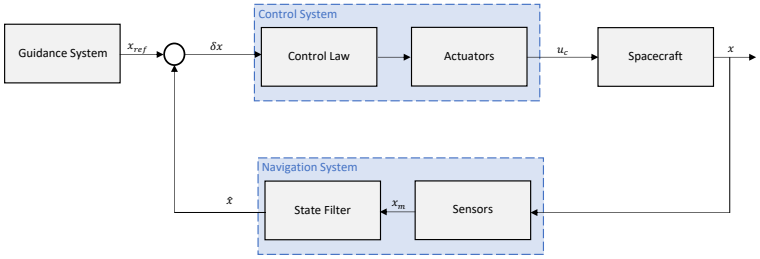

Figure 5.26: Schematic representation of the closed-loop system with spacecraft, navigation and control systems.

addition of noise, as result of the sensors model employed in the simulation. It can be noted that the filtered states converge to the spacecraft states and both of them to the reference states.

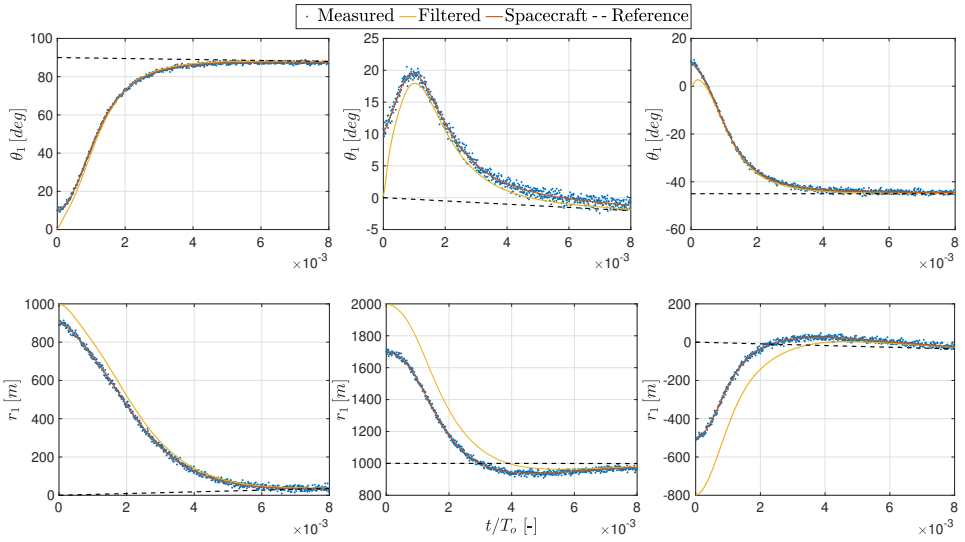

Figure 5.27: UKF-MLBS system, measured, filtered, spacecraft and reference states.

5.5.3 CASE 1: SAMPLING FREQUENCY

The four proposed navigation and control systems are tested with different sampling frequencies (time steps). The starting Δt is selected to be $\Delta t = 0.5$ s, since the UKF has an high computational cost, and the simulation time would result too high. The time step is increased until the closed-loop system diverges. This procedure showed that the STO-MLBS and STO-SMC are able to converge even with the low sampling frequency of $f_s = 0.05$ Hz ($\Delta t = 20$ s). On the other hand, the UKF-MLBS and UKF-SMC are not able

to handle with large time steps. In Fig. 5.28 the specific integrated control force and the integrated control moment are shown along with the time step. In agreement with the preliminary analysis, for the smallest Δt the UKF-MLBS and UKF-SMC perform better than the STO-MLBS and STO-SMC. However, while Δt increases, their performance decreases tremendously. On the other hand, the STO-MLBS and STO-SMC are able to keep almost a constant trend with respect the time step, thus increasing not meaningfully. In Fig. 5.29, the results are shown in terms of the statistics of the norm of the state errors (between spacecraft and reference states). In agreement with the previous results, it can be seen that STO-MLBS and STO-SMC are able to keep almost a constant accuracy with the time step. On the other hand the UKF-MLBS and UKF-SMC are more influenced by Δt. Particularly, when $\Delta t \geq 6$ s, their performance becomes unacceptable.

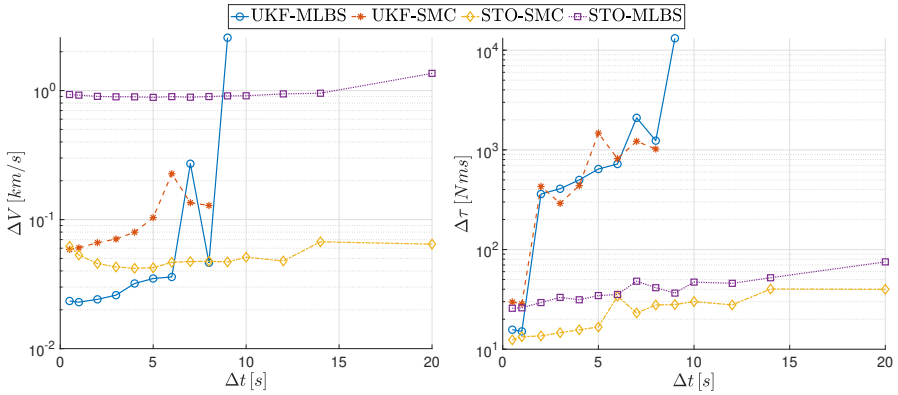

Figure 5.28: ΔV and $\Delta\tau$ for the four proposed systems with respect the sampling time Δt, which is the inverse of the sampling frequency f_s.

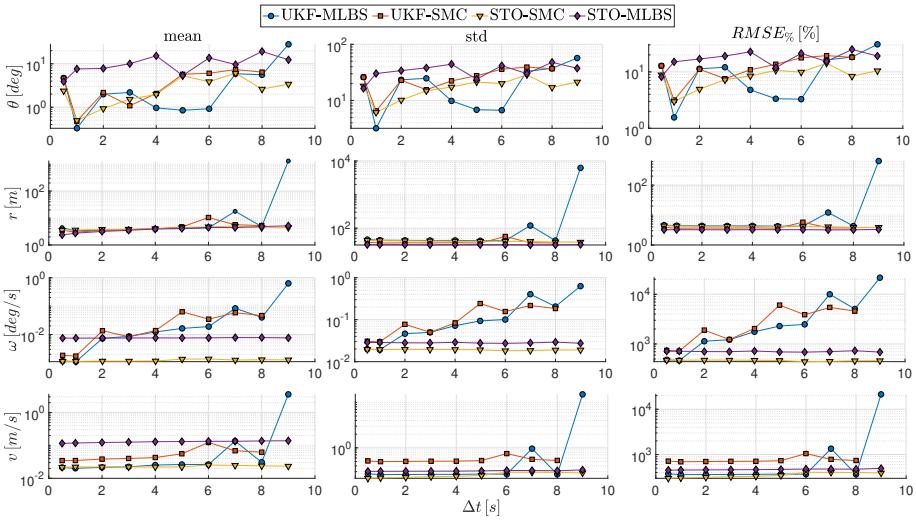

Figure 5.29: State error statistics (mean, std and normalized RMSE) with respect the sampling time Δt, which is the inverse of the sampling frequency f_s.

5.5.4 CASE 2: INACCURATE INITIAL CONDITIONS

The four proposed navigation and control systems are tested with respect the uncertainty on the initial navigation systems initialization, i.e. the initial estimates. The same procedure applied in Section 5.3 is reproduced, where the uncertainty percentage γ is introduced.

Fig. 5.31 shows how the the specific integrated control force and the integrated control moment vary with respect γ. It can be seen that UKF-MLBS and UKF-SMC have the minimum ΔV when the uncertainty is close to 0%, while ΔV increases while γ increases. The STO-SMC follows almost the same behavior of the previous two navigation and control systems. STO-MLBS, instead, has the highest ΔV, which does not vary meaningfully with respect γ. On the other hand, the UKF-SMC and UKF-MLBS are more robust in terms of $\Delta\tau$ when the uncertainty γ assumes large values. While STO-MLBS and STO-SMC don't follow a regular behavior, pointing out that those systems can experience issue when the rotational state initial estimates differ particularly from the true initial states. In Fig. 5.30, the results are shown in terms of the statistics of the norm of the state errors (between spacecraft and reference states). It can be seen that the position and velocity of the four systems follow the same behavior of ΔV, while the attitude and angular velocity evolve as $\Delta\tau$. It can be seen that between the four state error norms, the attitude error is the one which evolves more erratically, especially for STO-MLBS and STO-SMC. This result confirm the previous comment, i.e. the observer performance can be compromise meaningfully on the attitude estimation for large initial estimate uncertainty.

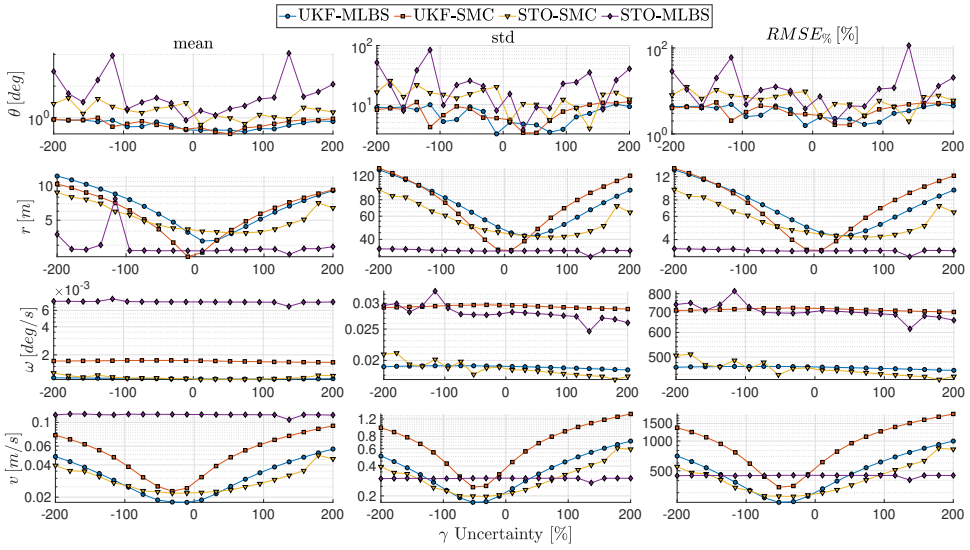

Figure 5.30: State error statistics (mean, std and normalized RMSE) with respect the initial state estimate uncertainty γ.

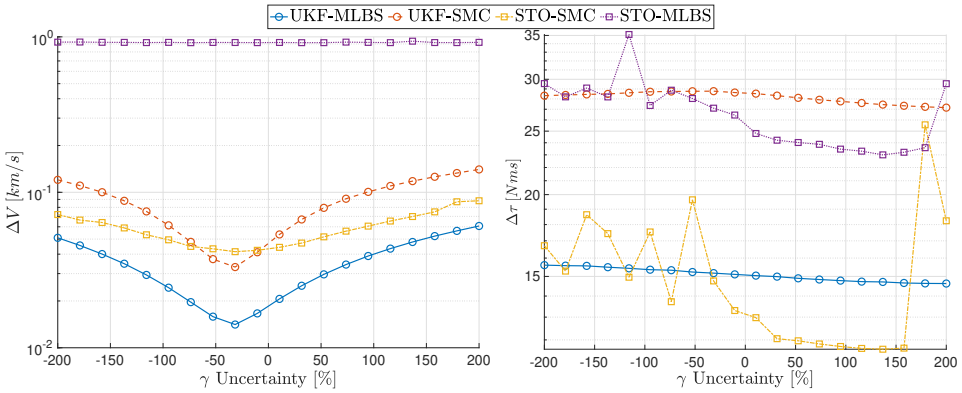

Figure 5.31: ΔV and $\Delta\tau$ for the four proposed systems with respect the initial state estimate uncertainty γ.

5.5.5 CASE 3: SENSITIVITY TO NOISE MEASUREMENT

In this section, the performance of the proposed systems is analyzed with respect the accuracy of the provided measurements. Particularly the two sets of noise standard deviations shown in Tab. 5.14 are used. The first sets represents a navigation system employed with very accurate and precise sensors thus explaining the low measurement noise standard deviation of each state. The second set, instead, represents a navigation system employed with very noisy sensors. The case study considered in the first place had standard deviations in between these new two sets.

Table 5.14: case study measurement noise standard deviations.

Parameter	Measurement Noise (low)	Measurement Noise (high)
Attitude $[deg]$	$\sigma_{\zeta_\theta} = 0.001$	$\sigma_{\zeta_\theta} = 0.5 \cdot \frac{180}{\pi}$
Position $[m]$	$\sigma_{\zeta_r} = 1$	$\sigma_{\zeta_r} = 500$
Angular Velocity $[deg/s]$	$\sigma_{\zeta_\omega} = 0.001$	$\sigma_{\zeta_\omega} = 0.01 \cdot \frac{180}{\pi}$
Velocity $[m/s]$	$\sigma_{\zeta_v} = 1$	$\sigma_{\zeta_v} = 10$

In Fig. 5.32 the norm of the state errors are reported for the proposed systems with the low measurement set (dash lines) and for the high measurement set (solid lines). With the low set of noise, the results resemble the results obtained in Sections 5.4 - 5.3. The UKF is generally able to estimate with higher accuracy the position and the attitude with respect the STO, and the MLBS can generally achieve lower steady state errors than SMC. As matter of fact, the UKF-MLBS and UKF-SMC achieve the best performance between the four systems, and they are even able to avoid the error jump due the the discontinuity of θ_1. The STO-MLBS and STO-SMC achieve a position accuracy comparable to the UKF-SMC, while the attitude estimation accuracy is not even comparable to them. When the high set of noise is used, the STO-MLBS and STO-SMC are not able to converge, as possible to see from the interrupted lines at $\approx 0.1\, t/T_o$. The UKF-MLBS and UKF-SMC, don't present particular problems even if, as expected, the order of magnitude of the steady state errors increase. Even with this large measurement noise, the steady state

errors assume order of magnitude comparable with the ones of the nominal case study. However, the attitude error experiences a decrease of accuracy in correspondence of the discontinuity.

In Tab. 5.15 the performance of the proposed systems is represented with the control moment an force characteristics. The STO-MLBS (high) and STO-SMC (high) are not reported since they are not able to converge.

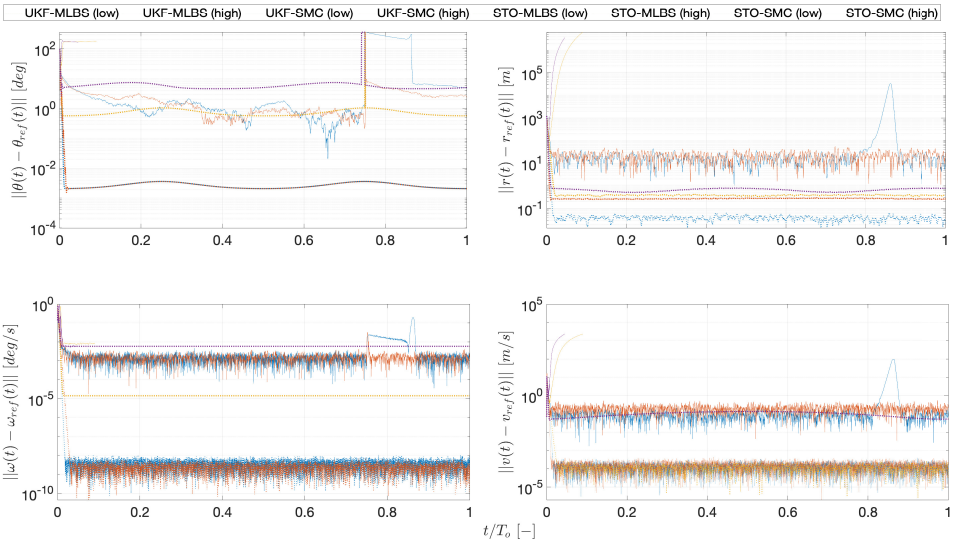

Figure 5.32: Norm of the difference between the reference states and the estimated states, obtained for "low" and "high" measurement noise statistics.

Table 5.15: Performance of the proposed navigation and control systems: ΔV, $\Delta\tau$, control input peaks and propellant mass burnt.

System	$\Delta V\,[km/s]$	$\|a_{cm}\|\,[km/s]$	$\Delta\tau\,[Nms]$	$\|\tau_{cm}\|\,[Nm]$	$\Delta M_p\,[kg]$
UKF-MLBS (low)	0.012094	$0.116\cdot10^{-3}$	11.493	0.14871	5.1228
UKF-MLBS (high)	0.68411	$0.63108\cdot10^{-3}$	91.875	0.14789	290.56
UKF-SMC (low)	0.029785	$0.40058\cdot10^{-3}$	23.965	0.19695	12.949
UKF-SMC (high)	0.49902	$0.5593\cdot10^{-3}$	72.995	0.19266	213.36
STO-MLBS (low)	0.014822	$0.6205\cdot10^{-3}$	12.509	0.17617	5.8735
STO-SMC (low)	0.027191	$0.6995\cdot10^{-3}$	26.032	0.20961	10.478

5.6 CONCLUSION AND DISCUSSION

In Section 5.3 the two proposed navigation systems have been tested in open-loop. The results of this comparison are summarized in Tab.5.16. The UKF has the main advantage of being accurate even with large source of measurement noise and large initial condition uncertainties. The initial state error covariance matrix can help to take care of initial large uncertainties. However, the UKF is less robust than STO to change in sample frequency, and requires an higher computational cost. This latter feature was expected since the complex formulation of UKF as compared to the STO. For the preliminary performance assessment, the STO system takes about 20 s to run, while the UKF system took about 60 s (for 2 hours simulation)[1].

Table 5.16: Navigation systems comparison summary.

Unscented Kalman Filter	Super-Twisting Sliding Mode Observer
• Good convergence time • High computational cost • Very sensitive to measurement noise. For low measurement noise, very high accuracy. For high measurement noise, high accuracy • For high sample frequency high accuracy, but performance decreases for small sample frequency • Convergence guaranteed even with large initial condition uncertainties. Possibility of additional tuning through initial state error covariance	▪ Low convergence time ▪ Low computational cost ▪ Not very sensitive to measurement noise. For low and high measurement noise, little difference in terms of accuracy ▪ Almost insensitive for sample frequency changing ▪ Convergence guaranteed even with large initial condition uncertainties. However, worse statistics than UKF
▪ Both the navigation algorithms are characterized by a difficult tuning due to the high number of parameters ▪ For a reasonable level of measurement noise, UFK and STO perform almost the same	

In Section 5.4 the two proposed control systems have been tested in closed-loop without measurement noise. The results of this comparison are summarized in Tab.5.17. The MLBS control law is capable of assuring convergence and good steady state error even with very small saturation limits (i.e. available control force/moment). The linearization of the system via backstepping allows the closed-loop system to behave in a good manner even with large commands. On the other hands, the SMC is characterized by a very simple and parameter-free control algorithm. It is very robust to change in sampling frequency and input noise disturbance. The computational cost of the two algorithm is almost the same. In fact, the model used for the control systems comparison took almost 120 s (for 1.6319 days simulation) to run for both the systems.

[1] The time information given in this sentence are given for the following machine: MacBook Pro, 2.8 GHz Intel Core i7, 16GB RAM. In addition, it is emphasized that the aforementioned data represented the time to run not just the UKF and STO blocks, but the model used for the navigation system comparison reported in the Appendix

Table 5.17: Control systems comparison summary.

Morse-Lyapunov Backstepping Control	Sliding Mode Control
• Few parameters to tune • Convergence guaranteed also with very small saturation limits, at cost of increasing convergence time • Insensitive to large attitude maneuvers • Small integrated control input moment • Sensitive to spacecraft parameter uncertainties • Robust to change in sampling frequency • Sensitive to input noise disturbance	▪ Lot of parameters to tune ▪ Convergence is not guaranteed with small saturation limits. Very sensitive due to discontinuous control input. ▪ Experiences trouble in convergence after a large attitude maneuver ▪ Large integrated control input moment ▪ Insensitive to spacecraft parameter uncertainties ▪ Sensitive to change in sampling frequency ▪ Robust to input noise disturbance
▪ MLBS is able to guarantee smaller steady state error than SMC, with the same control input saturation limits. ▪ The integrated control input force is the same order of magnitude. However, SMC requires more propellant mass	

Finally, in Section 5.5 the combinations obtained from the proposed navigation and control systems have been tested in closed-loop. The results of this comparison are summarized in the following points:

- The system equipped with STO-based navigation system have chattering problem, even if the sign$(\cdot)$ function is substituted with the tanh$(\cdot)$. Particularly, even if the closed-loop dynamics converges, after some time it can diverge due to the chattering motion. For this reason, one gain of the STO system has been made time-varying.

- The system equipped with STO-based navigation system are not able to convergence if the control input $u = u_c + u_g$ is not feedback inside the navigation system. It was somehow expected, since the observers require both the plant output and input. On the other hand, the UKF is able to convergence just using an estimate of the gravity input, obtained with the current state estimate.

- The UKF-based systems are able to handle better the noise measurement. The STO-based systems diverge for large measurement noise.

- The STO-based systems are able to handle better the sample frequency changes, as compared to the UKF-based systems.

- All the systems are robust to initial condition inaccuracies. However the UKF is more robust in terms of attitude. In addition, the UKF has the initial state error covariance that can take over initial condition large inaccuracies.

- Even with small noise measurement, the STO-based systems have poor accuracy compared to the UKF-based systems. Their accuracy is comparable to the accuracy of the UKF-based systems with large noise measurement.

- The STO-based systems are able to converge first than the UKF-based systems.
- Independently on the navigation algorithm, the SMC-based systems require the largest control effort. Between the two MLBS-based systems, the UKF-MLBS is the one which requires the uses control input and clearly the lowest propellant mass.
- The computational cost of the UKF-based systems is definitely higher than the STO-based systems. For 1 day of simulation time, each system requires to run:

  UKF-MLBS: $\approx$ 10 min

  UKF-SMC: $\approx$ 9.5 min

  STO-MLBS: $\approx$ 2 min

  STO-SMC: $\approx$ 1.5 min

The results obtained and summarized above, highlighted that each combination has some advantage and disadvantage. Even if the UKF-based systems requires the highest computational cost, they are preferred over the STO-based ones. The reason lies in the fact that the STO-based systems experienced issue in closed-loop convergence due to chattering, measurement noise and control input feedback. If the first problem may be resolved selecting time-varying gains, the other two are more serious. In order to feedback the control input, there is the need of using some type of sensor. However, if the STO experienced convergence issues for high source of measurement noise, it is clear that adding some source of noise to the input force/moment, can only deteriorate the STO performance. In addition, for real applications, cheap sensors may be characterized by relatively high noise measurement and inaccuracies. Therefore the UKF-based navigation systems are preferred over the STO ones. Between the UKF-MLBS and UKF-SMC, the first one is preferred. Even if the MLBS is sensitive to parameter uncertainties, its performance does not deteriorate as much to prefer to SMC ones. In addition, for sampling frequency typical of real-time application (not higher than 1 Hz), the MLBS performs definitely better in terms of accuracy, required control input and sensitivity to large commands.

In the following pages, the results of the UKF-MLBS combination are presented for the OSIRIS-REx mission case study introduced in 5.5.1. The data used are reported in Tab.5.9 and Tab.5.10, with the only difference of modifying k_{11} to $5{\cdot}10^{-4}$ and Q to $10^{-10} I_{12}$. Those changes lead to an even smaller control effort as compared to the previous case, at expense of a slightly larger larger settling time. Clearly, due to the high number of figures, those results are not reported for each navigation and control systems combination, in the preliminary performance assessment.

In Figs. 5.33-5.34 the time histories of attitude, position and velocities in the BCI frame are provided. Particularly, three different quantities are analyzed: (i) The measured states which represent the state variables measured by sensors and hence are affected by noise, (ii) the estimated (filtered) states, which are the outputs of the navigation system, and (iii) the ideal states, which are the noise-free states obtained with ideal and perfect sensors. Moreover, for each state variable, a magnified portion of the figure is also shown

to provide an approximation of the convergence times. It can be seen in the figures that the estimated states start from a different point with respect to the measured and ideal states, due to the different UKF initial conditions. However, the state filter is able to converge to the ideal states in less than a hundredth of the orbit period. Also, note that the attitude varies from −180 deg to 180 deg and the navigation scheme is able to handle this large variation with no issues. Figure 5.35 shows the trajectory of the spacecraft center

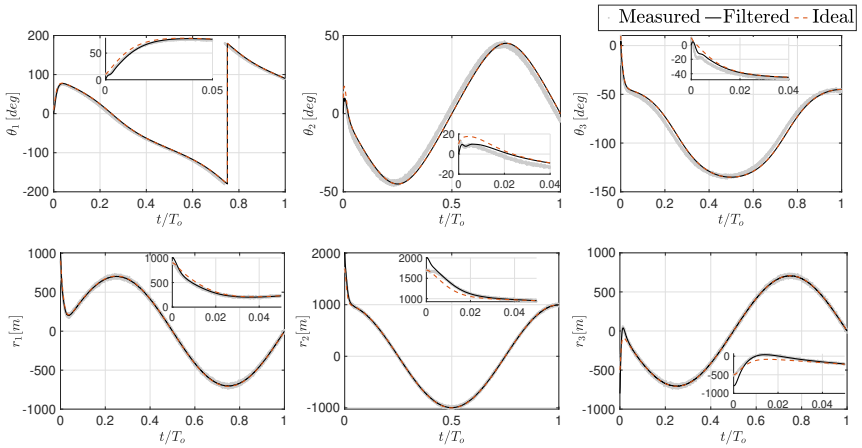

Figure 5.33: Measured (grey), estimated (black), and ideal (red) states.

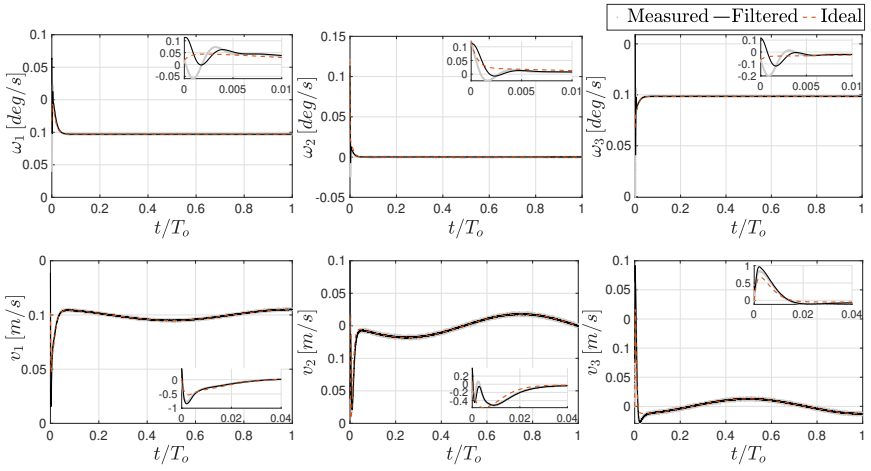

Figure 5.34: Measured (grey), estimated (black), and ideal (red) states.

of mass, the desired orbit, and the spacecraft's position and attitude at different points in the orbit. The spacecraft starts with a completely different attitude with respect to the desired ones, and in addition has an initial tumbling. The spacecraft transient response

is highlighted in the magnified window in the right panel of Fig. 5.35. The convergence of the filter and controller proposed here results in the convergence of the estimated states (including trajectory and attitude) to the actual states and desired states, as can be seen in the figure. It can be seen that as the spacecraft orbits around the asteroid, its attitude changes such that its bottom always faces towards Bennu. In each panel of Fig. 5.36, the

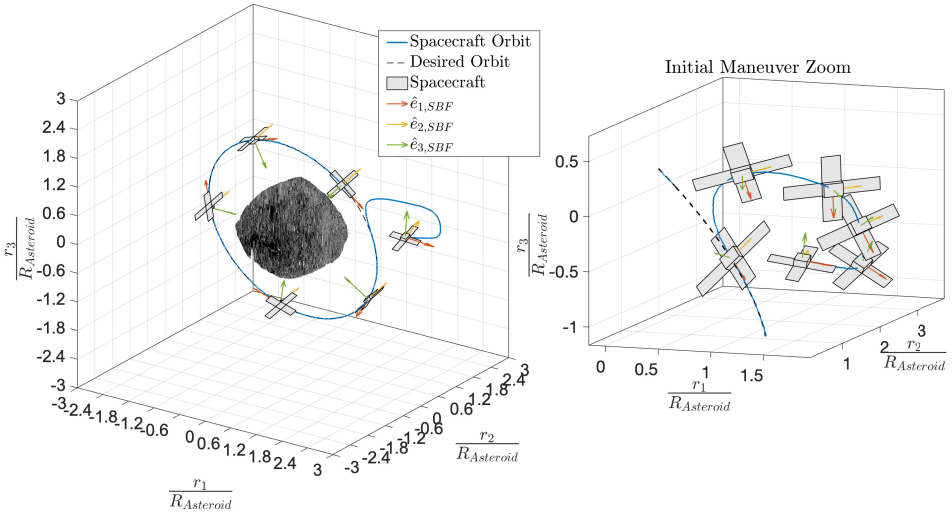

Figure 5.35: SBF orientation, and spacecraft attitude and trajectory around Bennu in BCI frame obtained via the implementation of the navigation and control systems.

norms of the differences between the spacecraft estimated states and their corresponding desired states are shown, where a noisy behavior of the aforementioned errors after the initial convergence can be seen. The attitude error has a peak in correspondence of the Θ_1 discontinuity (Fig. 5.33) and a rapid convergence. The order of magnitude of the stead state errors are satisfactorily small compared to the order of magnitude of the reference variables and the large sources of noise. For instance, the proposed navigation and control system allows to reach a position error in the order of 1 m in the orbit with 1000 m of radius and with a position noise standard deviation of 100 m. The same rationale applies to the attitude, where an accuracy of 0.0001 deg is reached. The mean and the RMSE are reported for each state error. The results improve as the numerical values of mean and RMSE decrease, as also indicated in [113]. Note that both the mean and the RMSE would reduce with time, since the number of samples with small steady state error would increase. In fact, these two indexes are influenced by the large state errors in before convergence.

In Fig. 5.37, the estimated state error between the estimated and the ideal states are shown along with the estimated confidence bounds of 3σ. The optimal performance of the estimator is generally indicated by the bounded estimation errors within the estimated standard deviation bounds [114, 124]. In other words, the UKF acts as an unbiased estimator, meaning that the expectation of the estimated state errors is zero [125].

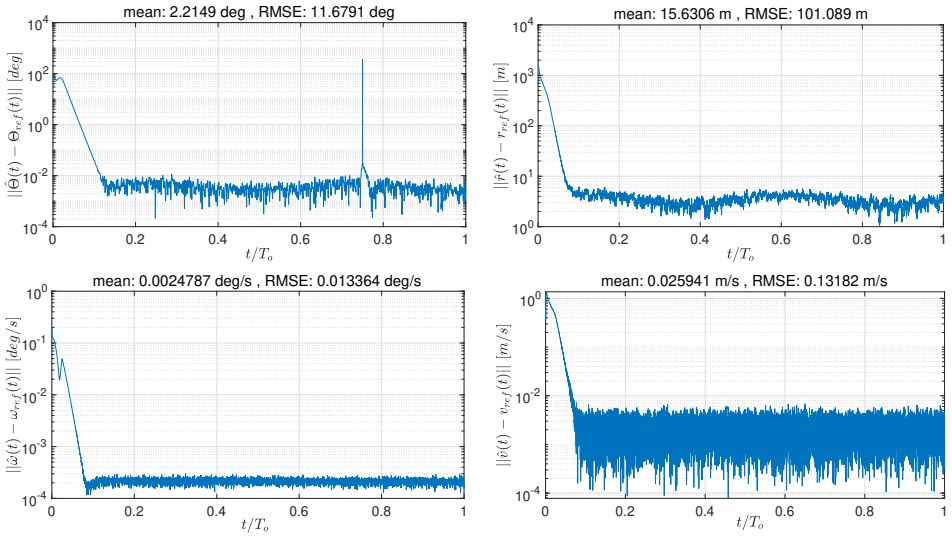

Figure 5.36: Norm of the difference between the estimated states and reference states

From a statistical point of view, it is expected that about 99% of the samples remain bounded inside the two envelopes. Additionally, the performance of the UKF confirms the fact that the state errors are approximately zero mean white noise. Note that the attitude components are characterized by a peak, which corresponds to the discontinuity of the Θ_1 when it goes from -180 deg to 180 deg, as shown in Fig. 5.33. The spacecraft can reach and maintain the desired orbit-attitude through the control system which produces the necessary control force and moment, that are shown in Fig. 5.38. In addition, the force control effort in quantified with the total integrated control force per unit mass and the moment control effort is quantified with the integrated moment. It can be seen that the proposed navigation and control system is able to guarantee the orbit and attitude tracking with a low amount of control moment and force, considering the initial conditions, the large saturation limits and noise statistics in Tab. 5.9. In fact, both F_c and M_c are well below the boundaries of 366 N and 1 Nm respectively. The total ΔV is less than those obtained in [117], where an adaptive controller was used for the orbital control. As a result of the UKF filtering action, they both appear without any residual noise, which would have introduced an extra control effort. Note that the control moment converges before the control force, in agreement with the magnified portions of Fig. 5.33-5.34. Moreover, since the orbit-attitude coupling is considered, the tracking position error can converge only if the tracking attitude error has converged. Therefore, the observed behavior is expected. It is emphasized that the gain selection is the results of a compromise between convergence time, steady state accuracy and control effort. The difference in the convergence rates may be reduced with a more aggressive control system, at the expense of a larger control effort, especially in the initial part of the trajectory.

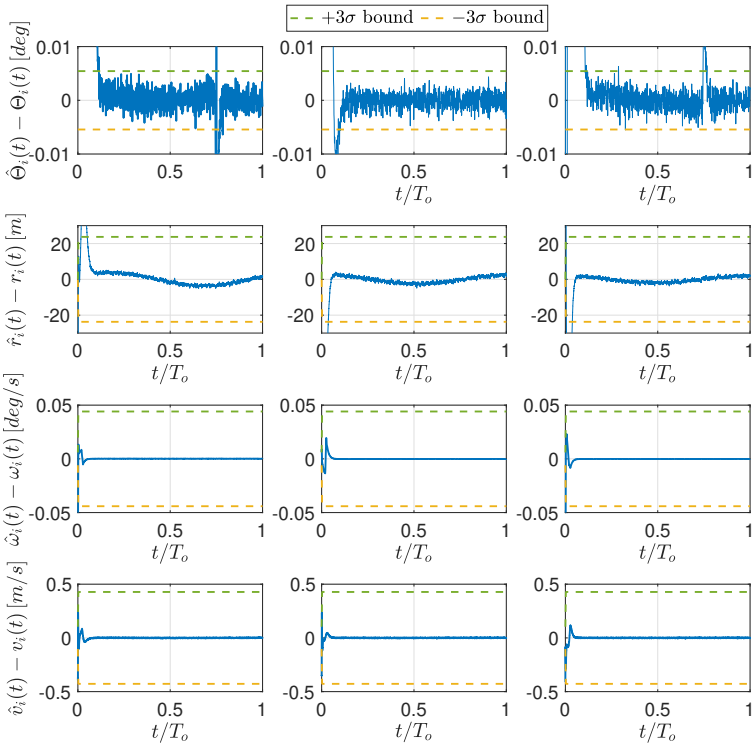

Figure 5.37: State estimation error components between the estimated states and the ideal noise-free states.

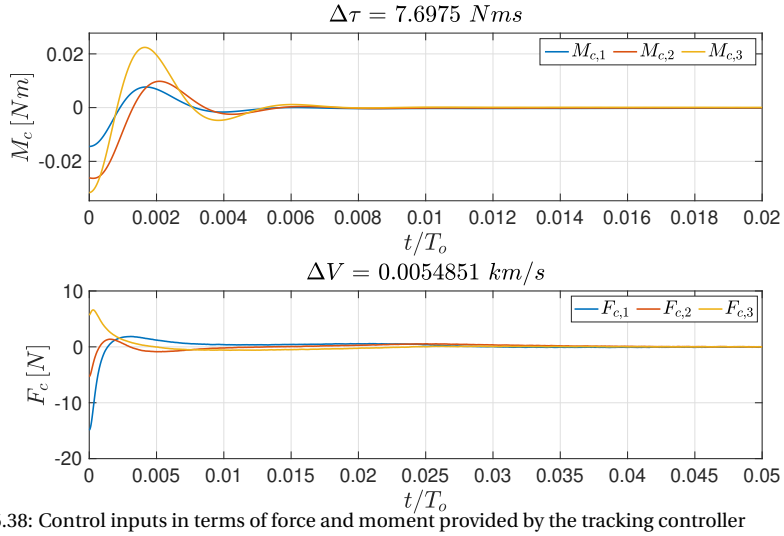

Figure 5.38: Control inputs in terms of force and moment provided by the tracking controller

Conclusions and Future Work

In this thesis, novel navigation and control algorithms are designed using the Lie groups formalism. The algorithms are applied to the problem of spacecraft motion around irregular bodies such as asteroids. In this mathematical framework, the geometrical characteristics of the system are well preserved and the translational and attitude motions are treated simultaneously.

Two different navigation systems have been designed to provide the state estimates: The Unscented Kalman Filter on $\mathsf{TSE}(3)$and the Super-Twisting Observer on $\mathsf{TSE}(3)$. The Unscented Kalman Filter computes estimates of the unknown variables by estimating a joint probability distribution over the variables for each instant of time. The Super-Twisting Observer is a deterministic state observer, meaning that the prediction of the state does not involve any source of randomness. In fact, the observer is structured as a copy of the plant and its gains remain constant throughout the process, once they are selected. Furthermore, two different control systems have been introduced: an asymptotically stable control law based on Morse-Lyapunov via Backstepping approach and a robust control law based on the Sliding Mode Control.

The navigation systems have been tested in a variety of test cases in open-loop, while the control systems have been tested in closed-loop assuming ideal measurements. The dynamics are propagated using a variational integrator. The results obtained for a rigid body spacecraft are compared to those of a point mass spacecraft in the problem of spacecraft motion around a small irregular body such as an asteroid. From those analyses, the characteristics of each of the navigation and control systems have been gathered. Finally, using the Matlab/Simulink simulation environment, different combinations of navigation and control systems have been extensively tested as well. The performance have been analyzed in terms of some performance indices such as the estimation accuracy, the tracking error, the control effort, and the propellant mass required for a simultaneous orbit-attitude tracking.

This framework proved the efficacy of the design of navigation and control algorithms on $\mathsf{TSE}(3)$allowing to preserve the geometrical characteristics of the system, while treating the translational and attitude motions simultaneously. In literature, most of the works on $\mathsf{TSE}(3)$ refers to the design of navigation and control algorithms addressed to robotic applications. However, even for a space application, the presented algorithms proved to achieve high tracking accuracy with a small required control effort. Hence, this formalism allows for the coupling between orbital and attitude motions of the spacecraft to be considered simultaneously in the design. The orbit-attitude coupling cannot be neglected in scenarios such as spacecraft motion around irregular celestial bodies due to their highly perturbed environments.

Future work may consider a more detailed modeling for the navigation system. A more accurate model of the measurement sensors may be obtained via extending their noise

characteristics to introduce biases, scale-factor errors, or mounting alignment errors. As well as, sensor fusion techniques may be used to augment the estimated states with sensors states, such as biases. Also, realistic dynamics of the actuators can be considered in the design of the control system. The robustness of the proposed navigation and control system can also be verified in problems such as orbit transfers, and spacecraft rendezvous, proximity operations, and docking. In addition, the stochastic estimation and control scheme presented here can be extended to the problem of multibody dynamics and multi-agent systems.

References

[1] Daero Lee and George Vukovich. “Robust adaptive terminal sliding mode control on SE(3) for autonomous spacecraft rendezvous and docking”. In: *Nonlinear Dynamics* (2016, doi: 10.1007/s11071-015-2479-1).

[2] D. Lee et al. “Finite-time control for spacecraft body-fixed hovering over an asteroid”. In: *IEEE Transactions on Aerospace and Electronic Systems* 51.1 (2015, doi: 10.1109/TAES.2014.140197), pp. 506–520.

[3] Daero Lee, Amit K. Sanyal, and Eric A. Butcher. “Asymptotic tracking control for spacecraft formation flying with decentralized collision avoidance”. In: *Journal of Guidance, Control, and Dynamics* 38.4 (2015, doi: 10.2514/1.G000101), pp. 587–600.

[4] Alexander Sjøberg and Olav Egeland. “An EKF for Lie Groups with Application to Crane Load Dynamics”. In: *Modeling, Identification and Control: A Norwegian Research Bulletin* 40 (Apr. 2019), pp. 109–124. DOI: 10.4173/mic.2019.2.3.

[5] S. Heo and C. G. Park. “Consistent EKF-based visual-inertial odometry on matrix Lie group”. In: *IEEE Sensors Journal* 18.9 (2018, doi: 10.1109/JSEN.2018.2808330), pp. 3780–3788.

[6] G. Bourmaud et al. “Discrete Extended Kalman Filter on Lie Groups”. In: *21st European Signal Processing Conference* (2013).

[7] G. Bourmaud et al. “Continuous-Discrete Extended Kalman FIlter on Matrix Lie Groups Using Concentrated Gaussian Distributions”. In: *Springer* 51 (2014, doi: 10.1007/s10851-014-0517-0), pp. 209–228.

[8] M. Brossard, S. Bonnabel, and J. Condomines. “Unscented Kalman filtering on Lie groups”. In: *IEEE/RSJ International Conference on Intelligent Robots and Systems (IROS)* (2017, doi: 10.1109/IROS.2017.8206066).

[9] M. Brossard, S. Bonnabel, and A. Barrau. “Unscented Kalman Filter on Lie Groups for Visual Inertial Odometry”. In: *"IEEE/RSJ International Conference on Intelligent Robots and Systems (IROS)* (2018, doi: 10.1109/IROS.2018.8593627).

[10] G. Loianno, M. Watterson, and V. Kumar. “Visual Inertial Odometry for Quadrotors on SE(3)”. In: *IEEE International Conference on Robotics and Automation (ICRA)* (2016, doi: 10.1109/ICRA.2016.7487292).

[11] Jerrold E. Abraham Ralph; Marsden. *Foundations of Mechanics*. Addison-Wesley, 1978.

[12] Taeyoung Lee. “COMPUTATIONAL GEOMETRIC MECHANICS AND CONTROL OF RIGID BODIES”. In: *PhD disseration* The University of Michigan (2008).

[13] J. Sola, J. Deray, and D. Atchuthan. “A micro Lie theory for state estimation in robotics”. In: *2018 arXiv preprint* (2018, arXiv: 1812.01537).

[14] R. M. Murray, Z. Li, and S. S. Sastry. *A Mathematical Introduction to Robotic Manipulation*. CRC Press, 1994.

[15] K. R. Pollock. “An analysis of orbital propagators for Low Earth Orbit Rendezvous”. In: *Naval Postgraduate School, Monterey, CA., Provided by the SAO/NASA Astrophysics Data System* OMB.0704-0188 (1994).

[16] S. P. Shuster. “A Survey and Performance Analysis of Orbit Propagators for LEO, GEO, and Highly Elliptical Orbits”. In: *Utah State University* OMB.0704-0188 (2017).

[17] V. Vittaldev, E. Mooij, and M. C. Naeije. “Unified state model theory and application in Astrodynamics”. In: *Celestial Mechanics and Dynamical Astronomy* 112.3 (2012, doi: 10.1007/s10569-011-9396-5), pp. 253–282.

[18] J. T.-Y. Wen and K. Kreutz-Delgado. “The attitude control problem”. In: *IEEE Transactions of Automatic Control* 36.10 (1991, doi: 10.1109/9.90228), pp. 1148–1162.

[19] S. P. Bhat and D. S. Bernstein. “A topological obstruction to continuous global stabilization of rotational motion and the unwinding phenomenon”. In: *Systems & Control Letters* 39.1 (2000, doi: 10.1016/S0167-6911(99)00090-0), pp. 63–70.

[20] J. Bohn and A. K. Sanyal. “Almost global finite-time stabilization of rigid body attitude dynamics using rotation matrices”. In: *International Journal on Robust and Nonlinear Control* 25.4 (2015, doi: 10.1002/rnc.3399).

[21] M. Nazari et al. “Morse-Lyapunov-Based Control of Rigid Body Motion on TSE(3) via Backstepping”. In: *2018 AIAA Guidance, Navigation, and Control Conference* (2018, doi: 10.2514/6.2018-0602).

[22] Nazari Morad. “AE 695I Geometric Mechanics & Control of Rigid Body Motions”. In: *Embry Riddle University* (August 2019).

[23] B. P. Malladi, S. Di Cairano, and A. Weiss. “Nonlinear Model Predictive Control of Coupled Rotational-Translational Spacecraft Relative Motion”. In: *2019 American Control Conference (ACC)*. 2019, doi: 10.23919/ACC.2019.8814345, pp. 3581–3586.

[24] Sangbum Cho, N. H. McClamroch, and M. Reyhanoglu. “Dynamics of multibody vehicles and their formulation as nonlinear control systems”. In: *Proceedings of the 2000 American Control Conference. ACC (IEEE Cat. No.00CH36334)*. Vol. 6. 2000, doi: 10.1109/ACC.2000.876955, pp. 3908–3912.

[25] N. Filipe and P. Tsiotras. “Rigid body motion tracking without linear and angular velocity feedback using dual quaternions”. In: *2013 European Control Conference (ECC)*. 2013, doi: 10.23919/ECC.2013.6669564, pp. 329–334.

[26] D. Lee and G. Vukovich. “Robust adaptive terminal sliding mode control on SE(3) for autonomous spacecraft rendezvous and docking”. In: *Nonlinear Dynamics* 83 (2016, doi: 10.1007/s11071-015-2479-1), pp. 2263–2279.

[27] D. Seo and M. Nazari. “Rigid Body Adaptive Stabilization on the Tangent Bundle of the LIE Groups”. In: *AIAA Scitech 2019 Forum* (2019, doi: 10.2514/6.2019-0653).

[28] E. A. Butcher, J. Wang, and T. Alan Lovell. “On Kalman Filtering and Observability in Nonlinear Sequential Relative Orbit Estimation”. In: *Journal of Guidance, Control, and Dynamics* 40.9 (2017, doi: 10.2514/1.G002702).

[29] C. A. Woolsey. “Reduced Hamiltonian Dynamics for a Rigid Body Coupled to a Moving Point Mass”. In: *Journal of Guidance, Control, and Dynamics* 28.1 (2005, doi: 10.2514/1.54099).

[30] Fabrizio Schiano. *What is the difference between filter and observer and estimator?* Apr. 2019.

[31] Quang Lam et al. “Gyro Modeling and Estimation of Its Random Noise Sources”. In: *AIAA Guidance, Navigation, and Control Conference and Exhibit*. DOI: 10.2514/6.2003-5562. eprint: https://arc.aiaa.org/doi/pdf/10.2514/6.2003-5562. URL: https://arc.aiaa.org/doi/abs/10.2514/6.2003-5562.

[32] L. Sy, N. H. Lovell, and S. J. Redmond. “Estimating lower limb kinematics using a Lie group constrained EKF and a reduced wearable IMU count”. In: *8th IEEE RAS/EMBS International Conference for Biomedical Robotics and Biomechatronics (BioRob)*. 2020, doi: 10.1109/BioRob49111.2020.9224342, pp. 310–315.

[33] K. Nirmal et al. “Noise modeling and analysis of an IMU-based attitude sensor: Improvement of performance by filtering and sensor fusion”. In: *Advances in Optical and Mechanical Technologies for Telescopes and Instrumentation II*. Ed. by Ramón Navarro and James H. Burge. Vol. 9912. International Society for Optics and Photonics. SPIE, 2016, doi: 10.1117/12.2234255, pp. 2138–2147. URL: https://doi.org/10.1117/12.2234255.

[34] Giuseppe Di Mauro, M. Lawn, and Riccardo Bevilacqua. “Survey on Guidance Navigation and Control Requirements for Spacecraft Formation-Flying Missions”. In: *Journal of Guidance, Control, and Dynamics* 41 (Dec. 2017), pp. 1–22. DOI: 10.2514/1.G002868.

[35] Maren Hulsmann. “Uncertainty Dispersion Analysis and Optimal Control of Atmospheric Re-Entry”. In: Universitat Bremen.

[36] Navigation Guillermo Ortega Head of the Guidance and Control Section of ESA. *ESA Guidance, Navigation, and Control Systems*. Dresdner Automatisierungstechnischen Kolloquien, 2014.

[37] E. A. Wan and R. Van Der Merwe. “The unscented Kalman filter for nonlinear estimation”. In: *Proceedings of the IEEE 2000 Adaptive Systems for Signal Processing, Communications, and Control Symposium* (doi: 10.1109/ASSPCC.2000.882463).

[38] Pierre-Antoine Absil, Robert Mahony, and Rodolphe Sepulchre. *Optimization Algorithms on Matrix Manifolds*. Princeton University Press, 2008, isbn: 978-0-691-13298-3.

[39] M. Brossard, A. Barrau, and S. Bonnabel. “A code for unscented Kalman filtering on manifolds (UKF-M)”. In: *International Conference on Robotics and Automation (ICRA)* (2020, arXiv:2002.00878).

[40] Matthew Wittal et al. “Stochastic spacecraft navigation and control in Lie group SE(3) around small irregular bodies”. In: 2020, doi: 10.13140/RG.2.2.21502.82240, AAS 20–690.

[41] Yuri Shtessel et al. “Sliding Mode Control and Observation”. In: Jan. 2014, pp. 291–320. ISBN: 978-0-8176-4892-3. DOI: 10.1007/978-0-8176-4893-0_8.

[42] T. D. Barfoot and P. T. Furgale. “Associating Uncertainty With Three-Dimensional Poses for Use in Estimation Problems”. In: *IEEE Transactions on Robotics* 30.3 (2014, doi: 10.1109/TRO.2014.2298059), pp. 679–693.

[43] Robert Grover Brown and Patrick Y. C. Hwang. *Introduction to Random Signals and Applied Kalman Filtering with Matlab Exercises, 4th Edition*. Wiley, ISBN: 978-0-470-60969-9, 2012.

[44] Q. Shen et al. “Integral-Type Sliding Mode Fault-Tolerant Control for Attitude Stabilization of Spacecraft”. In: *IEEE Transactions on Control Systems Technology* 23.3 (2015), pp. 1131–1138. DOI: 10.1109/TCST.2014.2354260.

[45] Y. -. Chen and S. -. Lo. “Sliding-mode controller design for spacecraft attitude tracking maneuvers”. In: *IEEE Transactions on Aerospace and Electronic Systems* 29.4 (1993), pp. 1328–1333. DOI: 10.1109/7.259536.

[46] Shih-Che Lo and Yon-Ping Chen. “Smooth sliding-mode control for spacecraft attitude tracking maneuvers”. In: *Journal of Guidance, Control, and Dynamics* 18.6 (1995), pp. 1345–1349. DOI: 10.2514/3.21551. eprint: https://doi.org/10.2514/3.21551. URL: https://doi.org/10.2514/3.21551.

[47] Mauro Mancini et al. “Sliding Mode Control Techniques and Artificial Potential Field for Dynamic Collision Avoidance in Rendezvous Maneuvers”. In: *IEEE Control Systems Letters* PP (July 2019), pp. 1–1. DOI: 10.1109/LCSYS.2019.2926053.

[48] Marin Kobilarov, Keenan Crane, and Mathieu Desbrun. “Lie Group Integrators for Animation and Control of Vehicles”. In: *ACM Transactions on Graphics* 28 (Apr. 2009). DOI: 10.1145/1516522.1516527.

[49] A. Muller and Z. Terze. “The significance of the configuration space Lie group for the constraint satisfaction in numerical time integration of multi body systems”. In: *Mechanism and Machine Theory* 82 (), pp. 173–202.

[50] T. Lee, H. Mcclamroch, and M. Leok. “Optimal Attitude Control for a Rigid Body with Symmetry”. In: *Proceedings of the American Control Conference* (2007, doi: 10.1109/ACC.2007.4282362).

[51] J. Gallier. “Basics of Classical Lie Groups: The Exponential Map, Lie Groups, and Lie Algebras, In: Geometric Methods and Applications"”. In: *Texts in Applied Mathematics* 38 (2001, doi: 10.1007/978-1-4613-0137-0_14), pp. 367–414.

[52] M.-A. A. H. Ahmed". “On Extracting Properties of Lie Groups from Their Lie Algebras”. In: *American Journal of Computational and Applied Mathematics* 6.5 (2016, doi: 10.5923/j.ajcam.20160605.02), pp. 182–186.

[53] M. Nazari et al. “Decentralized Consensus Control of a Rigid-Body Spacecraft Formation with Communication Delay”. In: *Journal of Guidance, Control, and Dynamics* (2016, doi: 10.2514/1.G001396).

[54] D. J. Scheeres. *Orbital Motion in Strongly Perturbed Environments*. Springer, Berlin-Heidelberg, 2012.

[55] W. M. Kaula. *Theory of Satellite Geodesy*. Blaisdell, Bosto, ISBN-13: 978-0486414652, ISBN-10: 0486414655, 1966.

[56] D. J. Scheeres et al. "Dynamics of orbits close to asteroid 4179 Toutatis". In: *Icarus* 132.1 (1998, doi: 10.1006/icar.1997.5870), pp. 53–79.

[57] M. Nazari et al. "Observer-based body-frame hovering control over a tumbling asteroid". In: *Acta Astronautica* 102 (2014, doi: 10.1016/j.actaastro.2014.05.016), pp. 124–139.

[58] Gaurav Misra and Amit K. Sanyal. "Analysis of Orbit-Attitude Coupling of Spacecraft Near Small Solar System Bodies". In: *AIAA Guidance, Navigation, and Control Conference*. DOI: 10.2514/6.2015-1777. eprint: https://arc.aiaa.org/doi/pdf/10.2514/6.2015-1777. URL: https://arc.aiaa.org/doi/abs/10.2514/6.2015-1777.

[59] G. Misra, A. Sanyal, and D. J. Scheeres. "Coupled orbit-attitude dynamics and relative state estimation of spacecraft near small solar system bodies". In: *Advances in Space Research* 57.8 (2015, doi: 10.1016/j.asr.2015.05.023), pp. 1747–1761.

[60] E. B. Bierhaus, B. C. Clark, and J. W. Harris. "The OSIRIS-REx spacecraft and the touch-and-go sample acquisition mechanism (TAGSAM)". In: *Space Sci* 214.107 (2018, doi: 10.1007/s11214-018-0521-6).

[61] E. Beshore et al. "The OSIRIS-REx asteroid sample return mission". In: *IEEE Aerospace Conference Proceedings* (2015, doi: 10.1109/AERO.2015.7118989).

[62] P.C. Thomas. "Sizes, shapes, and derived properties of the saturnian satellites after the Cassini nominal mission". In: *Icarus* 208.1 (2010), pp. 395–401. ISSN: 0019-1035. DOI: https://doi.org/10.1016/j.icarus.2010.01.025. URL: http://www.sciencedirect.com/science/article/pii/S0019103510000448.

[63] Sabrina Corpino. *Sistemi Aerospaziali - 03GKZMT, Lecture Notes*. Politecnico di Torino, Dipartimento di Ingegneria Meccanica e Aerospaziale (DIMEAS), 2019.

[64] T. D. Barfoot and P. T. Furgale. "Associating Uncertainty With Three-Dimensional Poses for Use in Estimation Problems". In: *IEEE Transactions on Robotics* 30.3 (2014, doi: 10.1109/TRO.2014.2298059), pp. 679–693.

[65] Oliver Olson. "A comparative study of the extended Kalman filter and sliding mode observer for orbital determination for formation flying about the L(2) Lagrange point". In: 2007.

[66] C. Zhang, A. Taghvaei, and P. G. Mehta. "Feedback particle filter on matrix lie groups". In: *2016 American Control Conference (ACC)*. 2016, pp. 2723–2728. DOI: 10.1109/ACC.2016.7525330.

[67] Tine Lefebvre and Herman Bruyninckx. "Kalman filters for nonlinear systems: A comparison of performance". In: *Int. J. Control* 7 (Aug. 2002).

[68] Arthur Gelb. *Applied Optimal Estimation*. M.I.T. Press, 1974.

[69] Gabriel A. Terejanu. *Unscented Kalman Filter Tutorial*. Department of Computer Science and Engineering, University at Buffalo, Buffalo, NY 14260, 2008.

[70] S. J. Julier and J. K. Uhlmann. "Unscented Filtering and Nonlinear Estimation". In: *Proceedings of the IEEE, 92(3):401–422* (2004).

[71] Mohinder Grewal and Angus Andrews. "Kalman filtering: theory and practice using MATLAB". In: *New York: John Wiley and Sons* 14 (Jan. 2001). DOI: 10.1002/9780470377819.

[72] Yi Xiong and M. Saif. "Sliding mode observer for nonlinear uncertain systems". In: *IEEE Transactions on Automatic Control* 46.12 (2001), pp. 2012–2017. DOI: 10.1109/9.975511.

[73] Sarah K. Spurgeon. "Sliding mode observers: a survey". In: *International Journal of Systems Science* 39.8 (2008), pp. 751–764. DOI: 10.1080/00207720701847638. eprint: https://doi.org/10.1080/00207720701847638. URL: https://doi.org/10.1080/00207720701847638.

[74] Di Shi, Zhong Wu, and Wusheng Chou. "Super-Twisting Extended State Observer and Sliding Mode Controller for Quadrotor UAV Attitude System in Presence of Wind Gust and Actuator Faults". In: *Electronics* 7 (July 2018), p. 128. DOI: 10.3390/electronics7080128.

[75] J. Davila, L. Fridman, and A. Levant. "Second-order sliding-mode observer for mechanical systems". In: *IEEE Transactions on Automatic Control* 50.11 (2005), pp. 1785–1789. DOI: 10.1109/TAC.2005.858636.

[76] Zhenhua Zhao et al. "Finite-time super-twisting sliding mode control for Mars entry trajectory tracking". In: *Journal of the Franklin Institute* (2015). ISSN: 0016-0032. DOI: https://doi.org/10.1016/j.jfranklin.2015.08.022. URL: http://www.sciencedirect.com/science/article/pii/S0016003215003439.

[77] T. Gonzalez, J. A. Moreno, and L. Fridman. "Variable Gain Super-Twisting Sliding Mode Control". In: *IEEE Transactions on Automatic Control* 57.8 (2012), pp. 2100–2105. DOI: 10.1109/TAC.2011.2179878.

[78] S. Janardhanan, M. un Nabi, and P. M. Tiwari. "Attitude control of magnetic actuated spacecraft using super-twisting algorithm with nonlinear sliding surface". In: *2012 12th International Workshop on Variable Structure Systems*. 2012, pp. 46–51. DOI: 10.1109/VSS.2012.6163476.

[79] Wakker K. F. Cornelisse J. W. Schoyer H. F. R. *Rocket Propulsion and Spaceflight Dynamics*. Pitman, 1979.

[80] European Space Agency (ESA). *Cassini/Huygens, ESA Education*. 2020 (accessed December 30, 2020). URL: https://sci.esa.int/documents/33648/36003/1567254416901-cassini-huygens.pdf.

[81] E. J. Sturm, T. J. Barber, and D. Roth. "Ensuring Cassini's end-of-mission propellant margins". In: *2015 IEEE Aerospace Conference*. 2015, pp. 1–9. DOI: 10.1109/AERO.2015.7119015.

[82] Gerald R. Hintz. *Orbital Mechanics and Astrodynamics*. Springer, Techniques and Tools for Space Missions, 2015.

[83] Wim van Ekeren. *Incremental Nonlinear Flight Control for Fixed-Wing Aircraft. Design and Implementation of Incremental Nonlinear Flight Control Methods on the FASER UAV*. Delft University of Technology, 2016.

[84] R. Laxman et al. "Optimal Nonlinear Dynamic Inversion-Based Flight Control System Design for an Aerospace Vehicle". In: Jan. 2020, pp. 65–86. ISBN: 978-981-15-1723-5. DOI: 10.1007/978-981-15-1724-2_8.

[85] Douglas Leith and W.E. Leithead. "Survey of gain-scheduling analysis and design". In: *Int. J. Control* (2000). DOI: 10.1080/002071700411304.

[86] L. Sonneveldt. *Adaptive Backstepping Flight Control for Modern Fighter Aircraft*. Delft University of Technology, 2010.

[87] W. Falkena. *Investigation of Practical Flight Control Systems for Small Aircraft*. Delft University of Technology, 2012.

[88] Pieter Gils et al. "Adaptive Incremental Backstepping Flight Control for a High-Performance Aircraft with Uncertainties". In: Jan. 2016. DOI: 10.2514/6.2016-1380.

[89] J. A. Farrell et al. "Command filtered backstepping". In: *2008 American Control Conference*. 2008, pp. 1923–1928. DOI: 10.1109/ACC.2008.4586773.

[90] Johann Koschorke. *Advanced Flight Control Design and Evaluation. An application of time delayed Incremental Backstepping*. Delft University of Technology, 2012.

[91] S.S. Sastry. *Nonlinear Systems. Analysis, Stability, and Control*. Springer, 1999.

[92] Weiping Li Jean-Jacques E. Slotine. *Applied Nonlinear Control: International Edition*. Prentice Hall, Englewood Cliffs,New Jersey 07632, 1991.

[93] PhD Alex Svirin. *math24.net*. https://www.math24.net/method-lyapunov-functions. 2021 (accessed March 6, 2021).

[94] A. Sanyal, N. Nordkvist, and M. Chyba. "An Almost Global Tracking Control Scheme for Maneuverable Autonomous Vehicles and its Discretization". In: *IEEE Transactions on Automatic Control* 56.2 (2011), pp. 457–462. DOI: 10.1109/TAC.2010.2090190.

[95] H.K. Khalil. *Nonlinear Systems*. Prentice Hall, Upper Saddle River, NJ, 3rd, 2002, pp. 154–156, 323–325, 346–348.

[96] J. J. Bohn, A. K. Sanyal, and E. A. Butcher. "Unscented state estimation for rigid body attitude motion with a finite-time stable observer". In: *2016 IEEE 55th Conference on Decision and Control (CDC)*. 2016, pp. 4698–4703. DOI: 10.1109/CDC.2016.7798985.

[97] L. Hui and J. Li. "Terminal Sliding Mode Control for Spacecraft Formation Flying". In: *IEEE Transactions on Aerospace and Electronic Systems* 45.3 (2009), pp. 835–846. DOI: 10.1109/TAES.2009.5259168.

[98] N. Bloise et al. “Artificial Potential Field and Sliding Mode Strategies for Proximity Operations with Obstacle Avoidance”. In: *2018 15th International Workshop on Variable Structure Systems (VSS)*. 2018, pp. 221–226. DOI: 10.1109/VSS.2018.8460264.

[99] K. Ghasemi, Jafar Ghaisari, and Farzaneh Abdollahi. “Robust formation control of multiagent systems on the Lie group SE(3)”. In: *International Journal of Robust and Nonlinear Control* 30 (Dec. 2019). DOI: 10.1002/rnc.4806.

[100] A. Chalanga et al. “Implementation of Super-Twisting Control: Super-Twisting and Higher Order Sliding-Mode Observer-Based Approaches”. In: *IEEE Transactions on Industrial Electronics* 63.6 (2016), pp. 3677–3685. DOI: 10.1109/TIE.2016.2523913.

[101] İlyas Eker. “Sliding mode control with PID sliding surface and experimental application to an electromechanical plant”. In: *ISA Transactions* 45.1 (2006), pp. 109–118. ISSN: 0019-0578. DOI: https://doi.org/10.1016/S0019-0578(07)60070-6. URL: http://www.sciencedirect.com/science/article/pii/S0019057807600706.

[102] Hoon Lee and Vadim I. Utkin. “Chattering suppression methods in sliding mode control systems”. In: *Annual Reviews in Control* (2007). ISSN: 1367-5788. DOI: https://doi.org/10.1016/j.arcontrol.2007.08.001.

[103] V. Utkin. “Variable structure systems with sliding modes”. In: *IEEE Transactions on Automatic Control* 22.2 (1977), pp. 212–222. DOI: 10.1109/TAC.1977.1101446.

[104] Dominic Dirkx and Kevin Cowan. *AE4868 Numerical Astrodynamics, Lecture Notes*. Delft University of Technology, Astrodynamics and Space Missions Department, 2019.

[105] Marin Kobilarov. *Discrete Geometric Motion Control of Autonomous Vehicles*. Master thesis,University of Southern California, 2007.

[106] Nawaf Bou-Rabee and Jerrold Marsden. “Hamilton–Pontryagin Integrators on Lie Groups Part I: Introduction and Structure-Preserving Properties”. In: *Foundations of Computational Mathematics* 9 (Mar. 2009). DOI: 10.1007/s10208-008-9030-4.

[107] Dominic Dirkx and Erwin Mooij. *AE4866 – Propagation and Optimization, Lecture Notes*. Delft University of Technology, Astrodynamics and Space Missions Department, 2020.

[108] Sandip Aghav and Shashikala Gangal. “Simplified Orbit Determination Algorithm for Low Earth Orbit Satellites Using Spaceborne GPS Navigation Sensor”. In: *Artificial Satellites* 49 (June 2014). DOI: 10.2478/arsa-2014-0007.

[109] Humei Wang, Wei Yang, and Li Junfeng. “Solution set on the natural satellite formation orbits under first-order earth’s non-spherical perturbation”. In: *Acta Mechanica Sinica/Lixue Xuebao* 21 (Nov. 2005), pp. 503–510. DOI: 10.1007/s10409-005-0063-5.

[110] Y. Zhang et al. “A comparative study of Luenberger observer, sliding mode observer and extended Kalman filter for sensorless vector control of induction motor drives”. In: *2009 IEEE Energy Conversion Congress and Exposition*. 2009, pp. 2466–2473. DOI: 10.1109/ECCE.2009.5316508.

[111] E.J. Lefferts, F.L. Markley, and M.D. Shuster. “Kalman Filtering for Spacecraft Attitude Estimation”. In: *Journal of Guidance, Control, and Dynamics* 5.5 (1982), pp. 417–429. DOI: 10.2514/3.56190. eprint: https://doi.org/10.2514/3.56190. URL: https://doi.org/10.2514/3.56190.

[112] Bruno Teixeira et al. “Flight path reconstruction – A comparison of nonlinear Kalman filter and smoother algorithms”. In: *Aerospace Science and Technology* 15 (Feb. 2011), pp. 60–71. DOI: 10.1016/j.ast.2010.07.005.

[113] J. Havlık and O. Straka. “Performance evaluation of iterated extended Kalman filter with variable step-length”. In: *Journal of Physics: Conference Series* 659 (2015, doi: 10.1088/1742-6596/659/1/012022), pp. 12–22.

[114] I. Miletović et al. “Improved Stewart platform state estimation using inertial and actuator position measurements”. In: *Control Engineering Practice* 62 (2017, doi: 10.1016/j.conengprac.2017.03.006), pp. 102–115.

[115] K.J. Astrom and Richard Murray. “Feedback Systems: An Introduction for Scientists and Engineers”. In: (Jan. 2008).

[116] An-Min Zou and Krishna Kumar. “Finite-time attitude control for rigid spacecraft subject to actuator saturation”. In: *Nonlinear Dynamics* 96 (Apr. 2019). DOI: 10.1007/s11071-019-04836-7.

[117] Keum W. Lee and Sahjendra N. Singh. “Adaptive and Supertwisting Adaptive Spacecraft Orbit Control Around Asteroids”. In: *Journal of Aerospace Engineering* 32.4 (2019), p. 04019042. DOI: 10.1061/(ASCE)AS.1943-5525.0001043. eprint: https://ascelibrary.org/doi/pdf/10.1061/\%28ASCE\%29AS.1943-5525.0001043. URL: https://ascelibrary.org/doi/abs/10.1061/%5C%28ASCE%5C%29AS.1943-5525.0001043.

[118] Anastasia Veloni and Nikolaos Miridakis. *Digital Control Systems. Theoretical Problems and Simulation Tools*. CRC Press, 2017.

[119] J. et al Wertz. “Space Mission Engineering: The New SMAD”. In: (2011).

[120] Patrick Blau. *Spaceflight101.com*. https://spaceflight101.com/osiris-rex/osiris-rex-spacecraft-overview/. 2020 (accessed January 12, 2021).

[121] Lockheed Martin Dani Hauf. *OSIRIS-REx, Discovering the Origins of the Solar System*. https://www.lockheedmartin.com/en-us/products/osiris-rex.html. 2020 (accessed January 12, 2021).

[122] Robert G. Melton. “Fundamentals of Astrodynamics and Applications”. In: *Journal of Guidance, Control, and Dynamics* 21.4 (1998), pp. 672–672. DOI: 10.2514/2.4291. eprint: https://doi.org/10.2514/2.4291. URL: https://doi.org/10.2514/2.4291.

[123] Bong Wie. “Space Vehicle Dynamics and Control, Second Edition”. In: *AIAA Guidance, Navigation, and Control Conference*. DOI: https://doi.org/10.2514/4.860119.

[124] J. B. Moor and B. D. O. Anderson. *Optimal Filtering*. Prentice Hall Information and System Sciences Series, 1979.

[125] F. Landis Markley and John L. Crassidis. “Correction to: Fundamentals of Spacecraft Attitude Determination and Control”. In: *Fundamentals of Spacecraft Attitude Determination and Control*. New York: Springer, 2014, isbn: 978-1-4939-0802-8.

Appendices

Chapter A

Appendix

A.1 SIMULINK MODELS

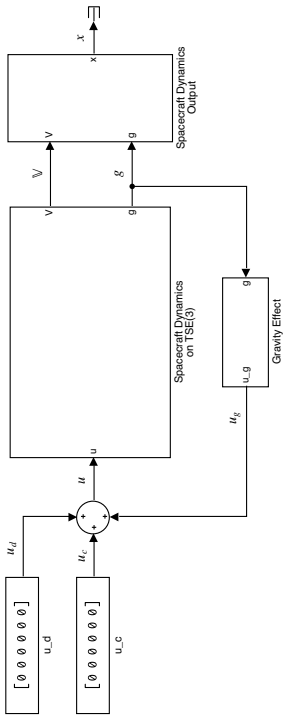

Figure A.1: Simulink Model used for the open-loop simulation.

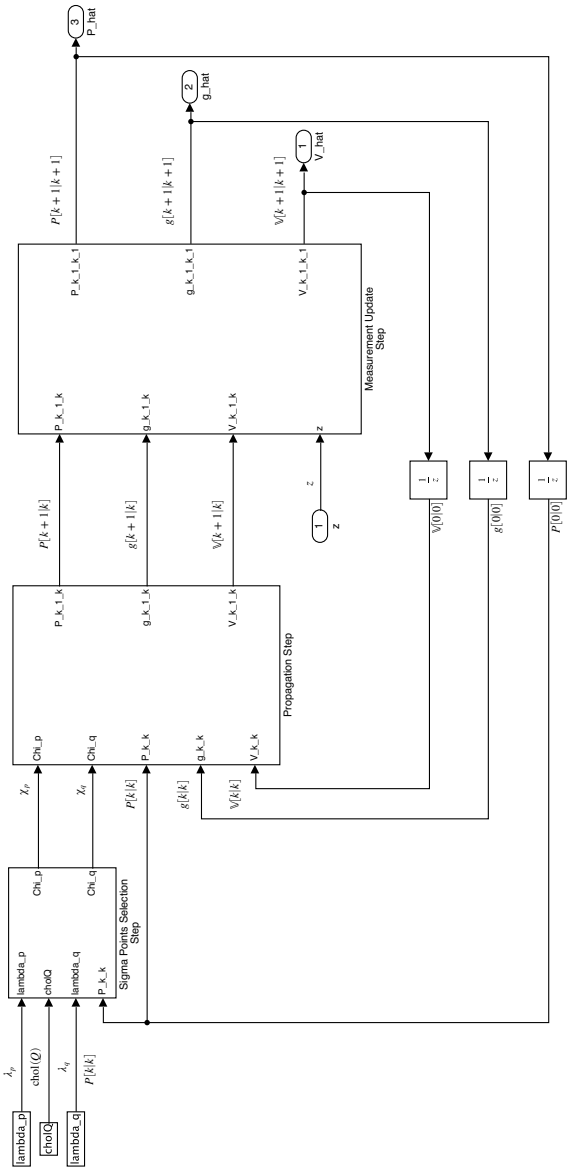

Figure A.2: Simulink Model for the UKF navigation algorithm.

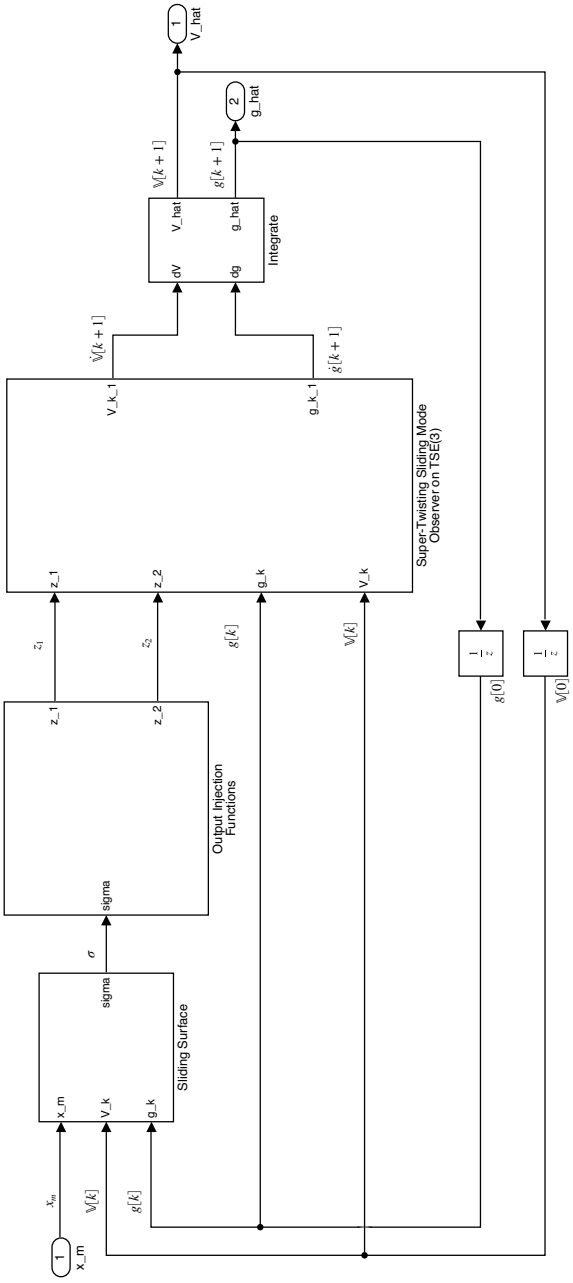

Figure A.3: Simulink Model for the STO navigation algorithm

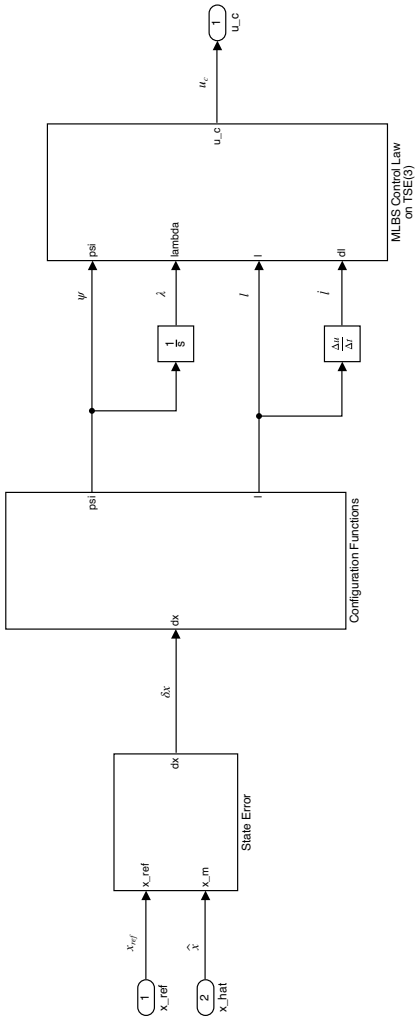

Figure A.4: Simulink Model used for MLBS control algorithm.

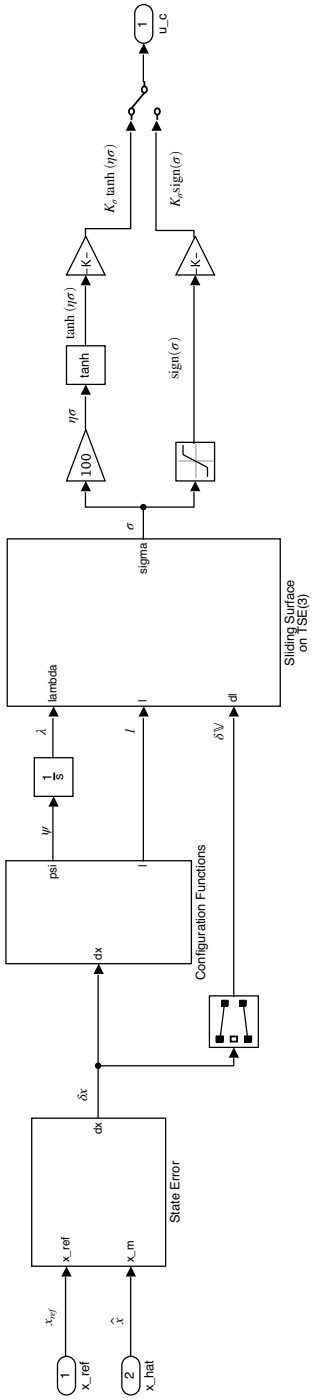

Figure A.5: Simulink Model used for SMC control algorithm.

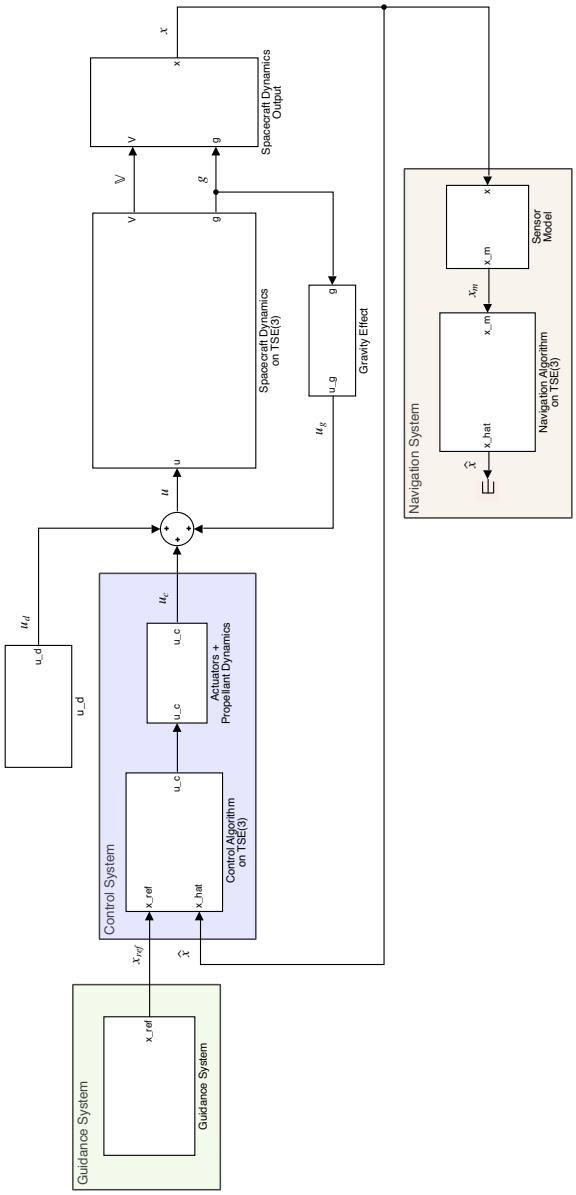

Figure A.6: Simulink Model used for the comparison of UKF and STO algorithms

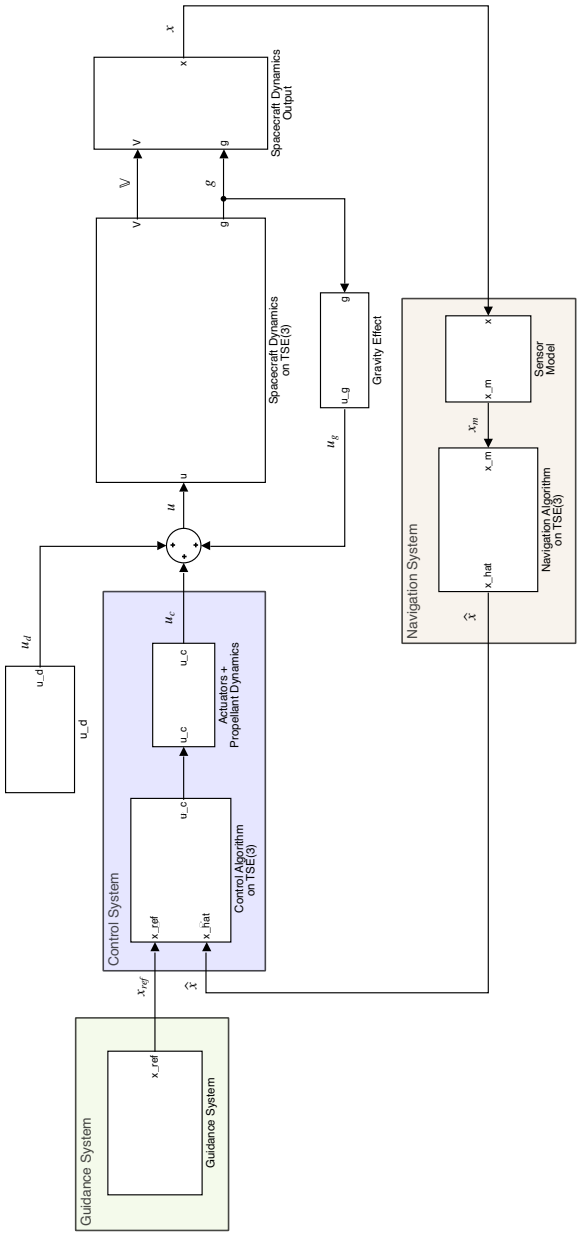

Figure A.7: Simulink Model for the complete guidance, navigation and control simulation.

A.2 UKF ALGORITHM VERIFICATION

The performance of the proposed UKF is compared to those of other state filters designed on SE(3) that can be found in literature. In particular, the algorithms selected for the comparison are i) the EKF on Lie group introduced in [4] (EKF); ii) the UKF on Lie group introduced in [8] (UKF); iii) the discrete EKF on Lie group (DEKF) described in [6]. The performance analysis is conducted on the basis of position and attitude estimation results. The study case consists in the propagation of the open loop spacecraft dynamics around the asteroid Bennu, where the data previously introduced are used. As done in [8, 7], the results are shown in Fig. A.8 in terms of the root mean square of the pose estimation error (RMSE). Particularly the first row reflects the position RMSEs, and the second row the attitude RMSEs. The Fig. A.8 depicts attitude and position RMSE as a function of: sample period Δt (left) with $\zeta_r = 10^{-1}$ km, $\zeta_\Theta = 10^{-1}$ deg and $\chi_r = 0$ km ,$\chi_\Theta = 0$ km (left); initial condition inaccuracies χ_r, χ_Θ with $\zeta_r = 10^{-1}$ km, $\zeta_\Theta = 10^{-1}$ deg and $\Delta t = 1$ s (center); measurement noise standard deviations ζ_r km, $\zeta\Theta$ deg with $\zeta_r = 10^{-1}$ km, $\zeta_\Theta = 10^{-1}$ deg and $\Delta t = 1$ s (right).

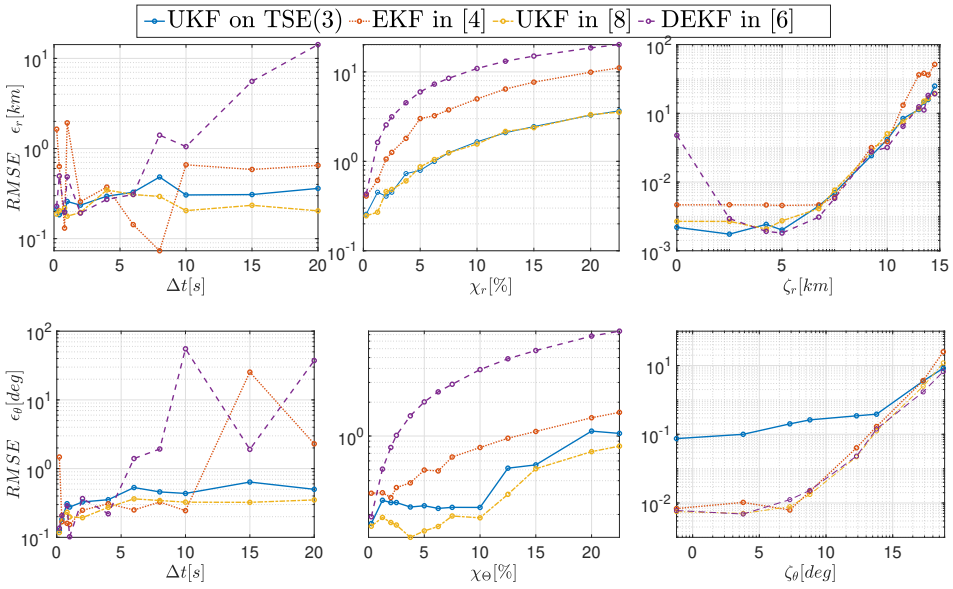

Figure A.8: Attitude and position RMSE as a function of sample period, initial condition inaccuracies and measurement noise standard deviations.

In the left column of Fig. A.8, the RMSE(s) for the position and attitude error are shown along with the sample period Δt from 0.1 to 20 seconds. It can be seen that the proposed filter (solid) and the UKF (dash) are robust to changes in the sampling frequency, whereas the other two filters based on the EKF are more unstable. Particularly, the EKF (dot) and DEKF (dash-dot). For smaller time steps, the difference among different filters reduces. Then the UKF on TSE(3) and the UKF proposed in [8] behave almost the same, achieving an higher accuracy with respect to EKF and DEKF even for large Δt. The center

column of Fig. A.8 shows the RMSE(s) for the position and attitude error along with the percentage of uncertainty on the filter initial pose estimate with respect to the true pose. Particularly, let the true values be r_0 and Θ_0, the filters initial guesses are parametrized as $r_0(1+\chi_r/100), R(\Theta_0(1+\chi_\Theta/100))$. As expected, the best performance are achieved for small values of uncertainties. The UKF filters outperform the EKF filters for all the range of χ_r, χ_Θ since the EKF are particularly influenced by the initial condition accuracy. Finally, in the right column of Fig. A.8, the RMSE(s) are given as functions of the standard deviation of the measurement noise, for the position and attitude measurements. Note that the proposed UKF filter on $\mathsf{TSE}(3)$ achieves the lowest accuracy in terms of attitude $\mathrm{O}(10^{-1})$ deg even with the smallest noise standard deviation. It can be explained by the fact that the UKF on $\mathsf{TSE}(3)$ also estimates the velocities which are assumed to be provided by noisy sensors, while the filter on $\mathsf{SE}(3)$ uses un-noisy velocities and only updates on position and attitude measurements. Generally, as shown in the figure, the proposed UKF on $\mathsf{TSE}(3)$ and standard UKF perform better than others. Even if the DEKF seems to be robust to noisy measurements, it is dependent on the initial condition accuracy and sample frequency. According Fig. A.8, the EKF on $\mathsf{SE}(3)$ [4] is able to achieve an higher accuracy of DEKF on $\mathsf{SE}(3)$ [6] and lower accuracy than the UKF on $\mathsf{SE}(3)$ [8] and the proposed UKF on $\mathsf{TSE}(3)$. The latter one has proved to be particularly robust even with noisy measurements, inaccurate initial conditions, and low sampling frequency.